ISSN 1883 - 0315

TOHOKU
UNIVERSITY

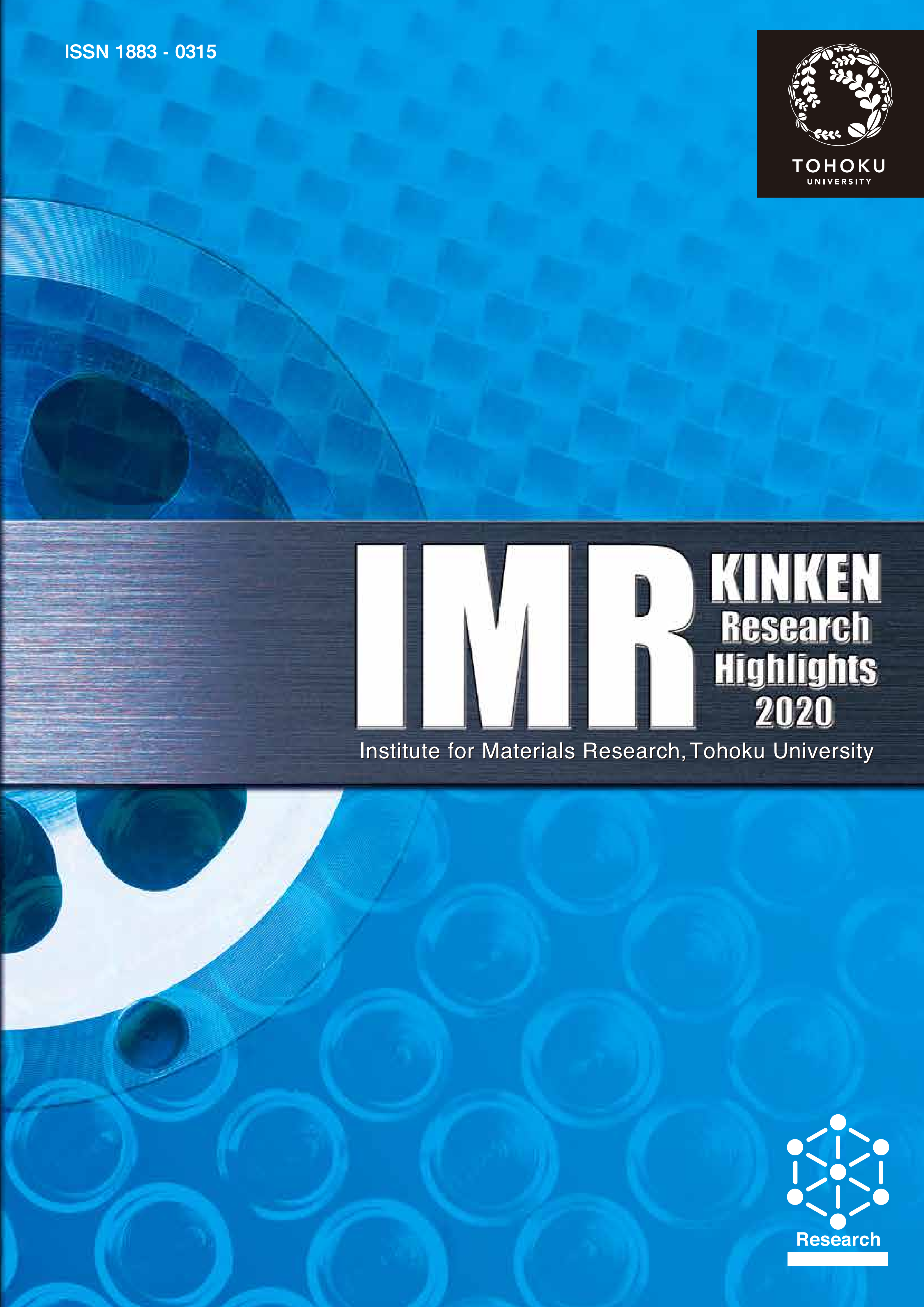

IMR KINKEN Research Highlights 2020

Institute for Materials Research, Tohoku University

Research

KINKEN

Research Highlights

2020

Institute for Materials Research, Tohoku University

KINKEN Research Highlights 2020

Contents

Research Highlights

1. Infrastructural Materials

2. Energy-Related Materials

3. Electronic Materials

Research Centers

International Collaborative Research

Preface

Dear Colleagues,

We are pleased to present *KINKEN* Research Highlights 2020, which is the annual report that includes a collection of research outputs of the past year from the Institute for Materials Research (IMR), Tohoku University. *KINKEN* is the abbreviation for “Kinzoku Zairyo Kenkyujo,” the Japanese name for IMR, which is well known in the materials science community.

IMR was the first Tohoku University research institute, of which there are currently six, to be established in 1916. Aiming to contribute to the well-being of the human race and the development of civilization through the creation of new materials that are useful to society, it carries out research on both the fundamentals and applications of a wide range of substances and materials. After its founding, IMR first focused on steel but quickly expanded its research area to the other metals and alloys. Then, in response to changing times and economic growth, it came to cover semiconductors, ceramics, and a wide range of other materials. Ever since our first director, Professor Kotaro Honda, invented the first artificial permanent magnet called “KS steel,” we have developed many new materials for practical use, including Sendust alloy, SiC fibers, and soft magnetic amorphous alloys. We have also focused on fundamental research, which is important for the development of new materials, as well as carried out cutting-edge research on magnetism, optical properties, superconductivity, and microstructure of materials. While doing so, IMR has become a leading research institute in the field of materials science.

IMR is notable for its fusion of fundamental and applied research, as well as of science and engineering. We offer some of the best large research facilities in the world — covering high-energy

Tadashi Furuhara

Director Prof. Tadashi Furuhara

irradiation, strong magnetic fields, and supercomputing — enabling researchers from Japan and abroad to engage in a variety of collaborative projects. To develop superior or new materials that are useful, we believe it is necessary to organically connect three “pillars”: (1) the “exploration” of physical phenomena that govern materials’ functions, (2) the “creation” of materials via various methods, and (3) the “measurement” of materials’ properties from various perspectives. IMR has for many years been contributing to the materials research community via our joint usage/research programs. IMR celebrated its 100-year anniversary in 2016. Having been designated in 2018 as an International Joint Usage/Research Center in Materials Science, known as Global Institute for Materials Research Tohoku (GIMRT), we have now further heightened our efforts to enhance such collaborations and cultivate new talent.

In the 21st century, our society faces global-scale environmental issues, such as global warming, resource depletion, acquiring a stable energy supply, and new kinds of environmental pollution. IMR will continue to work towards a sustainable society both by engaging in important research to solve various problems as well as by creating new areas of research that can bring about paradigm shifts in the future.

We hope that the KINKEN Research Highlights will enable you to better understand our recent research activities and will aid the promotion of worldwide collaboration with IMR. We ask for your continued support and welcome any suggestions.

Infrastructural Materials

Atom Probe Compositional Analysis of Interphase Precipitated Nano-Sized Alloy Carbide in Multiple Microalloyed Low-Carbon Steels

The composition of nano-sized alloy carbide formed by interphase precipitation at the migrating ferrite/austenite interface during ferrite transformation in vanadium-titanium multiple microalloyed low-carbon steels was analyzed using a three-dimensional atom probe. As carbide-forming elements, vanadium and titanium were simultaneously precipitated from the early stage of transformation, while the alloy carbide was more strongly enriched with titanium than vanadium.

Interphase precipitation of NaCl-structured nano-sized alloy carbide occurs at the migrating ferrite/austenite interface during ferrite transformation in steels containing strong carbide-forming elements such as vanadium (V), niobium (Nb), and titanium (Ti). In our previous studies, the effects of various factors, including transformation temperature, alloy composition, etc., on the interphase precipitation behaviors in V-added low-carbon steels were systematically investigated [1]. In this study, we attempted to quantitatively analyze the chemical composition of alloy carbide formed by interphase precipitation in a low-carbon steel, which is formed by the addition of multiple microalloying elements. Thus, we aimed to obtain more detailed insights into the nature of interphase precipitation.

The Fe-0.4C-1.5Mn-0.1Si-0.1V-0.1Ti (at%) alloy was firstly treated at 1,523 K for 0.6 ks to dissolve all the added V and Ti, and then held at 923 K for 60 s to perform isothermal ferrite transformation, followed by water quenching to freeze the microstructure. Next, a focused ion beam was used to prepare needle-shaped samples from the ferrite region with interphase precipitation in the transformed specimen, for the subsequent three-dimensional atom probe (3DAP) measurements.

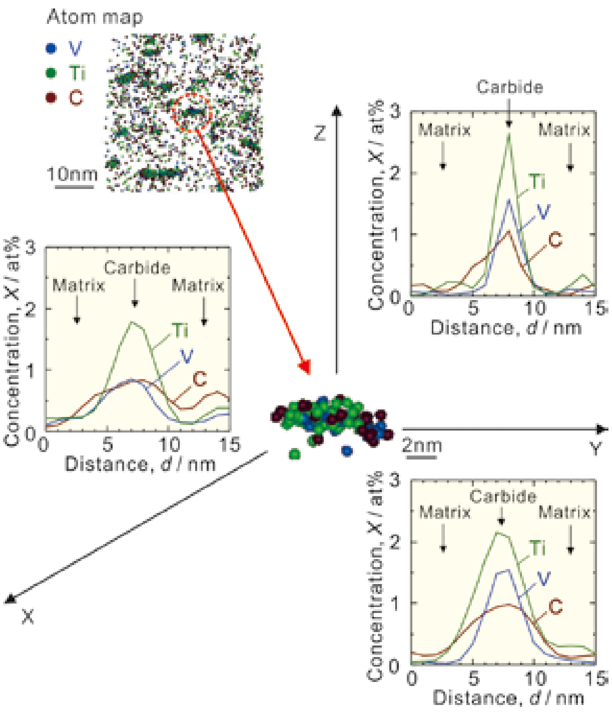

Fig. 1 Three-dimensional atom map in the V-Ti multiple-added alloy isothermally transformed at 923 K for 60 s, with one-dimensional concentration profiles across a specific carbide along three mutually perpendicular directions [2].

Figure 1 shows an example of the typical results obtained from 3DAP analysis. The atom map shows the inhomogeneous elemental distribution, while the enlarged atom map reveals that V, Ti, and C atoms were homogeneously distributed in the enriched regions without any core-shell structure, indicating the simultaneous precipitation of V and Ti as complex alloy carbides. This result is also supported by the one-dimensional concentration profiles obtained from three mutually perpendicular directions across the carbide, showing the synchronized variations in the concentrations of various elements. It is evident that the total amount of V, Ti, and C in the carbide was far below 100%, which was likely caused by the artifacts in 3DAP. By assuming the theoretical stoichiometry of the alloy carbide, its chemical composition was estimated to be $(V_{0.33}Ti_{0.67})C$. With the same bulk additive amount in at% of V and Ti, the concentration of Ti in the carbide was significantly higher than that of V, possibly due to its relatively stronger affinity to C and thus a strong tendency to precipitate in steels.

References

[1] Y.-J. Zhang, G. Miyamoto, K. Shinbo, and T. Furuhara, Acta Mater. **128**, 166 (2017).

[2] Y.-J. Zhang, G. Miyamoto, and T. Furuhara, Microsc. Microanal. **25**, 447 (2019).

Keywords: atom probe tomography, precipitation, steel

Yongjie Zhang (Microstructure Design of Structural Metallic Materials Research Laboratory)
E-mail: yongjie@imr.tohoku.ac.jp
URL: http://www.st-mat.imr.tohoku.ac.jp/en/index.html

Detecting Hydrogen Desorption During Deformation-Induced Martensitic Transformation in Steels

Hydrogen absorption, diffusion, trapping, and desorption are key phenomena to understand hydrogen embrittlement. In particular, deformation-hydrogen interaction is the origin of the complexity of hydrogen embrittlement. In this context, we recently succeeded in detecting hydrogen desorption occurring during the deformation-induced martensitic transformation in steels. The hydrogen desorption behavior showed significant differences among the fcc-hcp and fcc-bcc transformations, and dislocation glide without transformation.

Deformation-induced martensitic transformation (diffusionless transformation) in metals locally alters the solubility and diffusivity of hydrogen because of the crystallographic changes. The changes in solubility and diffusivity critically affect hydrogen embrittlement susceptibility when the metals have a significant hydrogen content [1]. For instance, type 304 austenitic steel is susceptible to hydrogen embrittlement because of the fcc to bcc martensitic transformation. Therefore, monitoring hydrogen motion during deformation-induced martensitic transformation is a key technique for clarifying the mechanism of hydrogen embrittlement. However, the detection of hydrogen during martensitic transformation is difficult because hydrogen is light/mobile and martensitic transformation is an instantaneous phenomenon.

To detect hydrogen desorption during martensitic transformation, mass spectrometry was utilized [2]. Specifically, a tensile testing machine was installed in a vacuum chamber equipped with a mass spectrometer. Then, some austenitic steels were prepared: Fe-19Cr-8Ni-0.14C, Fe-15Mn-10Cr-8Ni, and Fe-19Cr-14Ni-0.15C (mass%). The Fe-19Cr-8Ni-0.14C and Fe-15Mn-10Cr-8Ni steels showed the fcc-bcc and fcc-hcp martensitic transformations, respectively, while the Fe-19Cr-14Ni-0.15C steel did not show any martensitic transformation during tensile deformation until fracture. Figure 1 shows the martensite fraction as a function of strain.

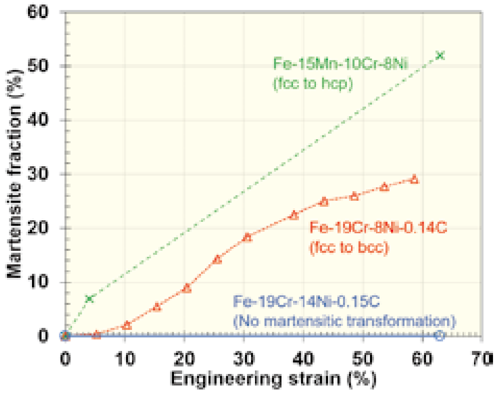

Fig. 1 Martensite fraction plotted against tensile strain.

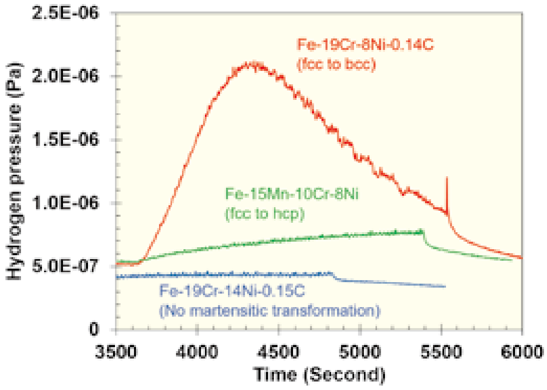

Fig. 2 Hydrogen desorption curves.

The specimens with different deformation modes were tensile-deformed at 298 K with an initial strain rate of 5×10^{-4} s^{-1}, and the desorbed hydrogen was detected as shown in Fig. 2. The hydrogen pressure and time correspond to the hydrogen desorption rate and nominal strain, respectively. The most remarkable hydrogen desorption was detected in the Fe-19Cr-8Ni-0.14C steel in which the fcc-bcc martensitic transformation occurred. The hydrogen desorption rate observed in the fcc-hcp martensitic transformation was much lower than that in the fcc-bcc martensitic transformation, and significant compared with the case without martensitic transformation. Interestingly, this result corresponds to hydrogen embrittlement susceptibility, i.e., the effect of fcc-hcp martensitic transformation on hydrogen embrittlement susceptibility was smaller than that on fcc-bcc martensitic transformation. We believe that our new approach would enable us to understand and predict the hydrogen embrittlement behavior of metals.

References

[1] M. Koyama, D. Yamasaki, A. Ikeda, T. Hojo, E. Akiyama, K. Takai, and K. Tsuzaki, Int. J. Hydrog. Energy. **44**, 26028 (2019).

[2] T. Hojo, M. Koyama, N. Terao, K. Tsuzaki, and E. Akiyama, Int. J. Hydrog. Energy. **44**, 30472 (2019).

Keywords: hydrogen, steel, phase transformation

Motomichi Koyama (Environmentally Robust Materials Research Laboratory)
E-mail: koyama@imr.tohoku.ac.jp
URL: https://akiyamaimr-e.amebaownd.com/

Novel Mode of Omega(ω)-Transformation in Titanium Alloys

Understanding the mechanism of the omega(ω)-transformation is crucial for the development of beta(β)-titanium alloys. We have recently demonstrated that a novel type of ω-transformation, diffusionless isothermal ω-transformation, can gradually proceed even above the ω-transformation temperature. The transformation mechanism can be reasonably explained by the quenched-in compositional fluctuations that are inevitably present in thermal equilibrium.

Owing to their high strength, corrosion resistance, and biocompatibility, titanium alloys are widely used for structural and biomedical materials. In the development of titanium alloys, the control of the transformation from the β-phase (body-centered cubic) to the ω-phase (hexagonal) is crucial because the latter dominates the microstructure and mechanical properties of the titanium alloys.

In terms of the transformation kinetics, the ω-transformation has been categorized into two transformation modes: athermal and isothermal ω-transformations. The former occurs instantaneously via a diffusionless mechanism, while the latter occurs gradually via atomic diffusion in conjunction with solute-atom partitioning. We, however, have demonstrated that a *diffusionless isothermal* ω-transformation can gradually occur near room temperature by elasticity and internal friction measurements, X-ray diffraction, atomic-resolution transmission electron microscopy, Fig. 1(a), and 3D atom-probe analysis [1].

Such an anomalous “diffusionless isothermal ω-transformation” was found to occur in locally unstable regions (a few nanometers in size) with less β-stabilizing elements, which are inevitably present owing to the quenched-in compositional fluctuations, as shown in Fig. 1(b) [1]. The ω-transformation is generally known to arise from the localized softening of the 2/3[111]$_\beta$ longitudinal phonon. Therefore, it can be concluded that the present localized transformation cannot be suppressed by the stabilization of the β-phase on average. The quenched-in compositional fluctuations (in equilibrium originally at a high temperature) determine the activation energies of the ω-nucleation process and the dynamic {111}$_\beta$ collapse. Thus, the compositional fluctuation is key to understanding the thermodynamics and kinetics of the ω-transformation [1]. This mechanism of the localized transformation is distinct from that of displacive transformations with large transformation strains, which cooperatively occur in widely spread regions, accompanied by the softening of long wavelength acoustic phonons at the gamma point.

References

[1] M. Tane, H. Nishiyama, A. Umeda, N. L. Okamoto, K. Inoue, M. Luckabauer, Y. Nagai, T. Sekino, T. Nakano, and T. Ichitsubo, Phys. Rev. Materials **3**, 043604 (2019).

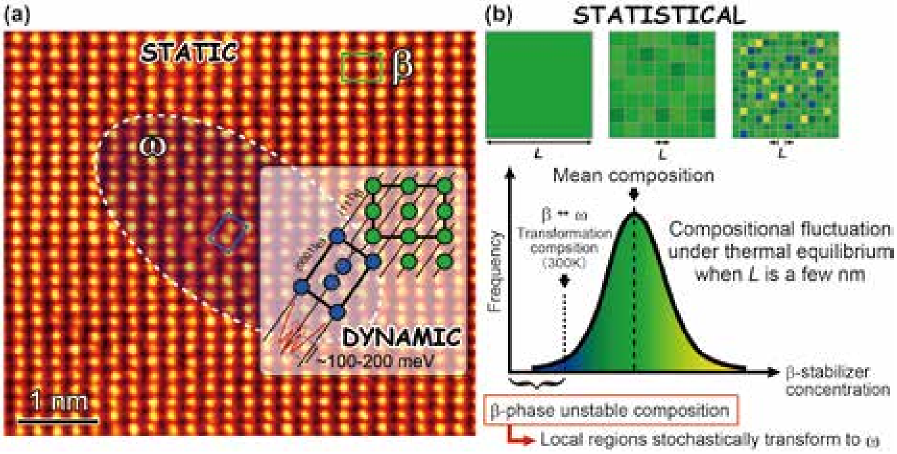

Fig.1 (a) Scanning transmission electron microscopy image of a Ti-21 at% V alloy aged at 323 K for ten days. Electron incidence is [110]$_\beta$. The {111}$_\beta$ planes fully collapse at the center of the ω-phase particle. (b) Schematic illustration of the quenched-in compositional fluctuations. As the voxel size (*L*) decreases, the composition fluctuation becomes more significant.

Keywords: metal, phase transformation, scanning transmission electron microscopy (STEM)

Tetsu Ichitsubo, Norihiko L. Okamoto, Hiroshi Tanimura, and Tomoya Kawaguchi (Structure-Controlled Functional Materials Research Laboratory)
E-mail: nlokamoto@imr.tohoku.ac.jp (NLO), tichi@imr.tohoku.ac.jp (TI)
URL: http://www.imr.tohoku.ac.jp/en/about/divisions-and-centers/research-division/16.html
http://ilab.imr.tohoku.ac.jp/~ilab/index.html/

Highly Efficient Process Design for Powder Bed Fusion-Type Additive Manufacturing Using an Electron Beam

We have developed and demonstrated a novel process design method for powder bed fusion-type additive manufacturing using an electron beam. This method utilizes the design of experiments and support vector machine, one of the machine learning methods, to provide the optimum conditions required for obtaining defect-free, additively manufactured parts without any destructive inspections.

Additive manufacturing (AM) is a technology that enables near-net shaping of metal parts with complex shapes. Powder bed fusion-type AM using an electron beam (PBF-EB) is an AM technology in which the re-coated metal powders are heated and selectively melted in a layer-by-layer manner using an electron beam. The PBF-EB can provide high quality metal parts as compared to a PBF-type AM using a laser beam (PBF-LB) because the former process is conducted at a high temperature under a high vacuum, leading to low thermal stress and less oxidation. Although the defect density in metal parts built using the PBF-EB is smaller than in those built using the PBF-LB, the former usually include pores that degrade the mechanical properties. Although the mechanism of defect formation and solidification during the PBF-LB process has been revealed by synchrotron X-ray imaging, it is still challenging to suppress defect formation during the PBF-LB and PBF-EB processes and fabricate defect-free metal parts. Although many efforts have been made to optimize processes for defect-free AM built parts, effective methods for process design have not been developed yet.

We have developed a highly efficient process design method for the PBF-EB process. This method utilizes the relationship between surface morphology and defect formation. A non-flat surface provides a non-uniform powder bed layer that is helpful in forming a next layer, leading to defect formation. In contrast, a flat surface provides a uniform powder bed layer, leading to defect-free parts. The robust condition will be one with the largest distance from the boundary between the flat and non-flat surfaces. This method applied the distance from the boundary between the flat and non-flat surfaces as a process condition. A support vector machine, which is a machine learning technique, was used to determine the classification boundary. Although only the sign of the decision function is usually used, our method uses not only the sign but also the value of the decision function.

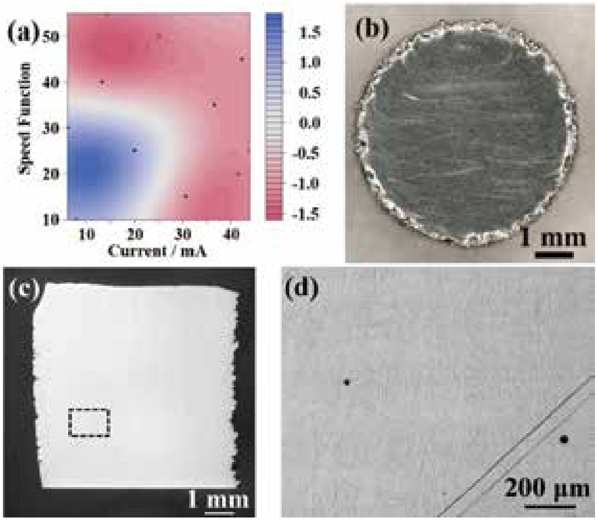

Fig. 1 (a) Process map constructed by an SVM. (b) Surface and (c) cross-sectional image of the PBF-EB built cylinder under the optimized condition with the highest decision function value. (d) Enlarged image of the region shown by the dotted rectangle in Fig. 1(c). [1]

We demonstrated our method for the CoCrMo alloy, as shown in Fig. 1 [1]. Only eleven data points were used in this demonstration, and it took only twelve hours. The PBF-EB built cylinder had no process defects. The spherical pores shown in Fig. 1(d) originated from the entrapped gas pores in the raw material powders. This result indicates that our method can predict the optimum condition for defect-free AM built parts with reduced lead time. Our method can optimize not only two-dimensional parameters, but also multi-dimensional parameters.

References

[1] K. Aoyagi, H. Wang, H. Sudo, and A. Chiba, Addit. Manuf. **27**, 353 (2019).

Keywords: additive manufacturing, alloy, defects

Kenta Aoyagi (Deformation Processing Research Laboratory)
E-mail: k.aoyagi@imr.tohoku.ac.jp
URL: http://www.chibalab.imr.tohoku.ac.jp/english/index.html

Statistical Analysis of the Distribution of Alumina Inclusion Particles in Stainless Steels in Laser-Induced Breakdown Spectrometry Using 1-kHz Q-Switched Nd:YAG Laser

A two-dimensional distribution of alumina inclusion particles in ferritic stainless steels was obtained from variations in the emission intensity of an Al I line, when a 1-kHz Q-switched Nd:YAG laser was scanned on a sample surface in laser-induced breakdown spectrometry (LIBS). This method provides a simpler and faster analytical method to determine the distribution of alumina inclusions than the conventional methods.

Quantitative and morphological assessments of non-metallic inclusion particles, which are embedded in the structure of steel materials, is an important issue in the analysis of steel products. Especially, 'hard' inclusions, such as coarse alumina particles, may cause any fatigue of structural steel materials and sometimes leave scratches and creases on the surface of the final product, depending on the number density and the size of the inclusions.

Laser-induced breakdown spectroscopy (LIBS) has been employed to analyze various solid samples directly and rapidly, because little pretreatment of the samples is required before the measurement. The scanning LIBS provides the distribution of constituent elements in a sample area by measuring their emission intensities. In this study, the quantitative distribution of alumina inclusions in ferritic stainless steels was measured when the LIBS system was operated under the optimal measuring conditions. The objective of this study was to develop a rapid measuring method suited for such elemental mapping.

The laser used in the experiment was a Q-switched Nd:YAG laser, having an oscillation wavelength of 532 nm. The emission signal from the plasma was measured on a spectrometer, comprising a grating monochromator and a photomultiplier, whose effective spectral band-path was ~0.1 nm at a wavelength of 300 nm [1]. The plasma chamber could be precisely moved to the laser beam three-dimensionally, when it was fixed on an X-Y-Z stage. The X-Y-Z stage was adjusted in each direction until the irradiation position of the laser had been focused on the target position of the sample surface, and then the laser beam was moved along a lateral direction at a constant scanning rate [1].

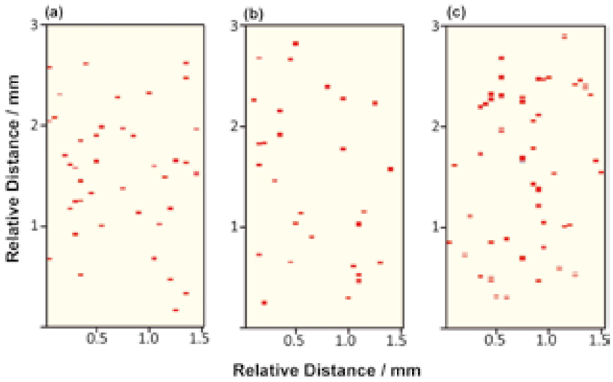

Fig. 1 Two-dimensional maps of the Al I emission intensity for samples A (a), B (b), and C (c).

Three kinds of ferritic stainless steels were prepared as test samples, labeled as samples A, B, and C, which included alumina particles (Al_2O_3) precipitated in the iron matrix. From the result of chemical analysis, the amounts of alumina inclusion in sample C would be twice larger than those in samples A and B.

A typical result of the two-dimensional map, based on the emission intensity of the Al I 396.152-nm line after the background correction, is illustrated in Fig. 1 [2]. The number of alumina particles in samples A, B, and C, were 35, 27, and 47, respectively. There were more alumina particles in sample C compared to the samples A and B, which agreed with the chemical analysis.

The analysis time was ~20 min for the sample area of 4.5 mm^2 to obtain the distribution of alumina inclusions. This method could provide the map of inclusions more rapidly and easily, as compared with the conventional method.

References

[1] T. Matsuda and K. Wagatsuma, ISIJ Int. **59**, 1838 (2019).

[2] T. Matsuda, S. Kashiwakura, and K. Wagatsuma, Microchem. J. **153**, 104400 (2020).

Keywords: steel, atomic emission spectrometry, laser plasma

Kazuaki Wagatsuma (Analytical Science Research Laboratory)
E-mail: wagatuma@imr.tohoku.ac.jp
URL: http://www.imr.tohoku.ac.jp/en/about/divisions-and-centers/research-division/27.html

Development of High-Performance High-Entropy Alloys Assisted by Thermodynamics and *ab initio* Calculations

High-entropy alloys have attracted considerable interest, with the stacking fault energy playing an important role in regulating their mechanical behaviors. In this study, the regulation principles have been described and a series of high-performance alloys has been designed, assisted by *ab initio* and thermodynamics calculations to shed light on the development of such novel materials.

The face-centered cubic (fcc) phase CoCrFeMnNi high-entropy alloys (HEAs) exhibit exceptional strength and ductility, both at room and cryogenic temperatures. The stacking fault energy (SFE) is a main factor affecting their plastic deformation mechanisms, which switches from dislocation slip to mechanical twinning by decreasing the fcc phase stability and SFE consecutively.

We recently demonstrated the principles for regulating SFE using *ab initio* and thermodynamic calculations [1-3]. The decreasing Mn, Ni, and Fe concentrations and increasing Co and Cr concentrations reduced the stability of the fcc phase and the SFE of CoCrFeMnNi and/or CoCrFeNi alloys (Fig. 1), and increased the elastic modulus, anisotropy, and lattice friction stress [1-2]. Further, increasing the Co concentration or minor addition of Mo promoted the yield strength [3].

Based on these findings, we developed a series of strong and ductile metastable fcc-phase HEAs with mechanical properties that were superior to those of the equiatomic counterparts. The investigation revealed that the enhancement of mechanical properties was attributed to the low-SFE-induced restriction of planar behavior of dislocations, twinning induced plasticity, strain-induced martensitic transformation, and/or Mo-addition induced strengthening. For instance, Figure 2 shows that mechanical twinning and martensitic transformation strengthened the HEAs, which exhibited superior tensile strength and ductility, as well as very high and stable strain hardening rates [3]. Thus, the present study offers a guideline for designing novel alloys.

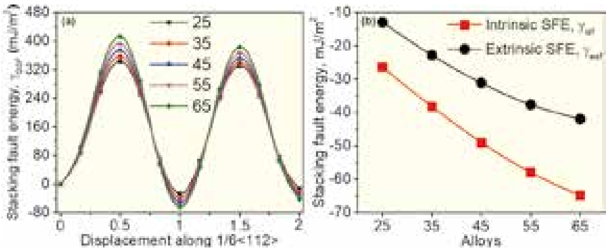

Fig. 1 (a) Generalized-stacking fault energy of the {111}<112> slip and (b) intrinsic and extrinsic stacking fault energies of $Co_xCr_{25}(FeNi)_{75-x}$ (x: 25-65) alloys calculated by ab initio method [1-2].

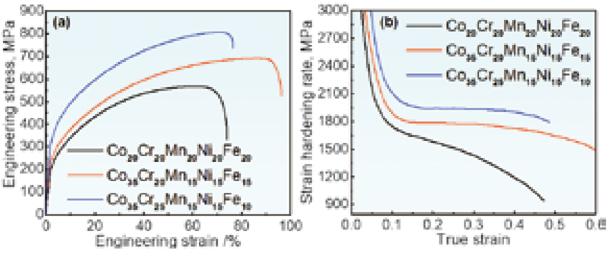

Fig. 2 (a) Room temperature engineering tensile stress-strain curves and (b) strain hardening curves of the designed $Co_{20}Cr_{20}Mn_{20}Ni_{20}Fe_{20}$, $Co_{35}Cr_{20}Mn_{15}Ni_{15}Fe_{15}$, and $Co_{35}Cr_{25}Mn_{15}Ni_{15}Fe_{10}$ high entropy alloys [3].

References

[1] D. Wei, X. Li, W. Heng, Y. Koizumi, F. He, W. M Choi, B. J. Lee, H. S. Kim, H. Kato, and A. Chiba, Mater. Res. Lett. **7** (2), 82 (2019).

[2] D. Wei, X. Li, S. Schönecker, J. Jiang, W. M. Choi, B. J. Lee, H. S. Kim, A. Chiba, and H. Kato, Acta Mater. **181**, 318 (2019).

[3] D. Wei, X. Li, J. Jiang, W. Heng, Y. Koizumi, W. M. Choi, B. J. Lee, H. S. Kim, H. Kato, and A. Chiba, Scr. Mater. **165**, 39 (2019).

Keywords: microstructure, mechanical properties, phase transformation

Daixiu Wei (Corresponding Author, Creation of Life Innovation Materials for Interdisciplinary and International Researcher Development)
E-mail: wei1987xiu@imr.tohoku.ac.jp
Hidemi Kato (Project Leader of Creation of Life Innovation Materials for Interdisciplinary and International Researcher Development)
E-mail: hikato@imr.tohoku.ac.jp
URL: http://www.imr.tohoku.ac.jp/en/about/divisions-and-centers/research-division/29.html

Entropy of a High-Entropy Alloy

The Professional development Consortium for Computational Materials Scientists (PCoMS) supports promising young scholars to engage in joint research at one of the four member institutions. The results obtained by Prof. T. Q. Nguyen of Osaka University during his extended stay at IMR, in which the entropy of a high-entropy alloy was calculated from first-principles, are outlined below.

Predicting the stability of alloys is an important task for materials design and development. Owing to the success of *ab initio* modeling techniques such as density functional theory (DFT), calculations on the ground-state properties of materials have become incredibly accurate. Despite such success, however, extending *ab initio* calculations to multi-component alloys exhibiting configurational disorder remains a challenge. In addition, obtaining thermodynamic information at finite temperatures requires suitable sampling of all the excited states at thermodynamic equilibrium, which would be computationally prohibitive via brute-force quantum mechanical calculations alone.

The cluster variation method (CVM) [1] expresses the free energy in terms of a set of cluster probabilities and incorporates a wide range of configurational freedom. In the present study, first-principles CVM formalism was applied to study the entropy and compositions of constituent elements as a function of temperature for the FCC quaternary system CrFeMnNi. The equiatomic composition of this alloy, $Cr_{25}Fe_{25}Mn_{25}Ni_{25}$, has been attracting widespread interest as a high-entropy alloy (HEA).

For the abovementioned quaternary system, there are ten different pairs. Thus, to find the interaction energy of each pair, we considered ten structures with different alloy compositions: the total energy calculations for these systems were performed using the DFT method and pair interaction energies were extracted based on our previous study [2] developed for the Fe-C system with point defects. To determine the configurational entropy, we employed a tetrahedron approximation within CVM.

Among the various results, the temperature dependence of entropy was compared between CVM and a primitive Bragg-Williams (BW) approximation. A separate calculation showed that the stable FCC CrFeMnNi alloy was mostly composed of Mn at low temperature. The concentration of Mn decreased gradually as the temperature increased and rapidly dropped to ~30% at ~850 °C (0.097k_BT), while the concentration of the other three components increased. Beyond 1,235 °C (0.130k_BT), the concentration of each component in the alloy approached the value of 25%. Accordingly, the entropy increased with temperature and reached a steady-state value. In the low temperature region, both CVM and BW provided closed values. However, at a higher temperature, the BW approximation slightly overestimated entropy. The difference, however, was not significant, which may be a characteristic feature of HEAs.

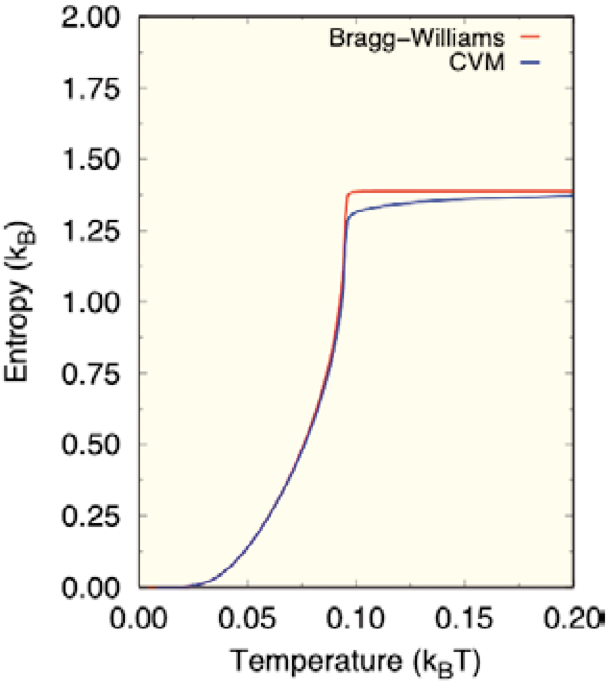

Fig. 1 Temperature dependence of entropy calculated by the Bragg-Williams approximation and cluster variation method.

References

[1] R. Kikuchi, Phys. Rev. **81**, 988 (1951).

[2] T. Q. Nguyen, M. C. S. Escano, K. Sato, Y. Shibutani, T. Oguchi, and T. Mohri, ISIJ International **59**, 2343 (2019).

Keywords: computational materials science

Yayoi Terada (PCoMS) and Tien Quang Nguyen (Institute for Nano Science Design, Osaka University)
E-mail: terada@imr.tohoku.ac.jp, quang@insd.osaka-u.ac.jp
URL: http://pcoms.imr.tohoku.ac.jp/index_e.html

Energy-Related Materials

IMR KINKEN Research Highlights 2020

In Situ Observation of the Twin-Related Dendrite Growth in GaSb

Crystal–melt interfaces were directly observed during the directional solidification of GaSb and the mechanism of faceted dendrite growth was studied. The dendrites propagated in either <110> or <112> direction. It was found that dendrite growth is related to nucleation at the re-entrant corners formed at twin boundaries.

The GaSb substrate is used in various electronic devices, *e.g.,* mid-infrared emitting lasers and thermophotovoltaic cells. As the crystal quality of the substrate has a significant influence on the electrical properties of the device, it is important to control the density and distribution of defects such as grain boundaries and dislocations in the crystal. It is known that re-entrant corners at twin boundaries provide favorable nucleation sites and pure semiconductors Si and Ge show twin-related dendrite growth. Even though twin formation is a serious problem during the solidification of group III–V compound semiconductors, its effect on dendrite growth in such semiconductors has not been studied extensively. In this study, dendrite growth during the directional solidification of GaSb was observed and the growth mechanism was clarified [1].

The *in situ* observation system used in this study consisted of a furnace and a digital microscope equipped with a zoom lens having a long working distance. The furnace had two carbon heaters that were independently controlled to produce a thermal gradient inside the furnace. GaSb was melted under an argon atmosphere, and the temperature was subsequently decreased to promote directional growth. The digital microscope was used to observe the GaSb crystal–melt interface and the growth velocity of the interface (V) was measured by tracing its position. The crystallographic orientations of the GaSb dendrites in the areas observed were determined by electron backscatter diffraction (JSM-6610A, JEOL).

A planar crystal–melt interface was maintained at low V. The planar shape became instable and a faceted interface was formed at V higher than the critical growth velocity (V_C). The dendrite growth was initiated at the faceted interface. Figure 1 shows the photographic images and schematics of the GaSb dendrite propagating in the <112> direction. The dendrite grown along <112> displayed continuous formation of two triangular crystals with a tip angle of 60°, and the growth direction of the two triangular crystals changed alternatingly. The dendrite grew not only along the <112> direction but also along the <110> direction. The dendrite grown along <110> showed that the tip angle was 120° and the growth direction of the tip did not change. Each type of dendrite exhibited a unique shape and propagation mechanism, and both growth processes were similar with those in Si. It was clarified that dendrites in GaSb grow *via* nucleation at the re-entrant corners located at the twin boundaries and more than two twin boundaries are required for the propagation of the dendrite.

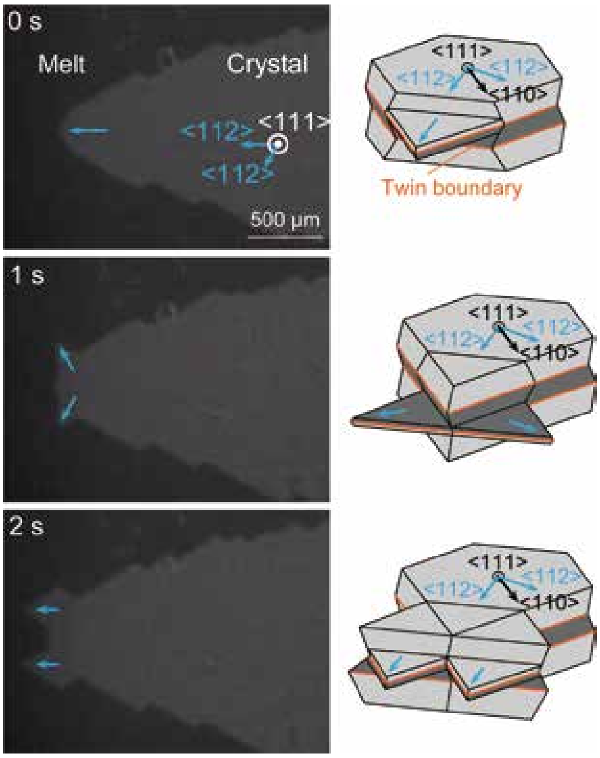

Fig. 1 *In situ* observation of the dendrite growth in GaSb. Schematics of the growth process are shown next to photographic images.

References

[1] K. Shiga, M. Kawano, K. Maeda, H. Morito, and K. Fujiwara, Scr. Mater. **168**, 56 (2019).

Keywords: crystal growth, grain boundaries, solar cells
Keiji Shiga (Crystal Physics Research Laboratory)
E-mail: kshiga@imr.tohoku.ac.jp
URL: http://www.imr.tohoku.ac.jp/en/about/divisions-and-centers/research-division/02.html

Discovery of Magnetic Field-Induced Pyroelectricity above 40 T in Multiferroic $LiNiPO_4$

A new magnetically ordered and pyroelectric phase has been discovered in multiferroic $LiNiPO_4$ in the course of determining its magnetization and a direct measurement of electric polarization in pulsed high magnetic fields up to 56 T. Pulsed-field Laue neutron diffraction up to 42 T revealed that commensurate canted antiferromagnetic order was realized in this newly observed phase. A model was proposed to explain how the magnetoelectric effect was driven by the canted antiferromagnetic order.

Multiferroic materials, in which magnetic and electric effects are simultaneously realized, are believed to be crucial for achieving cross-control between magnetism and electricity. There are three representative theoretical models explaining multiferroicity in multiferroic materials, namely, the spin current model based on the inverse Dzyaloshinskii-Moriya (DM) interaction, spin-dependent *p-d* hybridization model, and exchange striction model.

Multiferroic $LiNiPO_4$ is an attractive compound because it exhibits a rich variety of magnetic phases. In this material, a linear magnetoelectric (ME) effect is observed along the *a*- and *c*-axes below 20.8 K when a magnetic field is applied along the *c*- and *a*-axes, respectively (Fig. 1(a)). This ME effect is driven by the non-collinear antiferromagnetic spin structure. Because this effect cannot be explained by any of the models mentioned above, it is worth studying $LiNiPO_4$ for a deeper understanding of multiferroicity in general.

Recently, we discovered the magnetic field-induced phase transitions in $LiNiPO_4$ at 37.6, 39.4, and 54 T and the re-entrant ME effects in its phases IV and VII, as shown in Fig. 1(a) [1,2]. We previously proposed a model in which the commensurate antiferromagnetic order generated the linear ME effect in phase IV [1]. On the other hand, the magnetic field dependence of electric polarization in phase VII was clearly different from that in phases I and IV, in which a constant and a quadratic term in the ME tensor played an important role (*i.e.,* phase VII was pyroelectric).

To investigate the magnetic structure in these newly observed phases, neutron diffraction measurements were performed under the pulsed high magnetic fields up to 42 T on the NOBORU at J-PARC (Ibaraki, Japan) [1,2]. The combination of the white beam of the spallation neutron and the pulsed field allowed scanning of a wide area of reciprocal space in high magnetic fields. Figures 1(b)–1(d) show the results of the neutron diffraction measurements at 4.2 K, where the magnetic field was applied along the *c*-axis. The incommensurate $\boldsymbol{K}$ = (0 2/3 0) was observed in phases V and VI, and the commensurate $\boldsymbol{K}$ = (0 1 0) was observed in phase VII [2]. A model was proposed based on the combination of the superexchange interaction, DM interaction, and elastic distortion, which comprehensively explained the ME effect of $LiNiPO_4$.

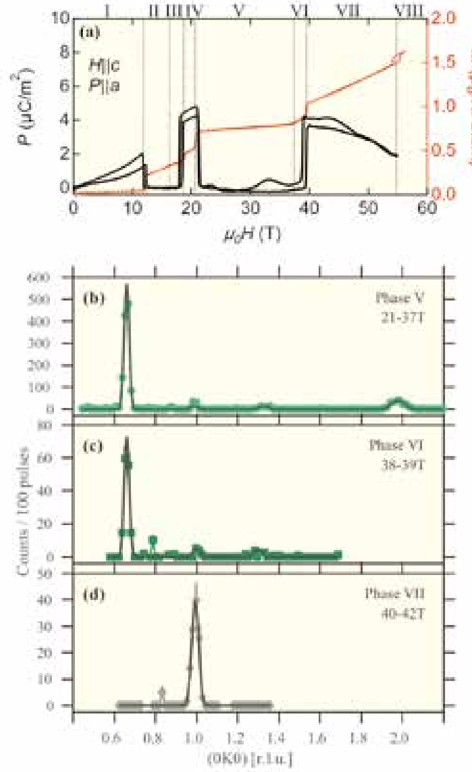

Fig. 1 (a) Dependence of magnetization and electric polarization along the *a*-axis measured at 4.2 K on the magnetic field. (b)–(d) Integrated intensities of the neutron Laue diffraction for each phase (V, VI, and VII).

References

[1] R. Toft-Petersen, E. Fogh, T. Kihara, J. Jensen, K. Fritsch, J. Lee, G. E. Granroth, M. B. Stone, D. Vaknin, H. Nojiri, and N. B. Christensen, Phys. Rev. B. **95**, 064221 (2017).

[2] E. Fogh, T. Kihara, R. Toft-Petersen, M. Bartkowiak, Y. Narumi, O. Prokhnenko, A. Miyake, M. Tokunaga, K. Oikawa, M. K. Sørensen, J. C. Dyrnum, H. Grimmer, H. Nojiri, and N. B. Christensen, Phys. Rev. B **101**, 024403 (2020).

Keywords: multi-ferroics, neutron scattering, high magnetic field

Takumi Kihara (Magnetism Research Laboratory)
E-mail: t_kihara@imr.tohoku.ac.jp
URL: http://www.hfpm.imr.tohoku.ac.jp/index.html

Phononic Thermal Hall Effect in Diluted Terbium Oxides

Thermal Hall effect is the deflection of thermal current depending on the sign of the magnetic field. The unconventional mechanism of the thermal Hall effect in magnetic insulators has generated considerable interest. Herein, the phononic mechanism of the thermal Hall effect in terbium oxides has been demonstrated by magnetic dilution.

In dielectrics, charge-neutral excitations such as phonons and magnetic excitations carry the heat current. The Lorentz force, which is the origin of the ordinary Hall effect, does not act on these charge-neutral particles. However, similar to the anomalous Hall effect in itinerant ferromagnets, it is expected that the charge-neutral heat current is deflected by the spin-orbit interaction in magnetic dielectrics. Strohm *et al.* first reported the thermal Hall effect in a paramagnetic dielectric, $Tb_3Ga_5O_{12}$ [1]. The thermal Hall effect has subsequently been observed in several magnetic dielectrics [2,3]. While this mechanism in some dielectrics can be explained by the Berry-phase-induced magnon Hall effect due to the Dzyaloshinskii-Moriya interaction [2], the mechanisms for other materials are not well understood. In particular, the thermal Hall effect observed in the paramagnetic state of some frustrated magnets [3] has two possible mechanisms, *i.e.,* the phonon Hall effect and the Hall effect due to exotic magnetic excitations, which are quite difficult to differentiate. Here, we propose that the dilution of the magnetic moment is useful for clarifying this issue. In the case of exotic magnetic excitation, the magnetic dilution should largely suppress the thermal Hall effect because the heat current is carried by a magnetic interaction. On the other hand, the phonon Hall effect is induced by the deflection of the phonon current originating from the local magnetoelastic coupling and the effect of magnetic dilution is more gradual.

The dilution effect of the thermal Hall effect in $Tb_2Ti_2O_7$ has been studied previously [4]. Hirschberger *et al.* observed a large thermal Hall effect in $Tb_2Ti_2O_7$ below 100 K [3]. Figure 1 shows the magnetic field dependence of thermal Hall conductivity divided by temperature at various temperatures for $(Tb_{0.3}Y_{0.7})_2Ti_2O_7$, in which the magnetic terbium ions are diluted with nonmagnetic yttrium ions. It is evident from the plots that there was finite thermal Hall conductivity for the diluted sample below 80 K.

The magnitude of the thermal Hall effect was comparable or even larger than that in pristine $Tb_2Ti_2O_7$. The dependence of the thermal Hall effect on the magnetic field was quite similar to that of magnetization in a Curie-type paramagnet, for which the dependence of magnetization on temperature and magnetic field is described by the Brillouin function. In fact, the dependence on magnetic field can be scaled by paramagnetic magnetization derived from the Brillouin function (dashed lines). This indicates that the magnetic scattering of phonons is the mechanism of the thermal Hall effect.

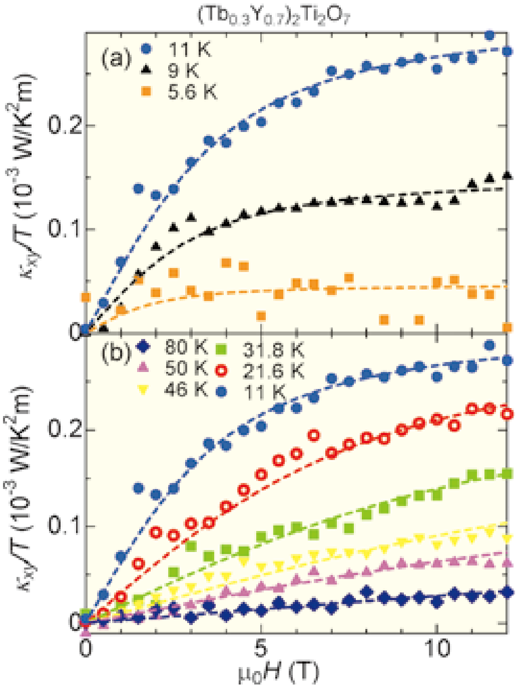

Fig. 1 (a), (b) Dependence of thermal Hall conductivity divided by temperature on the magnetic field for $(Tb_{0.3}Y_{0.7})_2Ti_2O_7$ at various temperatures. The dashed lines indicate the result of fitting with the Brillouin function.

References

[1] C. Strohm, G. L. J. A. Rikken, and P. Wyder, Phys. Rev. Lett. **95**, 155901 (2005).

[2] Y. Onose, T. Ideue, H. Katsura, Y. Shiomi, N. Nagaosa, and Y. Tokura, Science **329**, 297 (2010).

[3] M. Hirschberger, J. W. Krizan, R. J. Cava, and N. P. Ong, Science **348**, 106 (2015).

[4] Y. Hirokane, Y. Nii, Y. Tomioka, and Y. Onose, Phys. Rev. B **99**, 134419 (2019).

Keywords: magnetism, frustrated spin system, insulator

Yoshinori Onose (Quantum Functional Materials Physics Research Laboratory)
E-mail: onose@imr.tohoku.ac.jp
URL: http://www.imr.tohoku.ac.jp/en/about/divisions-and-centers/research-division/08.html

Molecular Dynamics Simulation of Wear Process in Diamond-Like Carbon for Low-Friction and High-Durability Material Design

Low-friction and high-durability material design requires a deep understanding of multi-physics phenomena, such as “chemical reaction” and “friction, impact, and stress.” We investigated the friction of diamond-like carbon (DLC) asperities using a reactive molecular dynamics simulator developed by us, which can consider tribochemical reactions. Further, we elucidated the atomic-scale chemical wear of DLC through the generation of hydrocarbon molecules.

Super-low-friction and high-wear-resistant technologies are important not only for reducing energy loss but also for improving the durability of industrial machines. Accordingly, diamond-like carbon (DLC) is a promising solid lubricant due to its low friction. The friction mechanism of DLC depends on multi-physics phenomena such as “chemical reaction” and “friction, impact, and stress,” and thus is difficult to elucidate. The tight-binding quantum chemical molecular dynamics (MD) code developed by us has already elucidated a low-friction mechanism and succeeded in designing tribology materials. However, this methodology cannot consider the wear process, as the model size is limited to a few thousand atoms. Thus, we developed a reactive MD simulator for friction, which can consider tribochemical reactions. Further, we succeeded in elucidating the wear process of DLC asperities using a model with several tens of thousands of atoms [1-3].

Figure 1 shows the wear process of the two DLC asperities simulated using our MD code. After the contact of the DLC asperities during the sliding, hydrocarbon molecules such as CH_4, C_2H_4, C_2H_6, etc. are generated and evaporated from the friction interface, indicating the atomic-scale chemical wear of DLC (Fig. 1c). In our previous small model, we could only observe bond generation and dissociation at the friction interface; we could not observe the generation and evaporation of hydrocarbon molecules. The evaporation of hydrocarbon molecules by chemical wear was proved using *in situ* experiments. We employed a quadrupole mass spectrometer (QMS) in a vacuum chamber, which can perform the *in situ* detection of the molecules generated during friction (Fig. 1d). The QMS detection also showed the generation of hydrocarbon molecules such as CH_4, C_2H_4, and C_2H_6 during the friction of DLC and the order of the number of generated molecules is $CH_4 > C_2H_4 > C_2H_6$. Thus, the order of the number of evaporated molecules obtained through our simulation is also consistent with the experiments, indicating that the increase in the model size enables the direct comparison of simulations and experiments.

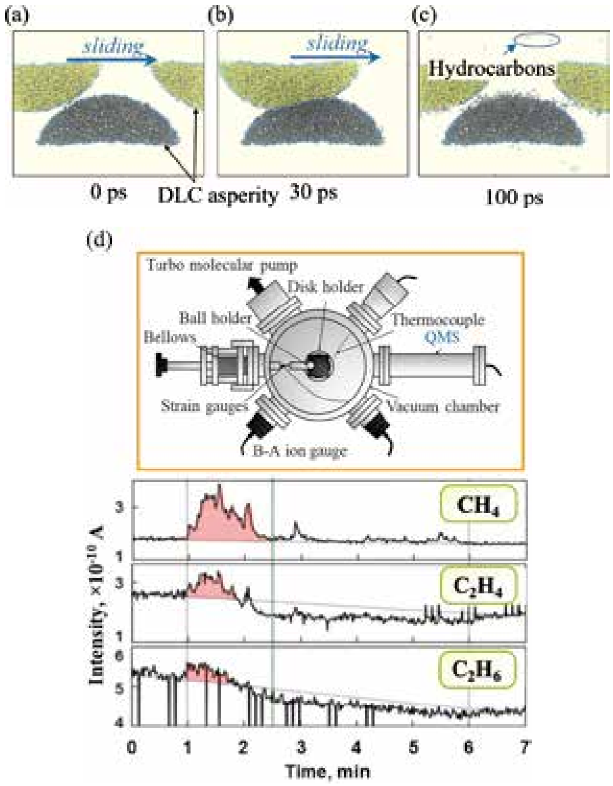

Fig. 1 Friction snapshots of DLC asperities at (a) 0, (b) 30, and (c) 100 ps. (d) QMS detection results for each molecule during the friction experiment of DLC.

References

[1] Y. Wang, N. Yamada, J. Xu, J. Zhang, Q. Chen, Y. Ootani, Y. Higuchi, N. Ozawa, M.-I. D. B. Bouchet, J. M. Martin, S. Mori, K. Adachi, and M. Kubo, Sci. Adv. **5**, eaax9301 (2019).

[2] Y. Wang, J. Xu, Y. Ootani, N. Ozawa, K. Adachi, and M. Kubo, Carbon **154**, 7 (2019).

[3] J. Zhang, Y. Wang, Q. Chen, Y. Su, J. Xu, Y. Ootani, N. Ozawa, K. Adachi, and M. Kubo, J. Comput. Chem. Jpn. **18**, 103 (2019).

Keywords: simulation, molecular dynamics, interface

Momoji Kubo (Materials Design by Computer Simulation Research Laboratory)
E-mail: momoji@imr.tohoku.ac.jp
URL: http://www.simulation.imr.tohoku.ac.jp/eng/index.html

Detection of the Phase Separation of Thermally Aged and Neutron-Irradiated Fe-Cr Binary Alloys Using Positron Annihilation

The Fe-Cr system is the basis for important engineering materials known as ferritic stainless steels, which are heat-resistant ferritic steels that are suitable as advanced structural materials for fission and fusion reactors. We detect an atomic-scale phase transition in a thermally aged and neutron-irradiated Fe-Cr system by using positron annihilation spectroscopy.

Fe-Cr alloys are susceptible to embrittlement at 748 K (475 °C) after thermal aging at approximately 748 K due to a phase transition where the ferrite phase decomposes into Fe- and Cr-rich ones. As shown in Fig. 1, increases in hardness after thermal aging at 748 K can be observed in the $Fe_{1-x}Cr_x$ alloys for $0.15 < x < 0.90$.

The normalized W-parameters evaluated using the coincident Doppler broadening (CDB) measurements in positron annihilation spectroscopy for the $Fe_{1-x}Cr_x$ alloys before and after aging are shown in Fig. 2. These experimental results and *ab-initio* calculation results showed a preferential position annihilation (PPA) of Fe atoms by considering the effect of the first- and second-nearest neighbor atoms. After aging at 748 K, the formation of isolated Fe atoms in the Cr-rich phases enhanced the PPA and increased the W-parameter.

The formation of Fe-rich phases and the changes in the interface conditions between the Fe- and Cr-rich phases also influenced the W-parameter. The progress of phase separation in the Fe-Cr binary alloys was detected *via* positron annihilation CDB measurements.

The phase separation of Fe-Cr alloys after neutron irradiation at 573 K was also detected *via* positron annihilation CDB measurements [2]. The PPA of the Fe-rich phase can affect the detection of vacancy clusters in Fe-Cr alloys using positron annihilation lifetime spectrometry.

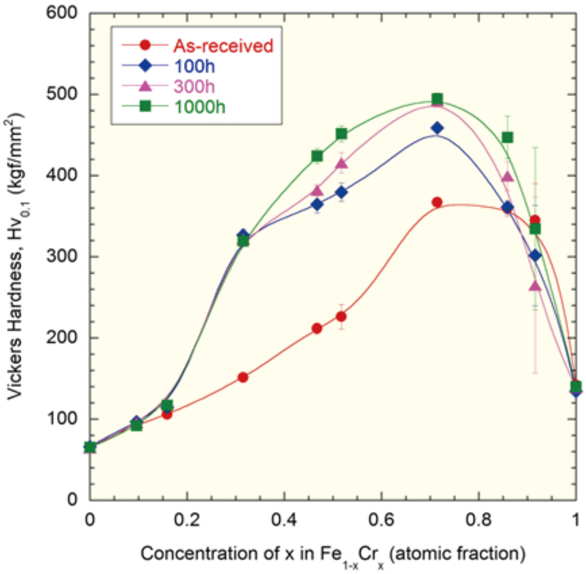

Fig. 1 Cr dependence of Vickers hardness in Fe-Cr binary alloys [1]

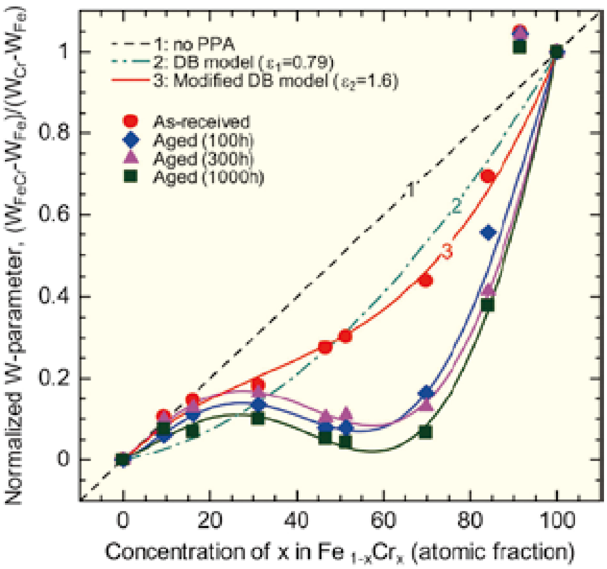

Fig. 2 Cr dependence of the normalized W-parameter of Fe-Cr alloys before and after thermal aging at 475 °C [1]

References

[1] R. Kasada and K. Sato, Philos. Mag. Lett. **99**, 360 (2019).

[2] Y. Noshita, K. Sato, H. Yamashita, R. Kasada, Q. Xu, M. Hatakeyama, and S. Sunada, Nucl. Mater. Energy **15**, 175 (2018).

Keywords: nuclear materials, strength, positron annihilation

Ryuta Kasada (Nuclear Materials Engineering Research Laboratory)
E-mail: r-kasada@imr.tohoku.ac.jp
URL: http://www.imr.tohoku.ac.jp/ja/about/divisions-and-centers/research-division/13.html

Effect of a Substrate on the Nucleation and Growth of Colloidal Crystals

Substrate effects on the nucleation and growth of colloidal crystals have been successfully demonstrated. Interactions between the colloidal particles and substrate were found to play an important role in nucleation, which is related to interfacial free energy. Further, it was found that lattice mismatch between the substrate and epitaxial layers had a significant effect on nucleation and growth. These findings may help achieve sophisticated control over the growth of colloidal crystals.

High-quality and large-sized crystals are desired for the versatile device applications of colloidal crystals. To this end, control over their nucleation and growth is required. Herein, the effects of the substrate on the nucleation and growth of colloidal crystals are described.

The nucleation rates, *J*, of two-dimensional (2D) colloidal crystals on uncoated cover glass, Pt-coated cover glass, and Au-coated cover glass were measured [1]. Among the three substrates, the *J* value of the uncoated cover glass was the largest, while it was the smallest for the Pt-coated glass under the same supersaturation conditions. The interfacial free energy change, $\Delta\sigma$, was obtained from the nucleation rate based on the classical nucleation theory. It revealed that the uncoated and Pt-coated cover glasses possessed the smallest and largest $\Delta\sigma$, respectively. Since $\Delta\sigma$ originates from the bond energy in atomic crystals, we deduced that it is related to the interactions between the colloidal particles and the substrate. The interactions between them are determined by surface force measurements using atomic force microscopy. The results showed that the adhesive force between the particles and uncoated cover glass was the weakest, while that for the Pt-coated sample was the strongest. A larger attractive interaction between the colloidal particles and the substrate yielded a higher $\Delta\sigma$, and thus a smaller *J*. Further. the interaction between the particles and substrate had a great influence on the heterogeneous nucleation rate of the colloidal crystals.

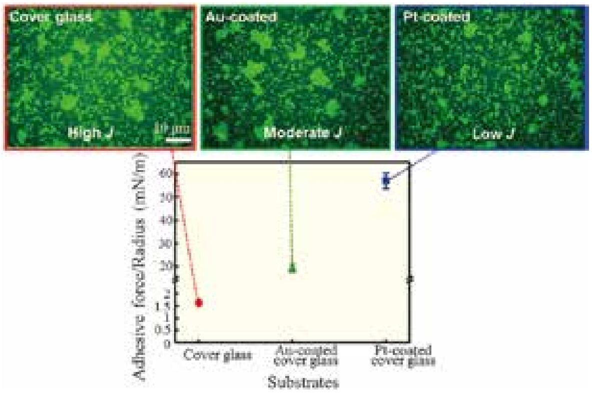

Fig. 1 Particle interaction and nucleation rate for three different substrates.

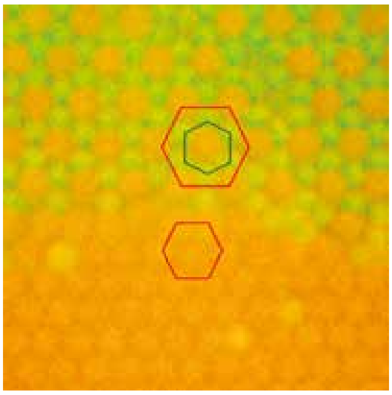

Fig. 2 One-dimensional heteroepitaxy of binary colloidal crystals with AB_2 structure.

The substrate effect was also recognized in the growth of binary colloidal crystals (BCCs). Owing to their tunable material properties, BCCs are highly desired for many applications. We have investigated the detailed growth process of BCCs in which depletion forces were induced between the particles by adding a polymer [2]. An AB_2 superlattice phase (A: large, B: small) was grown under various solution conditions, including various large-to-small particle ratios and polymer concentrations. *In-situ* observations revealed that BCCs typically grew *via* one-dimensional heteroepitaxy, which differs from the conventional colloidal epitaxial growth, demonstrating a novel technique to control the growth of BCCs.

References

[1] S. Guo, J. Nozawa, M. Mizukami, K. Kurihara, A. Toyotama, J. Yamanaka, H. Niinomi, J. Okada, and S. Uda, Cryst. Growth Des. **19**, 3215 (2019).

[2] J. Nozawa, S. Uda, A. Toyotama, J. Yamanaka, J. Okada, and H. Niinomi, Cryst. Growth Des. **20**, 3247 (2020).

Keywords: colloid, nucleation & growth, epitaxial growth

Jun Nozawa (Crystal Chemistry Research Laboratory)
E-mail: nozawa@imr.tohoku.ac.jp
URL: http://www.uda-lab.imr.tohoku.ac.jp/index-e.html

Complex Hydride Lithium Superionic Conductor for High-Energy-Density Lithium-Metal-Based All-Solid-State Batteries

The complex hydride lithium superionic conductor, 0.7Li(CB_9H_{10})–0.3Li($CB_{11}H_{12}$), achieved by designing structures of hydrogen clusters (complex anions), showed excellent stability against lithium metal and a high conductivity of 6.7 × 10^{-3} S cm^{-1} at 25 °C. This material enables lithium-metal-based all-solid-state batteries with the highest energy to date.

Lithium metal is widely believed to be the ultimate anode material for rechargeable batteries because it has the highest theoretical capacity (3860 mAh g^{-1}) and the lowest potential (–3.04 V vs. standard hydrogen electrode) among known anode materials [1]. Complex hydrides have received a lot of attention in making it possible to use the lithium metal anode because of their outstanding chemical and electrochemical stability against the lithium metal. However, because of their low ionic conductivity, using complex hydrides with the lithium metal anode has never been attempted in practical batteries.

In an effort to overcome the chronic drawbacks of complex hydrides and also realize lithium-metal-based batteries, we developed a new complex hydride lithium superionic conductor, 0.7Li(CB_9H_{10})–0.3Li($CB_{11}H_{12}$) [2]. The superionic conductivity was achieved by stabilizing the high temperature (high-T) phase of the complex hydride containing *closo*-type (cage-like) complex anions (Fig. 1a). Li(CB_9H_{10}) was used as the host starting material for the stabilization of the high-T phase because of its low phase transition temperature (90 °C) and high lithium ion conductivity, approaching 10^{-1} S cm^{-1} for the high-T phase. Our structural characterizations clarified that the high-T phase of Li(CB_9H_{10}) was stabilized by the partial substitution of $[CB_9H_{10}]^-$ with $[CB_{11}H_{12}]^-$.

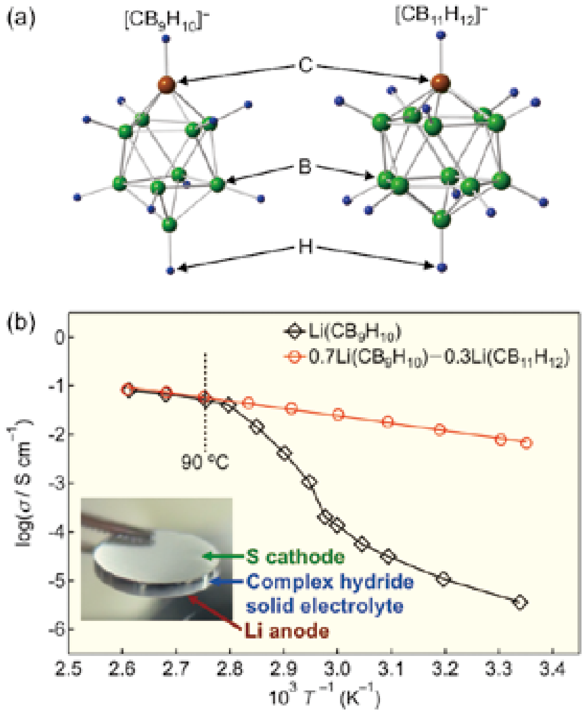

Fig. 1 (a) Structures of *closo*–type (cage–like) complex anions, $[CB_9H_{10}]^-$ and $[CB_{11}H_{12}]^-$. (b) Arrhenius plots of the lithium ion conductivities of Li(CB_9H_{10}) and 0.7Li(CB_9H_{10})–0.3Li($CB_{11}H_{12}$). Inset shows the all-solid-state Li–S battery.

0.7Li(CB_9H_{10})–0.3Li($CB_{11}H_{12}$) did not show any phase-transition-derived changes in conductivity and a linear increase in the logarithmic values (Fig. 1b). At temperatures above 90 °C, the conductivities of 0.7Li(CB_9H_{10})–0.3Li($CB_{11}H_{12}$) matched well with those of Li(CB_9H_{10}). More importantly, the lithium ion conductivity at 25 °C of 0.7Li (CB_9H_{10})–0.3Li($CB_{11}H_{12}$) was 6.7 × 10^{-3} S cm^{-1}, which is the highest value reported to date for complex hydride lithium ion conductors.

The developed complex hydride has several advantages as a solid electrolyte in all-solid-state batteries. In particular, its intrinsic stability with the lithium metal anode enables facile and stable lithium ion transfer at the interface with negligible resistance (<1 Ω cm^2). Additionally, the high ionic conductivity of 0.7Li(CB_9H_{10})–0.3Li($CB_{11}H_{12}$) coupled with its stability with the lithium metal results in a stable cycling of the high-energy-density all-solid-state lithium–sulfur (Li–S) batteries, even near room temperature.

References

[1] D. Lin, Y. Liu, and Y. Cui, Nat. Nanotechnol. **12**, 194 (2017).

[2] S. Kim, H. Oguchi, N. Toyama, T. Sato, S. Takagi, T. Otomo, D. Arunkumar, N. Kuwata, J. Kawamura, and S. Orimo, Nat. Commun. **10**, 1081 (2019).

Keywords: hydride, ionic conductor, energy storage

Sangryun Kim and Shin-ichi Orimo (Hydrogen Functional Materials Research Laboratory)
E-mail: sangryun@imr.tohoku.ac.jp
URL: http://www.hydrogen.imr.tohoku.ac.jp/en/index.html

Electronic Materials

IMR KINKEN Research Highlights 2020

Electrical Manipulation of Magnetization in Topological Semimetals

We theoretically study the spin-transfer torque induced by an electric field and analyze the dynamics of the magnetic domain walls in magnetic Weyl semimetals. Using several models for magnetic Weyl semimetals, we predict that the spin-transfer torque can be significantly enhanced. Moreover, due to the suppressed longitudinal conductivity by thin domain-walls, the dissipation by Joule heating associated with the spin-transfer torque becomes much smaller than that in bulk metallic ferromagnets. Consequently, domain wall motion can be efficiently controlled with low energy consumption in Weyl semimetals, as required for spintronic devices.

The electric control of spin magnetization can potentially be used in next-generation magnetic devices, allowing information to be written electronically. For instance, the magnetic racetrack memory has been proposed as a promising application of current-induced spin torque to spintronics devices. However, the sizeable current density required to operate the device limits its efficiency because of Joule heating, thus impeding its commercial application. Hence, more efficient methods of controlling magnetization are indispensable for practical applications.

To determine whether magnetic Weyl semimetals may be used in low-energy-consumption magnetic devices, we theoretically studied the spin torque acting on inhomogeneous local magnetization by computing the non-equilibrium spin density induced by applied electric fields [1,2,3]. We developed and employed a lattice model of a candidate Weyl semimetal, $Co_3Sn_2S_2$ [2], and numerically calculated the induced spin density. We derived the dynamics of the domain wall driven by the current-induced spin torque. The estimated velocity of a domain wall is one order of magnitude larger than that in conventional ferromagnetic metals [1,2].

Figure 1 shows the model and the electronic structures of the system. The conduction and valence bands are in contact at several points, around which the energy dispersion is linear. These results are consistent with those of first-principles calculations.

To analyze the dynamics of the domain wall, we employed Thiele's approach to map the Landau–Lifshitz–Gilbert equation to the equation of motion for the center coordinates of the domain wall and calculated a domain wall velocity that is one order of magnitude larger than that of the ferromagnetic nanowire. When the magnetization texture varies rapidly, the spin-transfer torque does not depend on the impurity-scattering relaxation time. In the Weyl semimetal phase, the longitudinal conductivity is very small because of the vanishing density of states; therefore, dissipation due to Joule heating is suppressed. Consequently, domain wall motion in the Weyl semimetal can be controlled much more efficiently than in conventional magnets. Magnetic Weyl semimetals can overcome the challenge of energy consumption for next-generation information and communication technology and are new candidates for high-performance magnetic devices.

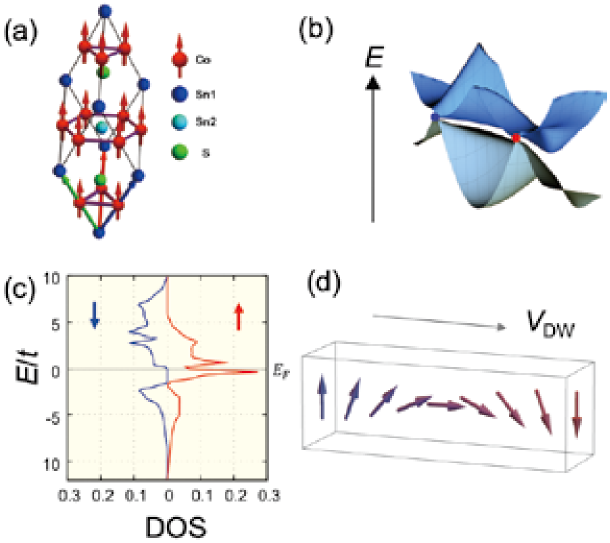

Fig. 1 (a) Crystal lattice structure of the magnetic Weyl semimetal $Co_3Sn_2S_2$. (b) Energy band dispersion. (c) Density of state (DOS). (d) Domain wall motion.

References

[1] D. Kurebayashi and K. Nomura, Sci. Rep. **9**, 5365 (2019).

[2] A. Ozawa and K. Nomura, J. Phys. Soc. Jpn. **88**, 123703 (2019).

[3] S. Kim, D. Kurebayashi, and K. Nomura, J. Phys. Soc. Jpn. **88**, 083704 (2019).

Keywords: spintronics, spin transfer, topological insulator

Kentaro Nomura (Theory of Solid State Physics Research Laboratory)
E-mail: nomura@imr.tohoku.ac.jp
URL: http://www.bauer-lab.imr.tohoku.ac.jp/?page=&lang=en

The Beginning of Paramagnetic Spintronics

In spintronics, paramagnetic insulators have been believed to be unimportant materials. Here, we show that a paramagnetic $Gd_3Ga_5O_{12}$, the most typical substrate for growing magnets, is a very good spin conductor. The unique advantages of paramagnets are expected to draw interest and open a new era for paramagnetic spintronics.

Exploring new materials for efficient spin transport is important in spintronics. In magnets, spin waves, the collective motion of magnetization supported by strong exchange interactions, carry spin current for long distances. However, paramagnets with weak exchange interactions are considered useless materials in spintronics.

In the present study [1], we report the observation of long-range spin transport in paramagnetic insulators. We used the paramagnetic insulator $Gd_3Ga_5O_{12}$ (GGG), which exhibits a large field-induced magnetization M at low temperatures T under high magnetic fields B. The device consists of two Pt contacts, which are electrically separated from each other, on a GGG slab (Fig. 1, top). We measured the voltage across the right Pt contact while applying charge current to the left Pt contact. The applied current drives the spin Hall effect (SHE), a charge to spin conversion phenomenon, and injects spin current into GGG. The spin current propagates and generates a voltage signal at the other contact *via* the inverse process of SHE.

The bottom panel of Fig. 1 shows the B dependence of the voltage signal (V) at 300 K and 5 K. When B was applied, we found a clear V signal at 5 K, but no signal appeared at 300 K. V increases with increasing B. The shapes of V are consistent with those of M of GGG. From the systematic measurements, we concluded that the observed signal is evidence of the long-range spin transport of the paramagnetic GGG.

Considering the results of the experiments and the model, we found that GGG exhibits a better spin conductivity than the magnet YIG, which is known as the best spin conductor. We speculate that long-range dipole interaction is a plausible mechanism of the spin transport. When GGG is exposed to high B at low T, it acquires a large M and can support spin waves mediated by dipole interactions even in paramagnetic insulators.

This result expands the material class of spintronics to paramagnetic insulators (which have unique advantages), and develops the new research field of *Paramagnetic Spintronics*.

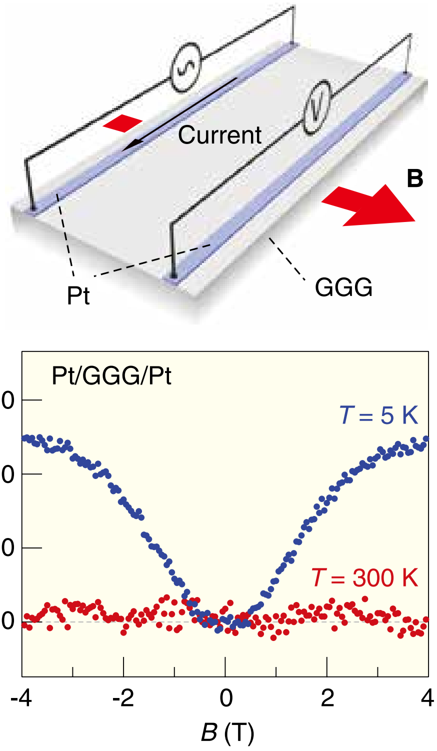

Fig. 1 (top) Schematic illustration of the experimental setup. Spin current in GGG is excited and detected electrically at the Pt contacts using direct and inverse spin Hall effects. (bottom) Magnetic field dependence of the signal. At 5 K, the signal appears when magnetic field is applied.

References

[1] K. Oyanagi, S. Takahashi, L. J. Cornelissen, J. Shan, S. Daimon, T. Kikkawa, G. E. W. Bauer, B. J. van Wees, and E. Saitoh, Nat. Commun. **10**, 4740 (2019).

Keywords: spintronics, spin current, spin dynamics

Koichi Oyanagi and Eiji Saitoh (Surface and Interface Research Laboratory)
E-mail: k.0yanagi444@gmail.com, eizi@ap.t.u-tokyo.ac.jp
URL: http://saitoh.t.u-tokyo.ac.jp/

Make It Flexible! — A Magnetic Alloy for Flexible Hall Sensors

With the rapid technological development toward Internet-of-Things, there has been an increasing demand for magnetic-field sensors with added functionality. A simple Fe-Sn magnetic alloy was demonstrated to be a promising material for the development of flexible magnetic-field sensors. The operating principle based on the anomalous Hall effect, which has not been exploited yet in flexible magnetic-field sensors, is now in the limelight.

Magnetic-field sensors capable of electrically detecting a magnetic field are widely used in modern electronics. Their applications include the monitoring of electric current and motion of micromechanical parts and use as an electrical compass. One such device is a Hall sensor [1], which employs the ordinary Hall effect in semiconductors such as Si and GaAs. To generate a large output Hall voltage under a given magnetic field, low-carrier and high-mobility semiconductors must be used. This inevitably involves high-temperature epitaxial growth of the semiconductor films, making it difficult to integrate the device directly on flexible electronics circuits that are essential in the emerging Internet-of-Things (IoT) technology.

A similar Hall-sensor function can, in principle, be obtained using the anomalous Hall effect (AHE). As this effect is related to magnetization and electronic band structure, it can be large in a metal [2]. However, magnetic metals with sufficiently large and linear AHE responses against the magnetic field have not been discovered as yet. In this study, we found that thin films of environmentally friendly Fe-Sn alloy are appealing as a material for the AHE-type Hall sensor [3,4]. The AHE in the Fe-Sn alloy films is larger than that observed in most metals (Fig. 1) and comparable to that recently reported for the single crystal of kagome-lattice topological ferromagnet Fe_3Sn_2 [5]. The AHE characteristics (Hall voltage vs. magnetic field under a constant input current) showed thermally stable operation as a Hall sensor over a wide temperature range. The Fe-Sn alloy films could be grown at room temperature on various substrates, including a flexible polymer (Fig. 1 inset), using a scalable sputtering method. These features enabled us to perform a proof-of-concept experiment for a "flexible Hall sensor" (Fig. 1 inset) [3].

The mechanism explaining the large AHE in the room temperature-grown, rather disordered Fe-Sn alloy films, is not clear as yet. On the basis of the results of impurity doping [6], we proposed that the intrinsic AHE arising from the topological character of electronic bands [2] is operative in the Fe-Sn alloy films. Such a new degree of freedom in engineering Hall-sensor performance is a lucrative incentive for the utilization of magnetic materials, especially with topological features, in the next-generation electronic devices.

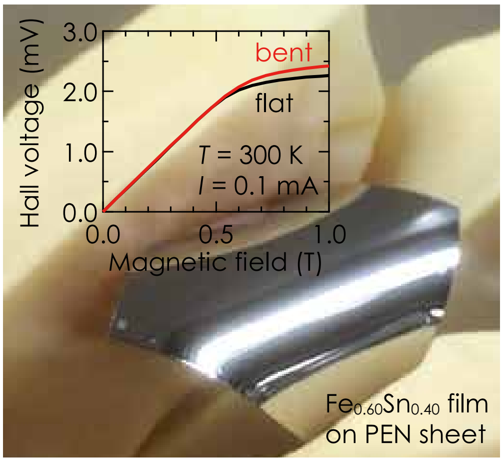

Fig. 1 40-nm-thick $Fe_{0.60}Sn_{0.40}$ alloy thin film sputtered on a flexible polyethylene naphthalate (PEN) sheet (area = 15 mm × 15 mm). Inset: AHE characteristics measured with and without mechanical bending.

References

[1] R. S. Popović, *Hall Effect Devices, 2nd ed.* (CRC Press, 2003).
[2] N. Nagaosa, J. Sinova, S. Onoda, A. H. MacDonald, and N. P. Ong, Rev. Mod. Phys. **82**, 1539 (2010).
[3] Y. Satake, K. Fujiwara, J. Shiogai, T. Seki, and A. Tsukazaki, Sci. Rep. **9**, 3282 (2019).
[4] J. Shiogai, Z. Jin, Y. Satake, K. Fujiwara, and A. Tsukazaki, Appl. Phys. Express **12**, 123001 (2019).
[5] L. Ye, M. Kang, J. Liu, F. von Cube, C. R. Wicker, T. Suzuki, C. Jozwiak, A. Bostwick, E. Rotenberg, D. C. Bell, L. Fu, R. Comin, and J. G. Checkelsky, Nature **555**, 638 (2018).
[6] K. Fujiwara, Y. Satake, J. Shiogai, and A. Tsukazaki, APL Mater. **7**, 111103 (2019).

Keywords: alloy, thin films, magnetic properties
Kohei Fujiwara (Low Temperature Physics Research Laboratory)
E-mail: kfujiwara@imr.tohoku.ac.jp
URL: http://mu.imr.tohoku.ac.jp/index_en.html

Lattice Dynamics Coupled to Electronic Ferroelectricity

Inelastic neutron scattering measurements on the molecular dimer-Mott insulator κ-(BEDT-TTF)$_2$Cu[N(CN)$_2$]Cl reveal a phonon anomaly over a wide temperature range. Starting from T_{ins} = 50-60 K, where the charge gap opens, low-lying optical phonon modes become over-damped upon cooling towards the antiferromagnetic ordering temperature T_N = 27 K, where a ferroelectric ordering at T_{FE} to T_N also occurs. Phonon damping decreases again when spins and charges are ordered below T_N, while no change on the lattice symmetry is observed across T_N. We attribute the phonon anomalies to structural fluctuations coupled to the degrees of freedom of charge and spin in BEDT-TTF molecules.

Conventional ferroelectrics (FE), which are driven by shifts in the atomic positions, are used in common electronic devices. Electrons and their interactions play the key role in electronic FE, which have gained popularity due to their ultrafast response and/or large magnetoelectric effect originating from electronic degrees of freedom. Recently, the simultaneous occurrence of FE and antiferromagnetic spin order in a dimer-Mott system κ-(BEDT-TTF)$_2$Cu[N(CN)$_2$]Cl (κ-Cl) has been observed. However, the origin of the electric dipoles in this compound is still disputed because of the lack of direct evidence from optical spectroscopy, which is sensitive to molecular charges. Given there is a finite electron-lattice coupling, fluctuations of the electric dipoles are expected to produce anomalies in the lattice dynamics that can be sensitively probed by neutron scattering. To study the phonon anomaly associated with charge disproportionation, we performed inelastic neutron scattering on deuterated single crystals of κ-Cl using the triple-axis spectrometers IN8 at ILL and PUMA at FRM2 [1].

Figure 1 shows the temperature dependence of the phonon intensity at Q = (603) and E = 1.5 meV obtained *via* the PUMA. The phonon intensity at low energies are enhanced when $T_N < T <$ 60 K. From the fitting of the constant-Q spectra to the damped harmonic oscillator function, we found that the low-lying optical phonon mode at 2.6 meV becomes overdamped over the temperature region. The onset temperature of phonon damping roughly coincides with the rapid increase in the electrical resistivity below T_{ins} = 50–60 K. Furthermore, phonon damping decreases again when spins and charges are ordered below $T_N = T_{FE}$ = 27 K, suggesting the close correlations among the lattice, spin, and charge. In addition, we found that the phonon anomaly is different from what is expected for conventional FE. First, the phonon intensity does not diverge at T_{FE}. Second, no change of the lattice symmetry is observed across T_{FE}. Thus, we attribute the phonon anomalies to structural fluctuations coupled to the degrees of freedom of charge and spin in the BEDT-TTF molecules. We consider these inelastic neutron scattering results as an important step that may trigger further systematic studies on lattice dynamics and its coupling to the electronic degrees of freedom of organic charge-transfer salts.

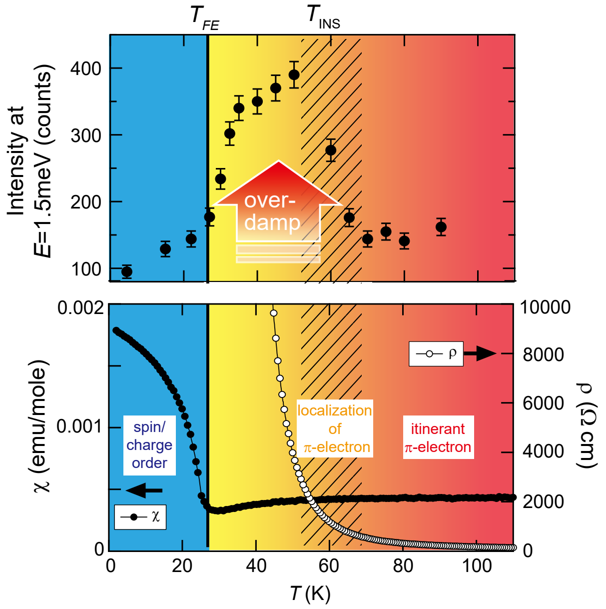

Fig. 1 (top) Temperature dependence of phonon intensity at Q = (603) and E = 1.5 meV and (bottom) electrical resistivity and DC magnetic susceptibility.

References

[1] M. Matsuura, T. Sasaki, S. Iguchi, E. Gati, J. Müller, O. Stockert, A. Piovano, M. Bohm, J. T. Park, S. Biswas, S. M. Winter, R. Valenti, A. Nakao, and M. Lang, Phys. Rev. Lett. **123**, 027601 (2019).

Keywords: organic, metal-insulator transition, neutron scattering

Takahiko Sasaki (Low Temperature Condensed State Physics Research Laboratory)
E-mail: takahiko@imr.tohoku.ac.jp
URL: http://cond-phys.imr.tohoku.ac.jp/index_e.html

Magnetism and Superconductivity in the T*-type Cuprates $La_{1-x/2}Eu_{1-x/2}Sr_xCuO_4$

Change in physical properties such as the magnetism and superconductivity of high-T_c cuprates in relation to their local structure is an interesting phenomenon. In this study, T*-type cuprates were synthesized and the superconductivity transition in these compounds after annealing was observed. The latter likely gave rise to additional oxygen atoms without inducing the magnetic transition, suggesting that magnetism played an important role in the formation of Cooper pairs in T*-type $La_{1-x/2}Eu_{1-x/2}Sr_xCuO_4$.

The local structure of high-T_c cuprates, in particular the oxygen sites near the copper sites, has generated significant research interest. High-T_c cuprates with “214” structures are known to have three types of isomers, *i.e.,* the so-called T-. T’-, and T*-type. In these families, physical properties such as magnetism and superconductivity often change after annealing, but the origin is unknown as yet. One of the possibilities is a change in the local structure associated with the apex oxygen site, which is one of the oxygen sites surrounding a copper site [1]. T*-type cuprates are ideal for investigating the relationship between the physical properties and local structure because in these compounds, a copper atom is surrounded by the five oxygen sites forming a pyramid-like cage.

Recently, we succeeded in synthesizing T*-type cuprates $La_{1-x/2}Eu_{1-x/2}Sr_xCuO_4$ (LESCO) and investigated their magnetism and superconductivity. Temperature dependencies of the resistivity of as-sintered (AS) and oxidation annealed (AN) T*-type LESCO are shown in Fig. 1 [2, 3]. While the superconducting transition was observed in the AN samples, the magnetic transition was absent. In contrast, the AS samples exhibited evidence for a disordered magnetic state below 10 K (Fig. 2). This is the first evidence for the effect of annealing on magnetism and superconductivity in LESCO.

To investigate the origin of superconductivity in LESCO, we performed muon spin rotation/relaxation (μSR) measurement on the AS and AN samples. Figure 2 shows the μSR spectra of AS- and AN-LESCO with $x = 0.14$ against temperature change. At low temperatures, a relaxation was observed in all AS-LESCO, whereas this anomaly was absent in all AN-LESCO. These experimental findings support the simultaneous development of (quasi-) static magnetism, and the resistivity at low temperatures suggests induced magnetism by the suppression of carrier mobility.

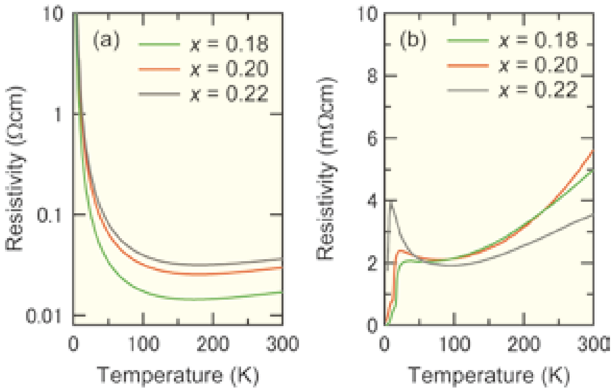

Fig. 1 Temperature dependence of the electrical resistivity for (a) AS- and (b) AN-LESCO with $x = 0.18$, 0.20, and 0.22 [3].

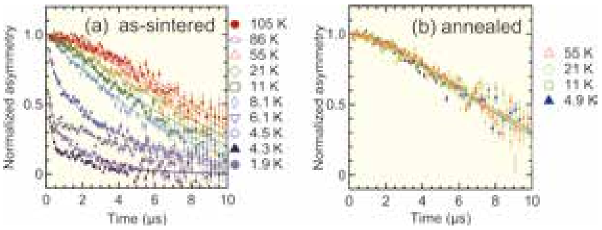

Fig. 2 Temperature dependence of μSR spectra in (a) AS- and (b) AN-LESCO with $x = 0.14$ [3].

References

[1] J. Akimitsu, S. Suzuki, M. Watanabe, and H. Sawa, J. J. Appl. Phys. **27**, L1859 (1988).

[2] M. Fujita, K. M. Suzuki, S. Asano, A. Koda, H. Okabe, and R. Kadono, JPS Conf. Proc. **21**, 011026 (2018).

[3] S. Asano, K. M. Suzuki, K. Kudo, I. Watanebe, A. Koda, R. Kadono, T. Noji, Y. Koike, T. Taniguchi, S. Kitagawa, K. Ishida, and M. Fujita, J. Phys. Soc. Jpn. **88**, 084709 (2019).

Keywords: superconducting, magnetism, electronic structure

Masaki Fujita (Quantum Beam Materials Physics Research Laboratory)
E-mail: qblab@imr.tohoku.ac.jp
URL: http://qblab.imr.tohoku.ac.jp/index-e.html

Development of Pixilated Scintillator Arrays and Eutectics for High-Resolution Radiation Imaging

Wafers of Tb-doped GAP/α-Al_2O_3 eutectic of size 25 × 25 mm^2 were fabricated *via* the micro-pulling-down method using an Ir crucible with a 25 × 25 mm^2 die. A prototype of an X-ray phase imaging detector was developed using a CMOS sensor with a fiber optic plate and eutectic wafer. We also successfully developed a radiation-imaging detector using a 0.1 × 0.1 mm^2-pixelated $Gd_3(Ga,Al)_5O_{12}$ (GAGG) scintillator combined with a silicon photomultiplier array made of 1 × 1 mm^2 channels.

High spatial resolution is desired for a radiation-imaging detector for alpha and beta particles, and gamma and X-rays. A pixelated scintillator can improve the spatial resolution of a scintillation imaging detector by reducing the light spread of the scintillator. For this type of radiation-imaging detector, the spatial resolution is sometimes limited by the pixel size of the scintillators and a scintillator array with a smaller pixel-size is desired. However, fabricating such a scintillator array manually is difficult. We reported two fabrication techniques for this purpose: fine cutting [1] and a rod-like eutectic structure [2,3].

The side view of the developed GAGG pixelated plate is shown in Fig. 1(a). The GAGG pixelated plate had the pixel size of 0.1 × 0.1 × 1 mm^3 with 0.05 mm slits between the pixels; thus, the pitch was 0.15 mm. The number of pixels was 53 × 53 and the total size of the GAGG pixel plate was 8 × 8 mm^2. The developed imaging detector resolved 0.1 × 0.1 mm^2 GAGG-pixels for Am-241 alpha particles.

Figure 2 shows the photographs of the grown eutectic and its scanning electron microscope (SEM) image. After optimizing the growth conditions such as seed size, pulling rate, atmosphere, insulator set-up, and temperature gradient along the growth direction, a prism-shaped eutectic could be fabricated (Fig. 2(b)). Figure 2(c) shows a cut and polished wafer of the Fig. 2(b) eutectic at the cross section. Optically transparent parts can be confirmed in more than 80% of the area on the 25 × 25 mm^2 wafer. Figure 2(d) shows a cut and polished sample of size 3 × 3 × 0.3 mm^3. The background of the surface of the sample shows bundles of optical fibers.

A prototype of an X-ray phase imaging detector was developed using a CMOS sensor with a fiber optic plate and a eutectic wafer. X-ray spots with a period of 8.24 μm were observed using the detector. X-ray phase imaging of the nylon ball was performed in this study. A phase change of approximately 2 μm could be confirmed in the air and nylon spherical interface. The X-ray phase imaging technique could be realized in the absence of absorption grating.

Fig. 1 Photo of the developed 0.1 mm pixel size GAGG plate (a) and the developed silicon photomultiplier (Si-PM)-based GAGG imaging detector optically coupled to a Si-PM array of channel size 1 mm (b)

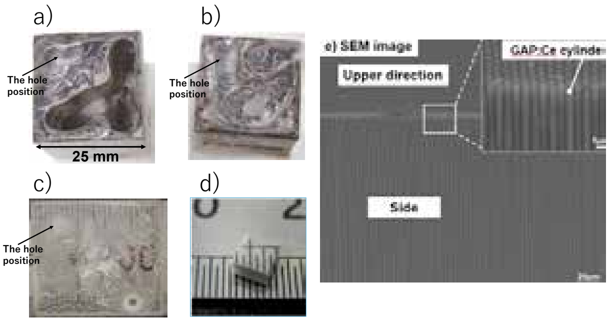

Fig. 2 Photographs of the grown eutectic (a) at the initial stage, (b) after optimization of the growth conditions, (c) cut and polished wafer of the (b) eutectic, (d) sample of size 3 × 3 × 0.3 mm^3, and (e) the SEM image of the eutectic.

References

[1] S. Yamamoto, J. Kataoka, K. Kamada, and A. Yoshikawa, Nucl. Instrum. Methods Phys. Res. A **919**, 125 (2019).

[2] K. Kamada, N. Yasui, Y. Ohashi, T. Den, H. Yamaguchi, A. Yamaji, Y. Shoji, M. Yoshisno, K. JinKim, S. Kurosawa, Y. Ohashi, Y. Yokota, and A. Yoshikawa, IEEE TNS **65**, 2036 (2018).

[3] A. Yoshikawa, K. Kamada, S. Kurosawa, Y. Yokota, A. Yamaji, V. I. Chani, Y. Ohashi, and M. Yoshino, J. Cryst. Growth **498**, 170 (2018).

Keywords: scintillator, crystal growth, radiation imaging

Akira Yoshikawa (Physics of Electronic Materials Research Laboratory)
E-mail: yoshikawa@imr.tohoku.ac.jp
URL: http://yoshikawa-lab.imr.tohoku.ac.jp/index-e.html

Structure Analysis of MnS_2, $MnSe_2$, and $MnTe_2$

The structures of the pyrite-type compounds such as MnS_2, $MnSe_2$, and $MnTe_2$, were determined by single crystal X-ray diffraction. The structural features of MnX_2 compounds (X = S, Se, and Te) were also discussed [1].

The pyrite-type structure, MX_2, is realized as a variety of chalcogen or pnictogen compounds (M = transition metal, X = S, Se, Te, P, As, and Sb). As depicted in Fig. 1, the pyrite-type structure is a 3D assembly of MX_6 octahedra, in which the M is solely bound to a single X in the X_2 molecule. This interesting structure may be featured by the variation of covalent X–X distances and ionic M-X distances. Figure 2 depicts M–X versus X–X distances in a variety of MX_2 pyrite-type compounds. As shorter M–X distances compared to X–X distances indicate diminishing characteristic as an X_2 molecule, the compounds located in the upper-left quadrant tend to exhibit a metallic luster and those located in the lower-right quadrant of the plot tend to exhibit a glass-like luster. Additionally, the variation of X–X distances realized in the MX_2 octahedron also reflects the MX_6 geometry. There are two short and long X–X edge distances in the MX_6 octahedron and the increase in the electronic polarization of the M cation leads to an increase in the $d(\mathrm{X{-}X})_l/d(\mathrm{X{-}X})_s$ ratio. Therefore, precise structural information would aid a discussion of the possible factors that lower the total energy in pyrite-type crystals.

The number of electrons in the d-orbital increases to d^5, d^6, d^7, and d^8 for Mn^{2+}, Fe^{2+}, Co^{2+}, and Ni^{2+}, respectively. In the low spin state, all electrons in Fe^{2+} occupy t_{2g} orbitals ($S = 0$), which is, evidently, a biased electron arrangement. In the high spin state, electrons in Mn^{2+} occupy all of the orbitals evenly ($S = 5/2$), which creates a spherical symmetry and its relatively large ionic size. As depicted in Fig. 2, the extent by which the M-S distance increases is highest for FeS_2, followed by CoS_2, NiS_2, and MnS_2. This result readily suggests the high spin state of Mn^{2+}. Analysis of the $d(\mathrm{X{-}X})_l/d(\mathrm{X{-}X})_s$ ratio indicates that MnS_2 exhibits the smallest distortion to the octahedral M-site. Considering that FeS_6 exhibits greater distortion than MnS_6, the difference in the spin states of FeS_2 and MnS_2 is also confirmed.

The $d(\mathrm{Mn{-}X})/d(\mathrm{X{-}X})$ ratios corresponding to S, Se, and Te decrease to 1.000 from S to Te and these results suggest a corresponding decrease in the molecular characteristics of the corresponding X_2 groups. The $d(\mathrm{X{-}X})_l/d(\mathrm{X{-}X})_s$ ratios increase as a function of the X–X distance, as suggested by the increase in the degree of octahedral distortion. However, the $d(\mathrm{X{-}X})_l/d(\mathrm{X{-}X})_s$ ratio corresponding to $MnTe_2$ is almost identical to that of FeS_2, and the distortion corresponding to $MnTe_6$ is large. This result readily suggests that the distortion of the M-site is not a major factor in the stability of spin states. This conclusion allows us to propose the idea that the factors that lower the total energy in MnS_2, $MnSe_2$, and $MnTe_2$ are primarily determined by the respective configurations of anions.

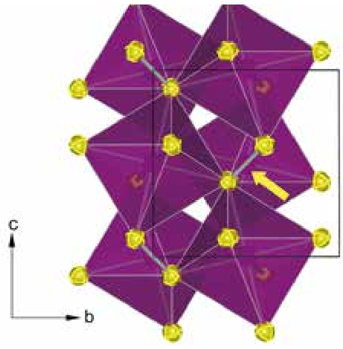

Fig. 1 Crystal structure of hauerite. The S-S bond (indicated by the yellow arrow) has been indicated in the middle of the unit cell.

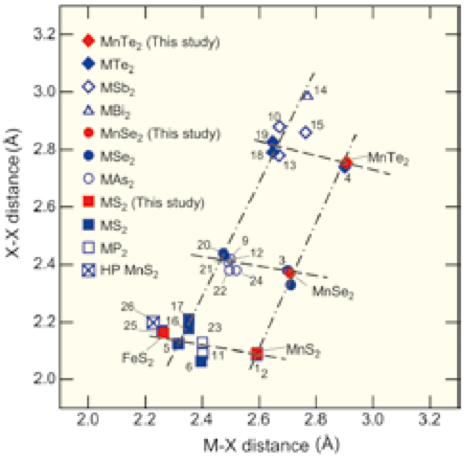

Fig. 2 M–X versus X–X distances in MX_2 pyrite-type compounds (M = metal ions, X = S, Se, Te, P, As, Sb, Bi).

References

[1] M. Tokuda, A. Yoshiasa, T Mashimo, H. Arima, H, Hongu, T. Tobase, A, Nakatsuka, and K. Sugiyama, Z. Kristallogr. Cryst. Mater. **234**, 371 (2019).

Keywords: X-ray diffraction (XRD), crystal structure, MnS_2

Makoto Tokuda (Chemical Physics of Non-Crystalline Materials Research Laboratory)
E-mail: tokuda@imr.tohoku.ac.jp
URL: http://www.imr.tohoku.ac.jp/en/about/divisions-and-centers/research-division/15.html

Host-Guest Hydrogen Bonding Influences Charge-Ordering in Magnetic Sponges

Electronic state modulation in magnetic frameworks represents an effective strategy for significantly changing their magnetism. We demonstrated that the dynamically changeable charge-ordered state in porous magnetic frameworks is affected by the host-guest hydrogen bonding between the host framework and lattice solvent molecules.

Chemo-responsive magnetism is one of the most desired functions in molecular magnets for potential applications in new types of memories, sensors, and switches. However, it is challenging to achieve drastic, large, and highly reversible functions in such materials. We recently proposed electronic state modulation (ESM) as a new mechanism to produce a large magnetic change in magnets. With ESM, the charge-ordered state of the magnetic framework is controlled depending on whether the guest molecules are present or not [1].

Here, we report a pseudo-polymorphic series of layered magnets, $[\{Ru_2(m\text{-}FPhCO_2)_4\}_2TCNQ(OMe)_2]\cdot n\text{DCE}$ (**1-*n*DCE**; m-FPhCO$_2^-$ = m-fluorobenzoate; TCNQ(OMe)$_2$ = 2,5-dimethoxyl-7,7,8,8-tetracyanoquinodimethane), consisting of two electron-donor (D) units of $[Ru_2(m\text{-}FPhCO_2)_4]$ and one acceptor (A) unit of TCNQ(OMe)$_2$ [2]. Three types of compounds having different D_2A charge-ordered states were distinguished by the amount of 1,2-dichloroethane (DCE) included as the crystallization solvent, namely, $[D^+–A^{2-}–D^+]_\infty$ for the fully solvated compound (pristine form; **1-4DCE**), $[D^+–A^{1.5-}–D^{0.5+}]_\infty$ for the solvent-free compound (**1**), and $[D^+–A^-–D]_\infty$ for a partially solvated intermediate state (**1-DCE** with $n \leq 1$). Compounds **1-4DCE**, **1** and **1-DCE** clearly had modified magnetism as well as their respective T_Cs; they were identified as a paramagnet, ferrimagnet with T_C = 30 K, and ferrimagnet with T_C = 88 K, respectively (Fig. 1a).

Notably, although **1** and **1-DCE** were isostructural in their framework, their charge-ordered states were modified. The key factor that allows these differences is a CH···O-type hydrogen bonding motif between DCE and the framework only found in **1-DCE** (Fig. 1b). To clarify the effect, density functional theory calculations were carried out. Consequently, a weak charge polarization of $–C^{\delta-}–H^{\delta+}$ in the guest DCE could provide a positive electrostatic field around the host framework to stabilize the orbital energies, where the host framework with DCE possesses a lower highest occupied molecular orbital (HOMO) energy level than that in a case without DCE (Fig. 1c). Hence, **1-DCE** with the CH···O-type hydrogen bonding motif stabilized the charge state of $[D^+–A^-–D]_\infty$.

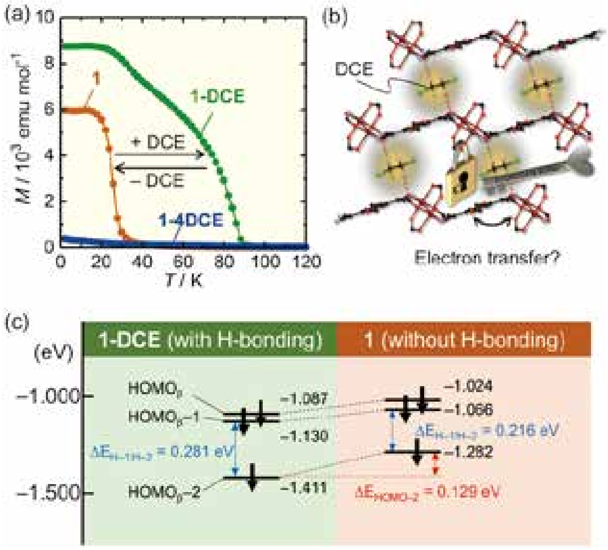

Fig. 1 (a) Temperature dependence of magnetization at H_{dc} = 100 Oe for **1-4DCE** (blue), **1-DCE** (green), and **1** (orange). (b) Crystal structure of **1-DCE**. (c) Calculated molecular orbitals energies around HOMO of the layered magnet with hydrogen bonding (**1-DCE**; left) and without hydrogen bonding (**1**; right) models.

The hydrogen bonding host-guest interactions could be quite useful as a trigger to control the electronic state (i.e., charge-ordered state) of the framework materials. Such a delicate system associated with host-guest interactions and subsequent electron transfers resembles the information transfer system in biological systems. Thus, the design of host-guest interactions in electronically conjugated systems is a promising strategy for the creation of dynamic functional electronic/magnetic materials whose electronic/magnetic, as well as dielectric, properties can be switched on demand by guest molecules.

References

[1] J. Zhang, W. Kosaka, K. Sugimoto, and H. Miyasaka, J. Am. Chem. Soc. **140**, 5644 (2018).

[2] J. Zhang, W. Kosaka, Y. Kitagawa, and H. Miyasaka, Angew. Chem. Int. Ed. **58**, 7351 (2019).

Keywords: computational materials science, magnetic properties, porosity

Jun Zhang and Hitoshi Miyasaka (Solid-State Metal-Complex Chemistry Research Laboratory)
E-mail: zhangjun@imr.tohoku.ac.jp, miyasaka@imr.tohoku.ac.jp
URL: http://www.miyasaka-lab.imr.tohoku.ac.jp/cn5/HOME-Eng.html

Overcoming Thermal Coarsening in Nanoporous Materials *via* High-Entropy Design

Controlling the feature sizes of three-dimensional bicontinuous nanoporous materials is essential for their advanced applications. However, the intrinsic coarsening of nanoporous materials naturally reduces their surface energy and leads to the deterioration of their physical properties over time. In this work, a novel 3DNP material is reported that could overcome thermal coarsening.

Stabilizing the feature sizes of three-dimensional bicontinuous nanoporous (3DNP) materials is challenging because their mature ligament size is inversely proportional to the melting point. Although 3DNP materials have outstanding physical properties because of their unique structure with open porous networks, the coarsening phenomenon leads to the degradation of physical properties over time.

The proposition for high-entropy alloys (HEA) is maximizing the configuration entropy to stabilize a multi-principle solid-solution alloy. Atomic size differences between constituent elements in HEA increases the activation energy for diffusion. In that context, a high-entropy design of nanoporous materials has the potential for achieving an exceptional stability against the coarsening.

To synthesize the 3DNP HEA, we utilized liquid metal dealloying (LMD), a unique technique to fabricate non-noble porous materials by preventing oxidation in a metallic melt. The high-entropy design of LMD based on the enthalpy of mixing is depicted in Figure 1a [1]. The composition of the 3DNP HEA was carefully established among elements immiscible with the Mg melt, and the selected TiVNbMoTa HEA was then alloyed with 75 at% miscible Ni. While Ni atoms were selectively dissolved in the Mg melt, the five immiscible elements rearranged their atomic configuration into the 3DNP structure.

The 3DNP HEA was able to preserve its nanoscale features under severe conditions. The average ligament size achieved in a unimodal porous structure was only 10 nm after 10 min at 837 K (Fig. 1b). The ring diffraction pattern proved the formation of *bcc* ligaments with various crystal orientations. Most of the ligaments consist of a few grains, and they form the polycrystalline 3DNP HEA scaffolds (Fig. 1c).

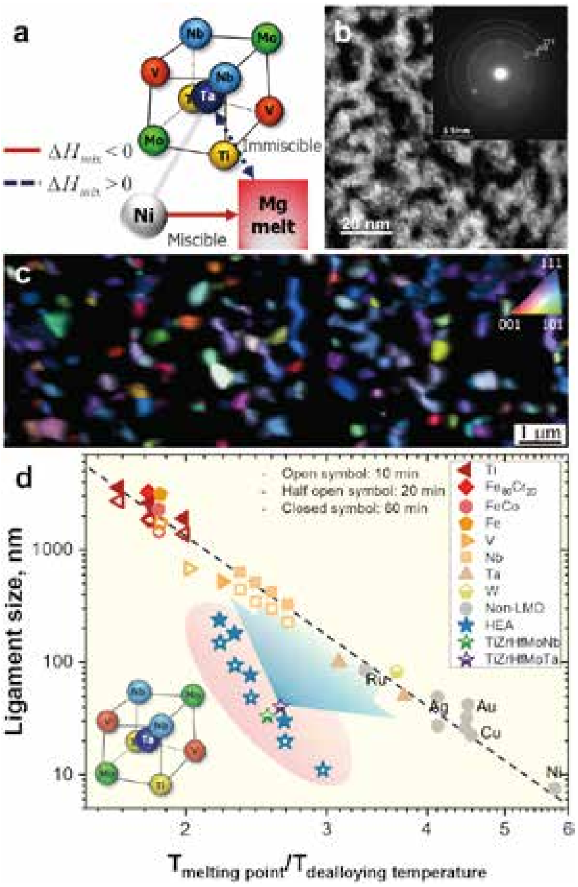

Fig. 1 (a) High-entropy design strategy for the 3DNP HEA by LMD. (b) Ligament structure after 10 min at 837 K. (c) Inverse pole figure map of the 3DNP HEA. (d) Ligament size versus homologous temperature.

Compared to pure metals or binary alloys, the 3DNP HEA showed a much slower coarsening rate and loss of desired 3DNP structure; the porous structure of the 3DNP HEA remains in the nanoscale regime after the same heat treatment (Fig. 1d). Suppressed coarsening in the 3DNP HEA likely originated from the high fraction of secure CSL boundaries and the slow diffusion in multi-principal elements. These findings provide an impetus toward a new generation of nanomaterials with excellent long-term performance.

References

[1] S.-H. Joo, J. W. Bae, W.-Y. Park, Y. Shimada, T. Wada, H. S. Kim, A. Takeuchi, T. J. Konno, H. Kato, and I. V. Okulov, Adv. Mater. **32**, 1906160 (2020).

Keywords: nanostructure, foam, 3D structure

Hidemi Kato (Non-Equilibrium Materials Research Laboratory)
E-mail: hikato@imr.tohoku.ac.jp
URL: http://www.nem2.imr.tohoku.ac.jp/index-e.html

Manganese-Based Intermetallic Compound Films with High Perpendicular Magnetic Anisotropy and Low Magnetization for Silicon Technology Application

Materials showing high perpendicular magnetic anisotropy, K_u, and low saturation magnetization, M_s, are essential for future spintronic devices. The (001)-textured Cu_2Sb-type manganese-based intermetallic compound films were fabricated onto silicon substrates with a thermally oxidized amorphous surface layer, and K_u was successfully enhanced by tuning the film composition.

Magnetic thin films with high perpendicular magnetic anisotropy, K_u, and low saturation magnetization, M_s, are desired for fabricating spintronic devices, such as magnetoresistive random access memory, MRAM. A high K_u and low M_s are important to ensure data retention with a small writing current and suppressing crosstalk among the memory cells with a diameter of several nanometers.

In this study, manganese (Mn)-based equiatomic intermetallic compounds, MnGaGe and MnAlGe, were selected as a class of high-K_u and low-M_s materials. The prototype of the crystal structure is Cu_2Sb (C38 phase), which is depicted in Fig. 1(a). We successfully fabricated epitaxially grown MnGaGe films onto MgO(100) substrates, and achieved a K_u value of 8.1×10^5 J/m^3 with a relatively small M_s of 2.6×10^5 A/m at room temperature (RT). The atomically resolved crystal structure was evident in the transmission electron microscopy image, which clearly showed the lattice spacing between the Ga/Ge layers (Fig. 1(b)) [1].

In addition to the magnetic properties, the Cu_2Sb-type Mn-intermetallic compounds possess another merit compared to other Mn-based materials, *i.e.,* the preferred (001) orientation for film growth, which is necessary for realizing perpendicular magnetization. The quantitative magnetic properties were unknown for poly-crystalline textured films before our study. Both MnGaGe and MnAlGe were investigated for the poly-crystalline film study, and (001)-textured films were successfully fabricated onto silicon substrates with an amorphous thermally oxidized layer on the surface. The maximum values of K_u were 8.6×10^5 J/m^3 and 4.8×10^5 J/m^3 for MnGaGe and MnAlGe [2] films, respectively, at RT, which are comparable with those in epitaxially grown films. Further study was conducted for the enhancement of moderate K_u of MnAlGe. By substituting Cr for a part of Mn, K_u was successfully enhanced to 7.3×10^5 J/m^3 [3], which approached the K_u of MnGaGe films as well as a target of 10^6 J/m^3 for future device applications.

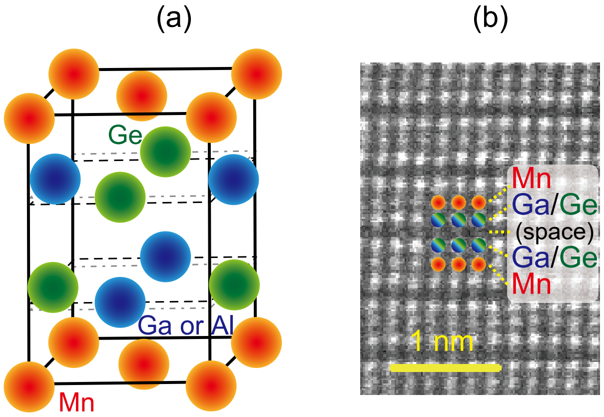

Fig. 1 (a) Schematic crystal structure of the Cu_2Sb-type MnGaGe or MnAlGe. (b) Cross-sectional transmission electron microscope image of a MnGaGe film, which demonstrates the lattice spacing between the Ga/Ge layers as well as the atomic positions.

The newly developed Cu_2Sb-type Mn-intermetallic compounds films are attractive for future spintronic applications as silicon-substrates-compatible high-K_u and low-M_s materials.

References

[1] M. Sun, T. Kubota, K. Ito, S. Takahashi, Y. Hirayama, Y. Sonobe, and K. Takanashi, Appl. Phys. Lett. **116**, 062402 (2020).

[2] T. Kubota, Y. Kota, K. Ito, R. Y. Umetsu, M. Sun, M. Mizuguchi, and K. Takanashi, AIP Adv. **10**, 015122 (2020).

[3] T. Kubota, Y. Kota, K. Ito, R. Y. Umetsu, M. Sun, M. Mizuguchi, and K. Takanashi, Appl. Phys. Express **12**, 103002 (2019).

Keywords: spintronics, magnetism

Koki Takanashi (Magnetic Materials Research Laboratory)
E-mail: koki@imr.tohoku.ac.jp
URL: http://magmatelab.imr.tohoku.ac.jp/

Novel Spin-Triplet Superconductivity and Huge Upper Critical Field at 35 T in UTe_2

We studied novel spin-triplet superconductivity in the heavy-fermion paramagnet UTe_2 in the proximity of ferromagnetic order. The superconducting transition temperature is 1.6 K. When the field is applied along the hard-magnetization axis (*b*-axis), the upper critical field, H_{c2}, reaches 35 T, which considerably exceeds the Pauli limit, indicating the spin-triplet state. The potential applications of UTe_2 and the relevant international collaboration/competition will further intensify in the future.

The novel heavy fermion superconductor UTe_2 attracts considerable attention [1,2], because of the realization of the spin-triplet state. UTe_2 is a paramagnet and crystallizes in an orthorhombic structure with the space group, *Immm*. The large Sommerfeld coefficient (~120 $mJK^{-2}mol^{-1}$) indicates heavy electronic states. The superconducting transition occurs at 1.6 K with a large specific heat jump, indicating strong coupling. When the field is applied along the hard-magnetization axis (*b*-axis), the field-reentrant superconductivity appears [3], as shown in Fig. 1(c). At 35 T, the superconductivity is cut off because of the first-order metamagnetic transition, where the effective mass of conduction electrons is enhanced, leading to strong fluctuations, which are an origin of the field-reentrant superconductivity. This behavior is similar to those of ferromagnetic superconductors. As shown in Fig. 1(a, b) the field-reentrant (-reinforced) superconductivity is observed in URhGe and UCoGe. In these cases, the collapse of the ferromagnetic Curie temperature induces ferromagnetic fluctuations, leading to the field-reentrant superconductivity. In contrast, in the paramagnet UTe_2, $T_{\chi\max}$, at which the magnetic susceptibility shows a broad maximum as a crossover, is transformed into the first metamagnetic transition at high fields.

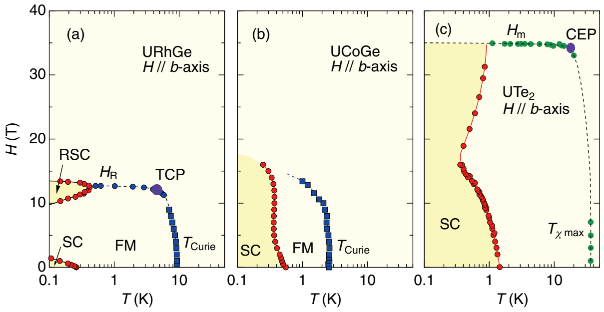

Fig. 1 Field-reentrant (-reinforced) superconductivity in the ferromagnets URhGe (a) and UCoGe (b) and in the paramagnet UTe_2 (c). SC, RSC, FM, TCP and CEP denote superconductivity, reentrant superconductivity, ferromagnetism, tricritical point and critical end point, respectively.

Another important discovery is the multiple superconducting states in UTe_2 [4]. Under a certain pressure, the superconducting transition splits into two, with a maximum of 3 K at 1 GPa for the higher transition temperature. At 1.5 GPa, the superconducting state collapses and a new magnetic ordered state is realized at a higher pressure. Under a magnetic field, the multiple superconducting states show a complicated pressure evolution, accompanied by an abrupt increase in H_{c2} in the high-field and low-temperature region. Different order parameters should be realized in the multiple superconducting states, supporting a scenario of the spin-triplet state. These studies are extended from the viewpoints of topological superconductivity and quantum computing. There were more than 20 papers on UTe_2 in 2019. Our paper was among the top 1% cited papers in the Web of Science in 2019 and was the Editors' Choice in JPSJ [1].

This work was conducted in collaboration with A. Nakamura, F. Honda, D. X. Li, Y. Homma, Y. Shimizu, Y. J. Sato, G. Knebel, J. P. Brison, A. Pourret, D. Braithwaite, G. Lapertot, Q. Niu, M. Valiska, H. Harima, W. Knafo, and J. Flouquet.

References

[1] D. Aoki, A. Nakamura, F. Honda, D. Li, Y. Homma, Y. Shimizu, Y. J. Sato, G. Knebel, J.-P. Brison, A. Pourret, D. Braithwaite, G. Lapertot, Q. Niu, M. Vališka, H. Harima, and J. Flouquet, J. Phys. Soc. Jpn. **88**, 043702 (2019).

[2] S. Ran, C. Eckberg, Q.-P. Ding, Y. Furukawa, T. Metz, S. R. Saha, I.-L. Liu, M. Zic, H. Kim, J. Paglione, and N. P. Butch, Science **365**, 684 (2019).

[3] G. Knebel, W. Knafo, A. Pourret, Q. Niu, M. Vališka, D. Braithwaite, G. Lapertot, J.-P. Brison, S. Mishra, I. Sheikin, G. Seyfarth, D. Aoki, and J. Flouquet, J. Phys. Soc. Jpn. **88**, 063707 (2019).

[4] D. Braithwaite, M. Vališka, G. Knebel, G. Lapertot, J.-P. Brison, A. Pourret, M. E. Zhitomirsky, J. Flouquet, F. Honda, and D. Aoki, Commun. Phys. **2**, 147 (2019).

Keywords: superconducting, heavy fermion, actinide

Dai Aoki (Actinide Materials Science Research Laboratory)
E-mail: aoki@imr.tohoku.ac.jp
URL: http://www.imr.tohoku.ac.jp/en/about/divisions-and-centers/research-division/25.html

Formation of Defects in Sintered Polycrystalline 122 Phase Fe-Based Superconductor

Among the factors influencing electromagnetic properties, grain boundaries are important microstructural issues for polycrystalline superconducting materials. In this study, based on the observed stacking faults and inter-granular amorphous layers, we have proposed a model for the formation of two types of cracks in the polycrystalline $Ba_2(Fe,Co)_2As_2$ (Ba-122) phase, namely, intra- and inter-granular cracks.

The evolution of intra- and inter-granular structures in Co-doped $BaFe_2As_2$ (Ba-122) has been studied to address the key issues associated with limited inter-granular current transport in randomly oriented polycrystalline Fe-based superconducting materials. In this study, the multi-scale structures in Ba-122 bulks fabricated at various sintering temperatures were investigated using electron microscopy, particularly focusing on the intra- and inter-grain structures [1].

Co-doped Ba-122 polycrystalline bulk samples were synthesized from elemental metals. Elemental Ba, Fe, Co, and As powders were weighed to a stoichiometric ratio of $Ba(Fe_{0.92}Co_{0.08})_2As_2$, and mixed and ground by high-energy ball milling.

Figure 1 shows the SEM back scattered electron (BSE) image of the polycrystalline bulk sintered at 600 °C for 48 h. The grains sintered at 600 °C were connected to each other through dark contrasted grain boundaries, as seen in the inset high angle annular dark field scanning transmission electron microscopy (HAADF-STEM) image. In the bulks sintered over 700 °C, the inter-granular phases expanded and separated the neighboring Ba-122 grains, while the cracks were generated into the Ba-122 grain parallel to each other.

Figure 2 summarizes the microstructural observations at a high magnification of the specimen sintered at 600 °C. The HAADF-STEM image (a) shows dark line contrasts in the intra-grain denoted with 'A' and the dark contrasted regions at grain boundaries denoted with 'B'. Note that there were no cracks in the intra-grain. The high magnification HAADF-STEM image (b) and high resolution TEM image (c) revealed that there were stacking faults of Fe-As layers on (001) planes in region 'A', and region 'B' was an amorphous layer with a width of 2 nm. Based on the observations, we propose that intra- and inter- granular cracks were formed by growing the stacking faults and amorphous layers, respectively.

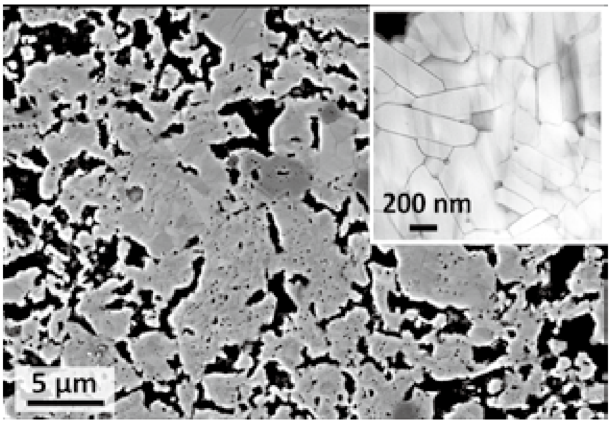

Fig. 1 SEM-BSE image of the samples heated at 600 °C for 48 h. The insets are HAADF-STEM images.

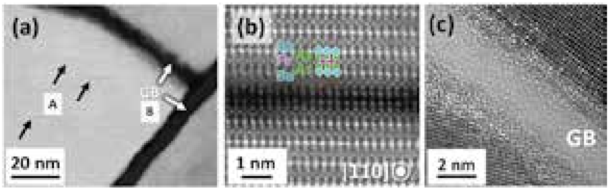

Fig. 2 (a) HAADF-STEM image of the sample heated at 600 °C for 48 h. (b) Magnified HAADF-STEM image of the dark area distributed in the intra-grain as shown by 'A' in (a). (c) High resolution TEM image of the grain boundary indicated by 'B' in (a).

References

[1] Y. Shimada, A. Yamamoto, Y. Hayashi, K. Kishio, J. Shimoyama, S. Hata, and T. J. Konno, Supercond. Sci. Technol. **32**, 084003 (2019).

Keywords: electron microscopy, nanostructure, superconducting

Yusuke Shimada (Materials Science of Non-Stoichiometric Compounds Research Laboratory)
E-mail: yshimada@imr.tohoku.ac.jp
URL: http://www.imr.tohoku.ac.jp/en/about/divisions-and-centers/research-division/26.html

Promoting Rare-Earth Monopnictides as a New Class of Magnetic Topological Insulator by Thin Film Stabilization

Using molecular beam epitaxy, GdBi thin films were fabricated as a candidate for antiferromagnetic topological insulators. Electrical transport and magnetic torque characterizations suggested lifting of semimetallicity below eight crystallographic unit cells and robust antiferromagnetism down to the minimum thickness of five crystallographic unit cells. These results are a promising step toward a bulk insulating antiferromagnetic topological insulator, which can potentially realize dissipationless spin-polarized currents on its edges in the monolayer limit.

Topological insulators (TIs) constitute a unique class of materials that are characterized by the presence of protected metallic surface states and a bandgap for the bulk part of the material. Combining TI with magnetism gives rise to exceptional properties such as dissipationless spin-polarized currents, which are promising ingredients for energy and electronic device applications. Magnetic TIs have been typically realized by magnetic doping and limiting the onset temperature at which magnetic effects on the electronic states of the TIs can be observed in the range of a few-kelvin.

Rare-earth monopnictides (*RX*) are a series of compounds with a variety of magnetic and electronic properties. Recent prediction of topological states in *RX* makes them a promising candidate for realizing magnetic TIs in intrinsically magnetic materials [1]. Their robust magnetism and strong coupling to electronic states can potentially boost the temperature necessary for the manifestation of properties unique to magnetic TIs. Despite these advantages, the semimetallic nature of *RX* inhibits experimental observations of their topological character, which is obscured by the metallic bulk state.

This study shows that the stabilization of antiferromagnetic GdBi (*R* = Gd, *X* = Bi) in thin film morphology can lift their semimetallicity while maintaining their long-range magnetic order [2]. High-quality GdBi (111) epitaxial thin films were fabricated with thickness ranging from 40 nm down to five crystallographic unit cells for the first time by molecular beam epitaxy. The temperature dependence of resistivity indicated a metallic-to-insulator transition in the thinnest films (see Fig. 1). Hall measurements suggested lifting of semimetallicity in these films by quantum confinement, supporting the metallic-to-insulator transition in GdBi thin films. Further, it was confirmed that the long-range antiferromagnetic order with T_N = 30 K was nearly unchanged from bulk single crystals in our thinnest films using torque magnetometry and transport measurements.

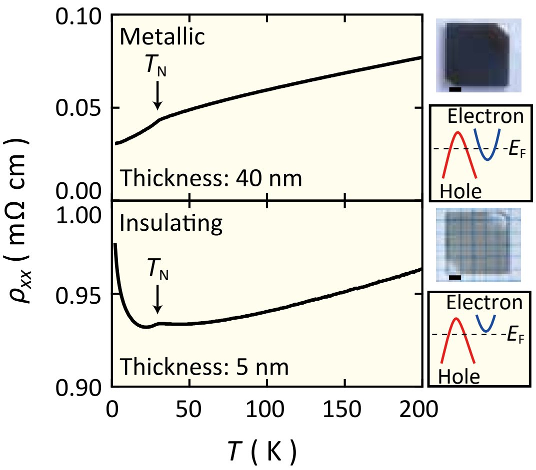

Fig. 1 Left panels show the temperature dependence of resistivity ρ_{xx} of GdBi thin films with two different film thicknesses. Right panels show the micrographs of samples and schematic drawings of the band structure of GdBi thin films. Scale bars are 1 mm.

The stabilization of GdBi thin films and ability to control their metallicity by film thickness present a pathway to observe the peculiar nature of magnetic TIs, including high-Chern-number-insulating states, which were predicted by first-principle calculations of monolayer GdBi [2].

References

[1] M. Zeng, C. Fang, G. Chang, Y.-A. Chen, T. Hsieh, A. Bansil, H. Lin, and L. Fu, arXiv:1504.03492 (2015).

[2] H. Inoue, M. Han, M. Hu, T. Suzuki, J. Liu, and J. G. Checkelsky, Phys. Rev. Mater. **3**, 101202(R) (2019)

Keywords: topological insulator, thin films, epitaxial growth

Hisashi Inoue (Exploratory Research Laboratory, IMR and Creative Interdisciplinary Research Division, Frontier Research Institute for Interdisciplinary Sciences)
E-mail: hisashi.inoue@fris.tohoku.ac.jp
URL: http://www.imr.tohoku.ac.jp/en/about/divisions-and-centers/research-division/33.html
https://www.fris.tohoku.ac.jp/en/researcher/creative/inouehisashi.html

Research Centers

Novel Production Method for the Lowest-Energy Nuclear State of Thorium-229 Isomer

International Research Center for Nuclear Materials Science

We have developed a novel production method for the lowest-energy state of the thorium-229 isomer (Th-229m). The method is based on nuclear resonant scattering (NRS) using a strong X-ray source at SPring-8. We successfully observed the NRS signal and demonstrated the first active pumping from the ground state of Th-229.

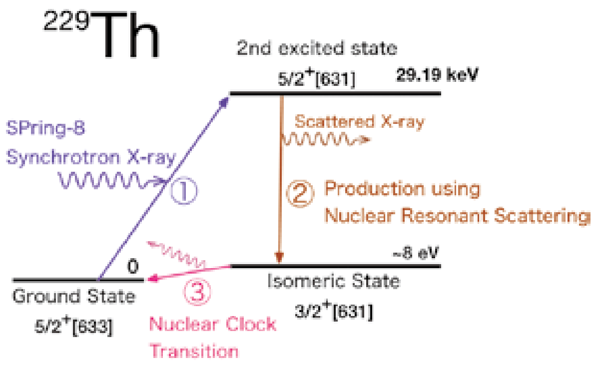

Fig. 1 Energy level of Th-229 (ground state and excited state) and new scheme for isomer production.

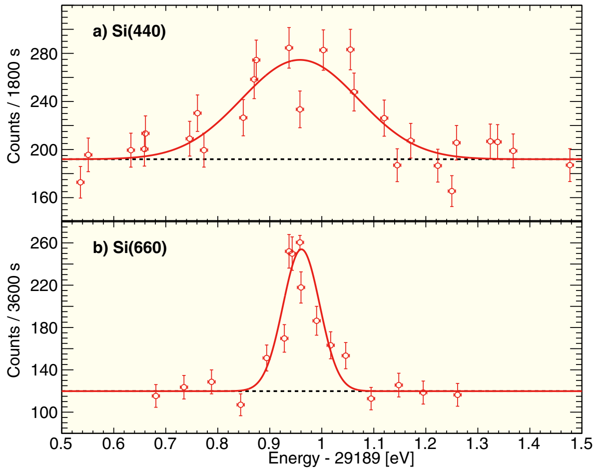

Fig. 2 Observed resonance peak of Th-229 NRS with (a) Si(440) beam (ΔE = 0.26 eV) and (b) Si(660) beam (ΔE = 0.1 eV) [1].

Thorium-229 (Th-229) is a unique nucleus having an ultra-low energy level of ~ 8 eV. This nuclear level (Th-229m) is so low that it can be excited optically by laser light, and thus, can be utilized as an ultra-precise “nuclear clock.” Despite numerous attempts for more than 40 years, direct laser excitation has not yet been achieved, and its basic properties still remain elusive. One of the bottlenecks in this direction is that Th-229m is produced only through the α decay of U-233, which is accompanied by a complicated nuclear process with a high level of radioactivity. We developed a novel method for producing Th-229m *via* the second excited state close to 29 keV by using X-ray beams (Fig. 1). The method is based on nuclear resonant scattering (NRS) using the strong synchrotron X-ray facility, SPring-8.

To observe the subtle NRS signal against the large background from X-ray electron scattering, we must enhance the signal rate by focusing the X-ray beam and correspondingly condensing the target material into a small area. We developed a Th-229 target with a small diameter of ϕ0.4 mm by the dry-up scheme. An ultra-pure sample of Th-229 provided by IRCNMS (Oarai) was used to build the target. The sample was chemically separated from U-233 a long time ago by Prof. Mitsugashira, and it is no longer contaminated with the radioactive Th-228 having a short half-life of 1.9 years.

Using the developed target, we performed the beam experiment at BL19LXU in SPring-8 2018. We successfully observed the NRS signal and determined the energy level of the second excited state of Th-229 (Fig. 2). Th-229m, predominantly decayed from the second excited state, can now be produced in a controllable manner. Efforts are underway to observe deexcitation photon emission from the isomeric state. This new method is expected to propel research on Th-229m toward the realization of a “nuclear clock.”

References

[1] T. Masuda *et al.*, Nature **573**, 238 (2019).

Keywords: actinide, nuclear materials, X-ray scattering

Koji Yoshimura and Akihiro Yoshimi (Corresponding Authors, Okayama University)
E-mail: yosimura@okayama-u.ac.jp, yoshimi@okayama-u.ac.jp
Yasuyoshi Nagai (Head of International Research Center for Nuclear Materials Science)
E-mail: nagai@imr.tohoku.ac.jp
URL: http://www.imr-oarai.jp/en/

Fabrication, Crystallization, and Properties of Fe-Based Soft Magnetic Alloys

Cooperative Research and Development Center for Advanced Materials

Researchers at the Cooperative Research and Development Center for Advanced Materials have studied various fabrication processes for advanced materials and explored the possibility of their application as multi-functional materials for future technologies in collaboration with universities and research institutes around the world. Herein, the recent research and development activities on soft magnetic material alloys for industrial applications are highlighted.

The effects of Co addition on the structural, thermal, and magnetic properties of Fe-Si-B-P-Cu alloy have been reported previously [1-2]. In this study, we explored the glass formation ability, thermal stability, and magnetic properties of the $Fe_{80}Co_xB_{14-x}Si_2P_3Cu_1$ (x = 0, 2, 4, 6) alloy and investigated the soft magnetic performances of $Fe_{80}Co_4B_{10}Si_2P_3Cu_1$ alloy. The addition of small amounts of Co remarkably affected the glass formation, crystallization, and magnetic behavior of the alloy. Co content was limited to 6% in consideration of fabrication costs. This nanocrystalline alloy presented a high magnetic induction (B_s) of 1.84 T, low coercivity (H_c) of 5.3 A/m (Fig. 1), high permeability of 12,601 at 1000 Hz, and low core loss of 62 W/kg at 1000 Hz at B_s of 1.5 T. These results indicated that the addition of a small amount of Co enhanced the soft magnetic performance by inducing uniform nanocrystallization of α-(Fe,Co) and averaging magnetic anisotropy.

It was also found that a high nucleation density could be obtained in the $Fe_{81.5}Si_{0.5}B_{4.5}P_{11}Cu_{0.5}C_2$ alloy by annealing it at a low heating rate because of the amounts of new nuclei precipitated during annealing [3]. The co-growth of pre-nuclei and newly precipitated nuclei by annealing at the optimum temperature (T_a) led to a uniform fine nanocrystalline structure of α-Fe, thereby resulting in low coercivity. The nanocrystallization mechanism of the alloy during annealing was different from that of the Fe-Si-B-P-Cu nanocrystalline alloy (Fig. 2). The $Fe_{81.5}Si_{0.5}B_{4.5}P_{11}Cu_{0.5}C_2$ alloy showed excellent magnetic softness. Thus, the developed strategy suggests that industrial crystallization can be simplified by a one-step annealing process at a low heating rate.

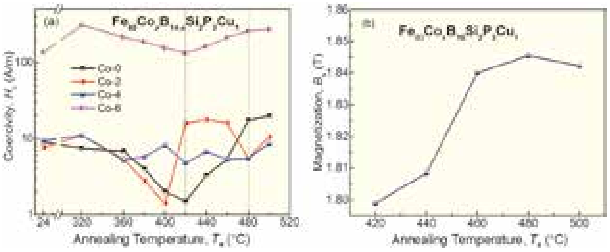

Fig. 1 (a) Dependence of H_c on T_a for the $Fe_{80}Si_2B_{14}P_3Cu_1$ alloy ribbons. (b) Dependence of B_s on T_a for the $Fe_{80}Co_4B_{10}Si_2P_3Cu_1$ alloy.

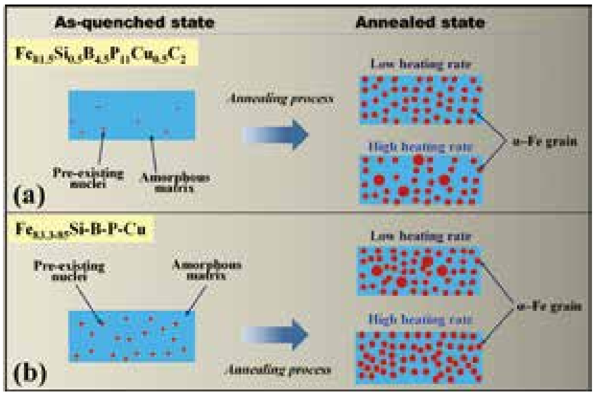

Fig. 2 Schematic illustration for the crystallization of (a) $Fe_{81.5}Si_{0.5}B_{4.5}P_{11}Cu_{0.5}C_2$ and (b) $Fe_{83.3-85}$Si-B-P-Cu alloys.

References

[1] B. Miao, Q. Luo, C. Chang, T. Liu, Y. Zhang, and J. Shen, J. Magn. Magn. Mater. **477**, 156 (2019).

[2] Y. Zhang, P. Sharma, and A. Makino, J. Alloys Compd. **709**, 663 (2017).

[3] L. Jiang, Y. Zhang, X. Tong, T. Suzuki, and A. Makino, J. Magn. Magn. Mater. **471**, 148 (2019).

Keywords: magnetic properties, nanostructure, amorphous

Yan Zhang (Cooperative Research and Development Center for Advanced Materials)
E-mail: zy-jp@imr.tohoku.ac.jp
Naoya Masahashi (Head of Cooperative Research and Development Center for Advanced Materials)
E-mail: masahasi@imr.tohoku.ac.jp
URL: http://www.crdam.imr.tohoku.ac.jp/en/index-en.html

Flux Pinning Properties of Practical $EuBa_2Cu_3O_y$ Tapes with Artificial Pinning Centers

High Field Laboratory for Superconducting Materials

Flux pinning properties of practical $REBa_2Cu_3O_y$ (REBCO, RE: rare earth and Y) tapes with $BaHfO_3$ artificial pinning centers (APCs) were studied. A good temperature scaling of the flux pinning force density F_p was found as a function of the magnetic field in a wide temperature region, in spite of the introduction of APC in REBCO tapes. It is suggested that the short and sprayed nanorods showed anisotropic random pinning behavior because of the high growth rate of REBCO layers.

It is well known that introducing artificial pinning centers (APCs) in practical $REBa_2Cu_3O_y$ (REBCO, RE: rare earth and Y) tapes can improve their in-field critical current density (J_c). Most APCs are $BaMO_3$ (M: Zr, Sn, Hf, *etc.*) with a nano-scaled rod structure along the *c*-axis of REBCO and they enhance the in-field J_c for *B*//*c* as a *c*-axis correlated pinning. We successfully developed homogeneous long EuBCO tapes with high in-field critical currents at low temperatures below 20 K *via* hot wall pulsed laser deposition at a high deposition rate, because of the introduction of APCs [1]. The flux pinning properties of the APC introduced EuBCO tapes were investigated in detail under high magnetic fields up to 24 T and in a wide temperature region using the 25 T cryogen-free superconducting magnet at HFLSM, as shown in Fig. 1(a). The flux pinning force (F_p) over 1 TN/m^3 was obtained at 4.2 K for *B*//*c*, which corresponds to ~66% of the world record of the REBCO short sample. In addition, good temperature scaling behavior of F_p was observed as a function of the magnetic field normalized by the F_p peak fields (Fig.1(b)), although the nanorods were introduced in the EuBCO matrix [2]. Generally, the F_p scaling behavior is observed for random pinning but not for the *c*-axis correlated pinning as in the case of well-aligned nanorods. The segmentation and incline of nanorods because of the very high growth rate of 20–30 nm/s is a possible reason for the random flux pinning-like behavior of F_p in Fig. 1(b). The solid lines in Fig. 1(a) are fitted results using the scaling law of F_p obtained in this study. Excellent agreement was observed between the fitting and experimental results and it was possible to easily estimate the J_c values at the desired conditions such as temperature, magnetic field, and field angle with the scaling function of F_p. This aspect is crucial for detailed designing of high field superconducting magnets.

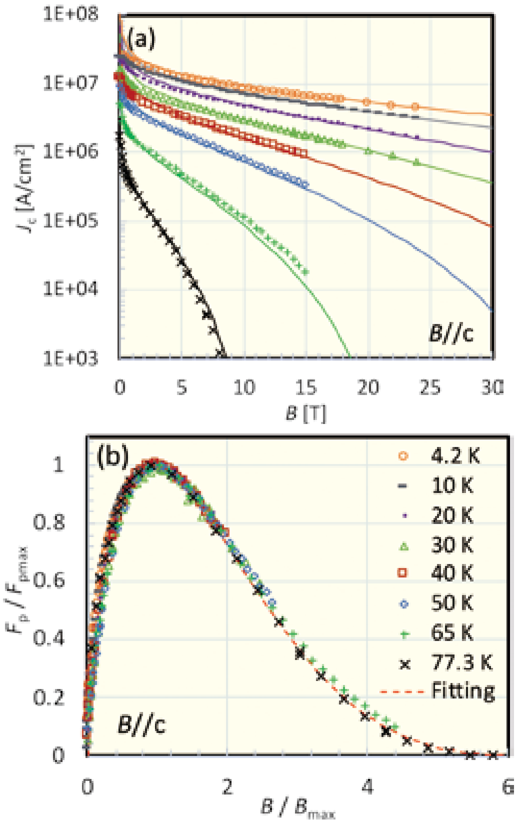

Fig. 1 (a) In-field critical current density J_c and (b) normalized pinning force densities as a function of normalized magnetic field for *B* // *c* for fast growth EuBCO with APC at various temperatures. Solid lines in (a) and broken line in (b) are fitted results using the scaling law.

References

[1] S. Fujita , S. Muto , W. Hirata, Y. Adachi, T. Yoshida , M. Igarashi, K. Kakimoto, Y. Iijima , K. Naoe, T. Kiss, T. Okada, and S. Awaji, IEEE Trans. Appl. Supercond. **28**, 6600604 (2018).

[2] S. Fujita, S. Muto, W. Hirata, T. Yoshida, K. Kakimoto, Y. Iijima, M. Daibo, T. Kiss, T. Okada, and S. Awaji, IEEE Trans. Appl. Supercond. **29**, 8001505 (2019).

Keywords: high magnetic field, high temperature superconductor

Shinji Fujita (Corresponding Author, Fujikura Ltd.)
E-mail: shinji.fujita@jp.fujikura.com
Hiroyuki Nojiri (Head of High Field Laboratory for Superconducting Materials)
E-mail: nojiri@imr.tohoku.ac.jp
URL: http://www.hflsm.imr.tohoku.ac.jp/cgi-bin/index-e.cgi

Scientific Breakthrough Toward the Creation of New Industrial Materials

Trans-Regional Corporation Center for Industrial Materials Research

The Institute for Materials Research (IMR) has launched the Trans-Reginal Corporation Center, a comprehensive Institute-wide effort that pairs the research groups at IMR across the innovation spectrum to solve industrial challenges of the present and address global energy problems for the future. The center was established in 2016 based on an agreement between the IMR, Osaka Prefecture Government, and enterprises sponsored by the government, taking over Osaka and Kansai Center projects.

The Trans-Regional Corporation Center was established in Osaka as a special unit of the Institute for Materials Research (IMR), Tohoku University, in April 2016 based on an agreement with the Osaka Prefecture Government. The Center is sponsored by the Ministry of Education, Culture, Sports, Science, and Technology, and takes over the Kansai Center, which carried out its duties from 2012 to 2016. The Center has three goals. First, to solve the technical problems that the industries have struggled to resolve. Second, the Center introduces academic output to the industries, with the aim of applying such output to society. Third, the Center helps educate the next generation of materials scientists and researchers. We have organized a bimonthly forum named “Monodukuri Kisokoza”, which focuses on special topics regarding materials and processing. Projects are conducted through wide collaborations between the government, universities, research institutions, and other organizations. The Center has four venues to cover the Kansai and Tohoku area, namely, the Osaka office at the Osaka Prefecture University, the Hyogo office at the University of Hyogo, the Sendai office at the IMR, and the Monozukuri Business Information Center Osaka at the Creation Core Higashi-Osaka.

The Center has developed various bioactive materials in collaboration with the industries, universities, and government [1]. Near-β TiNbSn alloy with low Young’s modulus was anodized in H_2SO_4 electrolytes to impart osseointegration to the alloy. The anodized oxide is composed of crystallized TiO_2 containing a number of internal pores and exhibits Hydroxyapatite (HA) formation after immersion in Hank’s solution. The anodized alloy after six weeks implantation in rabbit revealed incorporation of bone ingredients in the TiO_2 layer (Fig. 1). A model was proposed to explain the bioactivity of the anodized TiNbSn alloy (Fig. 2). It was concluded that the sulfuric acid electrolyte was favorable for HA formation, and the bioactivity could be attributed to the anodic TiO_2 that facilitated the incorporation of bone ingredients.

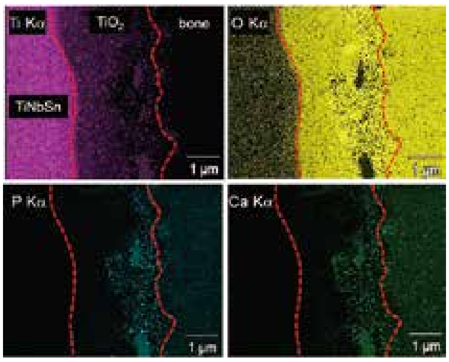

Fig. 1 TEM-EDX element mapping near the interface between anodic TiO_2 on TiNbSn alloy and rabbit bone six weeks after implantation: Ti Kα, O Kα, P Kα, Ca Kα.

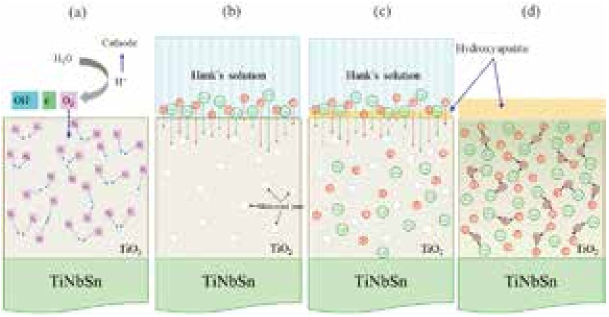

Fig. 2 Schematic diagrams of (a) micro-sized pore evolution during anodization, (b, c) bone ingredients migration, and (d) hydroxyapatite formation on the surface of the anodic oxide subject to immersion in Hank’ solution.

Similar collaborative research utilizing academic knowledge and industrial technology for practical applications is in progress. The Center will expend effort to be innovative in the metallic material industry through alliances with the partners and promote materials science research.

References

[1] N. Masahashi, Y. Mori, H. Tanaka, A. Kogure, H. Inoue, K. Ohmura, Y. Kodama, M. Nishijima, E. Itoi, and S. Hanada, Mater. Sci. Eng. C **98**, 753 (2019).

Keywords: biomaterial, osseointegration, photocatalytic

Naoya Masahashi (Head of Trans-Regional Corporation Center for Industrial Materials Research)
E-mail: masahasi@imr.tohoku.ac.jp
URL: http://www.imr.tohoku.ac.jp/en/about/divisions-and-centers/facilities/04.html

Development of an Ultra-Large Scale Micromagnetic Simulation Code for the Magnetic Process Inside Permanent Magnets Using a Supercomputer

Center for Computational Materials Science

Magnetization nucleation inside nanocrystalline magnetic materials was clarified in this study by ultra-large scale micromagnetic simulations. Initiation of magnetic reversal was affected by the microstructure of the nanocrystalline magnetic material, such as easy-axis orientation and overlap of grains. Development of the ultra-large scale micromagnetic simulation code enabled us to improve the performance of magnetic materials.

Micromagnetic simulations can clarify magnetization dynamics such as domain wall motions and magnetization reversals in magnetic materials. Such simulations provide not only magnetization but also distributions of the magnetic fields and magnetic energies. As actual magnetic materials have complex microstructures, visualization of their fields and energies yields important information to enhance their performance.

The simulation size of magnetic materials is determined by the exchange length and their microstructure. We had to employ a large number of grids inside the exchange length to simulate the magnetization dynamics accurately. Many magnetic materials consist of micro-meter sized grains [1]. In addition, the calculation method of the magnetic fields such as dipole and magnetostrictive fields has high computational complexity. Hence, we developed a micromagnetic simulation code for magnetization dynamics inside bulk magnetic materials using massively parallel computing [2, 3]. This code enabled us to perform ultra-large scale simulation of 0.3 billion cells on MASAMUNE-IMR.

Figure 1(a) shows an example of the simulation model for magnetic materials [4]. This model is for a hot-deformed permanent magnet that consists of tabular grains. The crystal axis was slightly tilted from the nominal easy-axis of the permanent magnet. We considered external, anisotropy, exchange, and dipole fields in this simulation. Figure 1(b) shows magnetic nucleation site at coercivity. The magnetization reversal initiated at a corner of the grain. Figures 1(c)–(e) show the distributions of the exchange, anisotropy, and dipole fields of remnant magnetization. In contrast with the anisotropy and exchange fields, the dipole field was not uniform inside the magnet. A strong dipole field was applied in the nucleation site.

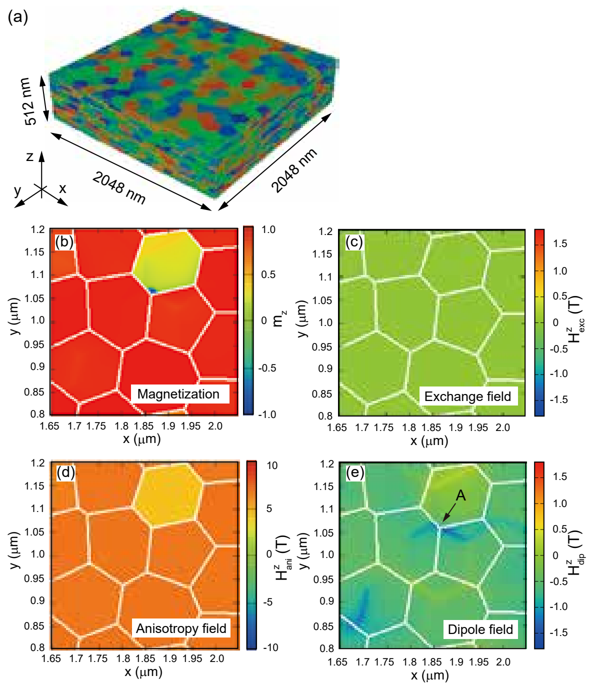

Fig. 1 (a) Image of the simulation model. (b) Nucleation site at coercivity. (c) Exchange, (d) anisotropy, and (e) dipole fields at remanence [3].

The nucleation is related to the orientation of the crystal axis because the distribution of this orientation is essential to the strong dipole field.

References

[1] R. K. Mishra and R. W. Lee, Appl. Phys. Lett. **48**, 733 (1986).

[2] H. Tsukahara, K. Iwano, C. Mitsumata, T. Ishikawa, and K. Ono, AIP Adv. **7**, 056224 (2017).

[3] H. Tsukahara, K. Iwano, C. Mitsumata, T. Ishikawa, and K. Ono, Phys. Rev. Appl. **11**, 014010 (2019).

[4] H. Tsukahara, K. Iwano, C. Mitsumata, T. Ishikawa, and K. Ono, NPG Asia Mater. **12**, 29 (2020).

Keywords: computational materials science, nanostructure, magnetism

Hiroshi Tsukahara and Kanta Ono (Corresponding Authors, High Energy Accelerator Research Organization)
E-mail: thiroshi@post.kek.jp
Momoji Kubo (Head of Center for Computational Materials Science)
E-mail: momoji@imr.tohoku.ac.jp
URL: https://www.sc.imr.tohoku.ac.jp/eng/

Ordering Kinetics of Nanoporous FeCo During Liquid Metal Dealloying and the Development of Nanofacets

Collaborative Research Center on Energy Materials

This study investigates the surface morphology and ordering kinetics of three-dimensional interconnected nanoporous FeCo. The ordering kinetics were accelerated by the surface-diffusion-driven coarsening in the nanoporous structure. Post-heat treatment led to the development of precise nanofacets via the preferential growth of surface planes.

It is interesting to study nanofacets because the surface structure has a significant effect on the physical properties of nanomaterials. However, it is still a challenge to synthesize well-defined nanofacets on a large-scale because of the tendency of nanomaterials to agglomerate.

In 2011, liquid metal dealloying (LMD) was reported and provided a means for overcoming the elemental limitation of chemical dealloying [1]. An example of a carefully designed LMD system is three-dimensional interconnected nanoporous (3DNP) FeCo. The order-disorder transition between the B2 and disordered *bcc* structures should result in structural variations. In the present study, the ordering behavior of 3DNP FeCo was investigated during the LMD process. The findings of ordering and coarsening phenomena were then practically applied for surface reconstruction.

The synthesized porous FeCo exhibited significant variations in surface morphology depending on the LMD temperature. At 600 °C, truncated cubic ligaments had flat surfaces of particular facets (Fig. 1a). The ligament surfaces become roughened at 700 °C (Fig. 1b). Stepped surfaces were observed at 800 °C (Fig. 1c), which is above the order-disorder transition temperature (T_c) of FeCo (730 °C).

In chemically ordered materials, the faceted surfaces depend on the degree of order, the energy of the facet(s), and surface-termination. Interestingly, the ordering kinetics of 3DNP structures differ from those of the bulk materials. When the dealloying time is increased from 3 min to 36 min at 600 °C, the ordered (100) peak is intensified, and the ordering parameter (S) increases drastically at the beginning of the LMD process (Fig. 2a). The bulk FeCo plate exhibited slower ordering kinetics than the nanoporous FeCo.

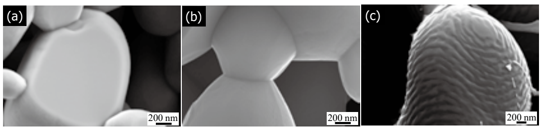

Fig. 1 Surface structures of porous FeCo prepared by LMD at (a) 600 °C, (b) 700 °C, and (c) 800 °C.

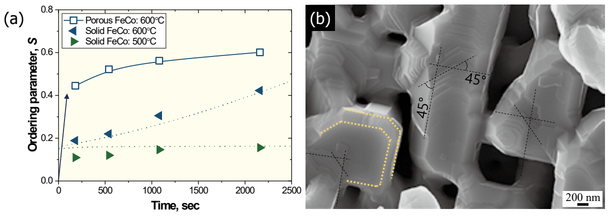

Fig. 2 (a) Ordering kinetics of porous FeCo and bulk FeCo samples. (b) Developed nanofacets on porous FeCo after post-heat treatment.

The theoretical ordering kinetics based on vacancy concentration agreed well with the experimental results of the bulk samples. However, there was a large disparity with the ordering kinetics of the 3DNP structure. The surface diffusivity was usually faster than the bulk diffusivity. In other words, the surface diffusion accelerated long-range ordering from the beginning of dealloying and formed a nanocube.

Precise nanofacets were developed on ligaments with equimolar composition in large-scale bulk-porous FeCo samples at 600 °C after heat treatment (Fig. 2b). The preferential growth of delicate steps and ledges verified the surface diffusion formation mechanism of the nanofacets [2].

References

[1] T. Wada, K. Yubuta, A. Inoue, and H. Kato, Mater. Lett. **65**, 1076 (2011).

[2] S.-H. Joo, K. Yubuta, and H. Kato, Scr. Mater. **177**, 38 (2020).

Keywords: nanostructure, foam, kinetics

Hidemi Kato (Corresponding Author, Non-Equilibrium Materials Research Laboratory)
E-mail: hikato@imr.tohoku.ac.jp
Tetsu Ichitsubo (Head of Collaborative Research Center on Energy Materials)
E-mail: tichi@imr.tohoku.ac.jp
URL: http://www.imr.tohoku.ac.jp/en/about/divisions-and-centers/facilities/05.html

Spin Transport in Different Oxide Phases of Copper

International Collaboration Center

In this study, spin transport in two types of copper oxides are directly compared. The results indicate that antiferromagnetic CuO exhibits good spin conductivity, whereas diamagnetic Cu_2O is a spin insulator. This implies that possessing unpaired spins should be an important characteristic for good spin conductors. It is also revealed that materials with different magnetic phases may have the potential to be spin operation materials.

Spin can be transported in an insulator even in the absence of motion of free electrons, implying that it is not affected by the Joule-heating problem. Electrical spin, rather than electrical charge, is expected to serve as the carrier of information and/or energy in next-generation information processing devices [1]. Therefore, one of the most important issues in the field of spintronics is to understand the mechanism and dominant characteristics of spin transports in insulating systems. Spin transport has been actively discussed in the context of various insulating systems [2-5]. However, the relationship between spin transport and the ambient material's intrinsic features, such as phase, structure, defect, and even its electronic configuration of ions has been rarely investigated.

In this study, the spin transports in two different oxide phases of the same transition metal copper have been directly compared. First, cupric oxide (CuO) and cuprous oxide (Cu_2O) were prepared, both of which are stable oxides of copper with distinct structures and magnetic properties. CuO is antiferromagnetic, in which Cu^{2+} has one unpaired spin in the 3*d* orbital, while Cu_2O is diamagnetic with a Cu^+ ion having a fully filled 3*d* orbital. By comparing the behavior of these two oxides, it is possible to obtain information about the influence of metallic ions with different electronic configurations on spin transport.

During the next step of the process, typical tri-layer devices were developed, which consisted of a thin CuO or Cu_2O layer sandwiched by a heavy metal Pt layer and an insulating Yttrium Iron Garnet (YIG) layer Fig. 1(a). Within this structure, the YIG layer acted as a spin generator, in which spin currents were generated and from which they were injected into the copper oxides via a spin pumping effect. The Pt layer acted as the spin detector, in which spin currents conducted through the middle oxide layer were detected as a voltage signal via the inverse spin Hall effect (ISHE). CuO and Cu_2O were identified based on X-ray diffraction measurements, as depicted in Fig. 1(b).

Figure 1(c) indicates that antiferromagnetic CuO is a good spin conductor. The ISHE signal of the YIG/CuO/Pt device was observed to be even greater than that of the device combining YIG and Pt directly. This implies that such an intervening antiferromagnetic layer enhanced the efficiency of spin transport at the interface. On the other hand, diamagnetic Cu_2O was observed to behave as a spin insulator. Spin currents were completely blocked by the 5 nm-thick Cu_2O layer.

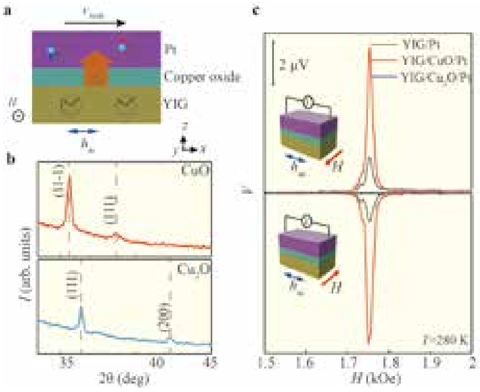

Fig. 1 Spin transport results in copper oxides

The difference between the degrees of spin transport in CuO and Cu_2O is mainly attributed to the difference in the electronic configurations of the respective copper ions, which is, in turn, associated to the different structures and magnetic phases of the oxides. In CuO, copper loses two electrons to form Cu^{2+}. There is an unpaired spin in the 3*d* orbital, which couples with the nearest neighboring unpaired spin in the opposite direction. Spins can be transported in such antiferromagnetic systems, as has been reported in several existing works [2-5]. In Cu_2O, Cu- possesses a fully filled 3*d* orbital without any unpaired spins. Cu_2O is diamagnetic, and its spin bandgap is equivalent to its electron bandgap. Therefore, diamagnetic materials act as spin insulators. This work experimentally establishes that the existence of unpaired spin is one of the important conditions for a good spin conductor.

References

[1] S. Maekawa, *Concept in Spin Electronics* (Oxford Univ. Press, 2016).

[2] Z. Qiu, J. Li, D. Hou, E. Arenholz, A. T. N'Diaye, A. Tan, K. Uchida, K. Sato, S. Okamoto, and Y. Tserkovnyak, Nat. Commun. **7**, 12670 (2016).

[3] Z. Qiu, D. Hou, J. Barker, K. Yamamoto, O. Gomonay, and E. Saitoh, Nat. Mater. **17**, 577 (2018).

[4] D. Hou, Z. Qiu, and E. Saitoh, NPG Asia Mater. **11**, 35 (2019).

[5] Z. Qiu and D. Hou, Chinese Phys. B **28**, 088504 (2019).

Keywords: spintronics, spin wave, spin transfer

Zhiyong Qiu (Corresponding Author, Dalian University of Technology)
E-mail: qiuzy@dlut.edu.cn
Gerrit Ernst-Wilhelm Bauer (Head of International Collaboration Center)
E-mail: icc-imr@imr.tohoku.ac.jp
URL: http://www.icc-imr.imr.tohoku.ac.jp/

Collaborative Research Programs of CNSAM

Center of Neutron Science for Advanced Materials

The Center of Neutron Science for Advanced Materials is a neutron facility with research emphasis on novel material science in IMR. It manages three neutron instruments in a research reactor facility, JRR-3, under a general user program, in addition to a new spectrometer, POLANO, at J-PARC/MLF. We leveraged these instruments and our endogenous capacity to commence a user program in April 2019. In this report, we present the current status of this research program.

The Center of Neutron Science for Advanced Materials (CNSAM) was established in 2010 to promote novel material science research that exploits the use of neutrons. CNSAM operates two neutron spectrometers and one diffractometer at the JRR-3 research reactor of the Japan Atomic Energy Agency. In addition, the center is in the process of constructing a polarized neutron spectrometer, POLANO, at the Materials and Life Science Experimental Facility (MLF) in the Japan Proton Accelerator Research Complex (J-PARC). POLANO is a newly developed spectrometer that was designed to realize polarization analysis in higher energy regions, beyond the measurements that are facilitated using a conventional triple-axis spectrometer [1]. The construction of POLANO began in 2012 under collaboration with the High Energy Accelerator Research Organization. After several years of designing, manufacturing, installing devices, and other related matters, we finally commenced beam commissioning in June 2017 and initiated a general user program in April 2019 at J-PARC MLF that exploit unpolarized neutron beams.

Additionally, we initiated a collaborative research program in IMR in last April to provide opportunities not only for experimental research using neutron beams, but also for the development of neutron devices and analysis methods, and theoretical work based on our neutron data. During FY 2019, we received 12 and 7 proposals from domestic and overseas researchers, respectively. The proposals were classified into several categories including “neutron experiment at MLF,” “instrumental development,” “development in analysis method,” “structural analysis and data handling,” and “others”. For the category of “others,” proposals based on the complemental use of neutron and other quantum beams, such as X-rays and muon beams were deemed to be acceptable.

Figure 1 represents an image of the user support in the POLANO cabin and the development of a solenoid coil for polarized measurement. Four staff members of the center are primarily responsible for supporting the users at both IMR and MLF.

Fig. 1. Image of the user support in the POLANO cabin at MLF and researchers engaged in the development of a solenoid coil for polarized measurements.

Our strategic use of the four neutron instruments includes structural research for new materials and advanced research on magnetism using polarized neutrons to improve our understanding of fundamental concepts in materials science. We are now preparing for full-scale operation of POLANO using polarized neutrons and the re-operation of JRR-3, which is scheduled for the end of FY2020.

References

[1] T. Yokoo, N. Kaneko, Y. Ikeda, S. Itoh, M. Fujita, M. Ohkawara, T. Ino, and K. Hayashi, MLF Annual Report 2018 (2019).

Keywords: neutron diffraction, neutron scattering, instrumentation

Masaki Fujita (Head of Center of Neutron Science for Advanced Materials)
E-mail: nc-imr@imr.tohoku.ac.jp
URL: http://nc-imr.imr.tohoku.ac.jp/index-e.html

Development of an Ultrasound Measurement System Available in High Field and Low Temperature Regions and its Application to Multipole Physics

Laboratory of Low Temperature Materials Science

This study reports the successful measurement of changes in ultrasound velocities of CeTe, demonstrating the field-induced antiferroquadrupole orders with high accuracy at high fields of up to 28 T at 50 mK. This is achieved using a cryogen-free hybrid magnet and a dilution refrigerator with a plastic mixing chamber.

Multipole physics is currently one of the leading research topics in the field of magnetism. Due to the limited availability of experimental techniques to access multipole phenomena, progress in their methods of measurement is highly desired. In this context, ultrasounds are capable of modulating crystal electric fields via lattice strains and inducing quadrupole electric fields. Such fields couple with electric quadrupole moments on local electrons in magnetic ions, and the responses to this interaction appear as changes in the velocities v of ultrasounds. Multipoles of high rank do not couple with magnetic fields directly, and interactions among multipoles are usually much weaker than dipole-dipole interactions. Studies on multipole physics, therefore, require high field and low temperature conditions. Based on this perspective, ultrasound serves as one of the most optimal probes, as it can be generated by low electric power translated via conductors.

In this study, we succeeded in developing an ultrasonic measurement system available at fields of up to 28 T and at temperatures as low as 50 mK, using a cryogen-free hybrid magnet (CHM) and a dilution refrigerator (DR) with a plastic mixing chamber (MC). The CHM was composed of an outer 9T-superconducting magnet and an inner 19T-resistive magnet [1]. The plastic MC suppressed the eddy currents arising from the high-speed sweep induced by the resistive magnet and enabled measurements at 50 mK. Figure 1 depicts the DR set in the CHM. Figure 2 presents an example of the observation of the elastic constant C_{44} (proportional to v^2) at 50 mK in CeTe, which is a heavy fermion system exhibiting antiferroquadrupole (AFQ) orders. As illustrated in Fig. 2, CeTe (T_N=2 K) was observed to undergo successive transitions from antiferromagnetic phase I to an AFQ phase II at 0.7 T, and, eventually, into another AFQ phase IV at around 6.3 T. The vanishing field of phase IV was determined to be 18.5 T, which agrees well with the theoretical prediction [3]. We confirmed the quenching of the AFQ phase by the field in CeTe and experimentally identified the transition field at the low temperature limit for the first time. Oscillations in C_{44} above 20 T were observed to have originated from the acoustic de Haas-van Alphen effect in the field-induced ferromagnetic phase by heavy fermions.

Fig. 1 CHM and DR constructed for High Field Laboratory for Superconducting Materials.

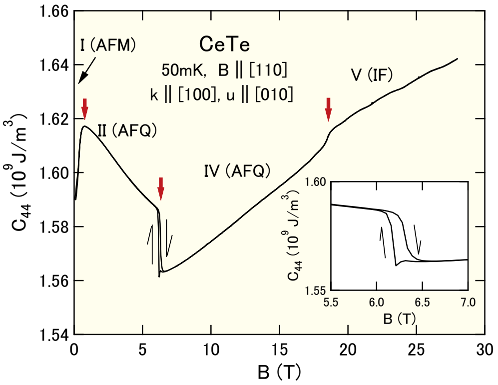

Fig. 2 Field dependence of the elastic constant C_{44} of CeTe at 50 mK (***B*** ll [110]) [2]. The letters ***k*** and ***u*** denote the wave vector and polarization of ultrasound, respectively.

References

[1] K. Watanabe, G. Nishijima, S. Awaji, K. Takahashi, K. Koyama, N. Kobayashi, M. Ishizuka, T. Itou, T. Tsurudome, and J. Sakuraba, IEEE Trans. Appl. Super. **16**, 934 (2006).

[2] S. Nakamura, S. Awaji, T. Yanagisawa, T. Saito, T. Matsumura, and A. Ochiai, JPS Conf. Proc. **30**, 011155 (2020).

[3] H. Takaguchi, Y. Hayashi, T. Matsumura, K. Umeo, M. Sera, and A. Ochiai, J. Phy. Soc. Jpn. **84**, 044708 (2015).

Keywords: high magnetic field, ultrasound, multipole

Shintaro Nakamura (Corresponding Author, Laboratory of Low Temperature Materials Science)
E-mail: nakamura@imr.tohoku.ac.jp
Takahiko Sasaki (Head of Laboratory of Low Temperature Materials Science)
E-mail: takahiko@imr.tohoku.ac.jp
URL: http://ltsd.imr.tohoku.ac.jp/index-e.html

Research Facility for Physics and Chemistry of Radioactive and Nuclear Materials

Laboratory of Alpha-Ray Emitters

More than 170 species of radioisotopes and nuclear materials are available for study at the Laboratory of Alpha-ray Emitters. This laboratory is an established international center for the study of the physical and chemical properties of radioactive materials such as actinide compounds. Researchers from many of the leading universities and institutes all over Japan visit this facility every year to prepare a variety of materials and perform chemical and physical measurements.

The Laboratory of Alpha-ray Emitters provides a research environment for the study of 170 radionuclides and elements, especially alpha-ray emitters such as actinide. This lab functions as a source for the preparation of pure crystals of actinide compounds and supplies them to other universities for application to synchrotron orbit-radiation. In the past decade, actinium-225 (Ac-225), an actinide element, has been produced as part of an inter-university collaboration. The radiation-controlled area of this laboratory includes three chemistry rooms that are equipped with local exhaust ventilation systems to facilitate the handling of various kinds of material. Several spectrometers, including units for gamma rays and alpha rays, are available.

A recent achievement is the determination of the energy of an optical nuclear transition in Th-229 using alpha-ray emitters. The low-energy nuclear transition in Th-229 is in the optical region and thus provides unique opportunities for high-resolution laser spectroscopy of the atomic nuclei. A promising application is an optical nuclear clock: an atomic clock that references a nuclear transition. Extensive experimental efforts have been devoted to the accurate measurement of this nuclear transition energy. However, the reported energy value ranges from 3.5 eV to 8.28 eV, and further measurements based on different experimental techniques are necessary to improve our confidence in the transition energy.

By using a transition edge sensor (TES) microcalorimeter, we have determined the absolute energy of the 29.2-keV gamma rays emitted from U-233 [1] (Fig. 1). Combining this result with that for the case wherein the 29.2-keV nuclear state in Th-229 was resonantly excited using narrow-band synchrotron radiation [2], we determined the optical nuclear transition energy in Th-229 to be 8.30(92) eV [1]. This value agrees with the two latest values measured using different experimental techniques.

We have recently succeeded in improving the energy-resolution of our TES chip to achieve better accuracy. The enhanced energy resolution was observed to be 15 eV at 29 keV, an improvement by a factor of 2.5 compared to previous sensors. A series of measurement tests using this new sensor is in progress at the Laboratory of Alpha-ray Emitters.

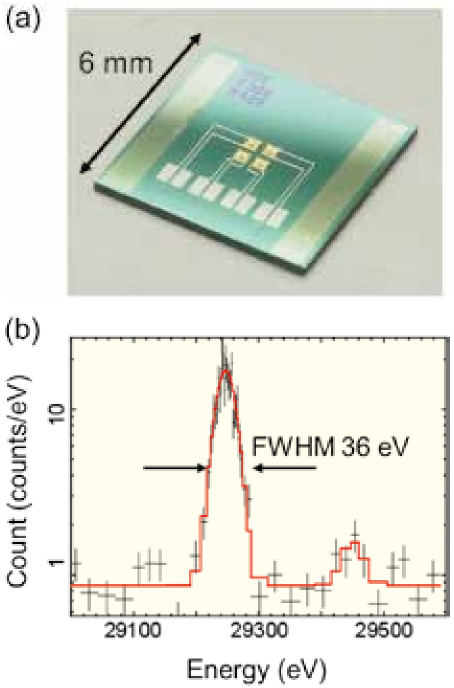

Fig. 1 (a) Developed TES microcalorimeter chip. (b) Spectrum of the 29-keV gamma ray emitted from U-233 was observed with an energy-resolution of 36 eV (FWHM), and used to determine the energy of the optical nuclear transition in Th-229.

References

[1] A. Yamaguchi, H. Muramatsu, T. Hayashi, N. Yuasa, K. Nakamura, M. Takimoto, H. Haba, K. Konashi, M. Watanabe, H. Kikunaga, K. Maehata, N.Y. Yamasaki, and K. Mitsuda, Phys. Rev. Lett. **123**, 222501 (2019).

[2] T. Masuda *et al.*, Nature **573**, 238 (2019).

Keywords: actinide, atomic clock, transition edge sensor

Kenji Shirasaki (Head of Laboratory of Alpha-Ray Emitters)
E-mail: kshira@imr.tohoku.ac.jp
URL: http://alpha.imr.tohoku.ac.jp/en.html

Microwave Digestion Using a Quaternary Acid Mixture for Inductively-Coupled Plasma Atomic Emission Spectrometric Analysis of Steel Samples

Analytical Research Core for Advanced Materials

We hereby introduce a microwave digestion method that is routinely used to prepare analytical samples. This digestion process is suitable for the quantification of volatile elements as well as alloyed elements in metallic samples. Reliable analytical results can be obtained by optimizing the digestion conditions.

Chemical analysis is an essential aspect in the characterization of advanced materials. To quantify alloyed elements in steel using an inductively-coupled plasma optical emission spectrometer (Fig. 1), the sample material is decomposed using different types of acid mixtures (*e.g.*, an acid mixture of hydrochloric and nitric acid (mixed acid A), acid mixture of sulfuric and phosphoric acid (mixed acid B), and acid mixture of hydrofluoric and nitric acid (mixed acid C)). For example, low-alloyed steel can be digested using mixed acid A, B, or C. However, mixed acid B is often used for several high-alloyed steels as well (*e.g.*, tool steel containing tungsten). However, silicon, phosphorous, and sulfur cannot be quantified using this mixed acid because it contains phosphorous and sulfur. Additionally, silicon precipitates in the acid solution.

For the preparation of steel samples, a quaternary acid mixture of hydrochloric, hydrofluoric, nitric, and phosphoric acids [1] was tested. A microwave oven (Fig. 2) was used for the digestion experiment. This quaternary acid mixture (HCl, HF, HNO_3, and H_3PO_4) was superior to the tertiary acid mixtures (HCl, HF, and HNO_3; HCl, HNO_3, and H_3PO_4; HCl, HF, and H_3PO_4; and HF, HNO_3, and H_3PO_4). The working parameters of the microwave digestion were optimized to quantify alloyed elements of vanadium, chromium, manganese, cobalt, nickel, molybdenum, and tungsten, in addition to a volatile element of sulfur in various steel samples including stainless steel and tool steel.

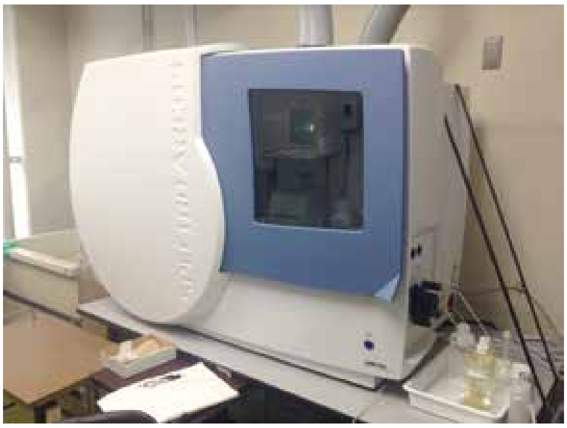

Fig. 1 Inductively-coupled plasma optical emission spectrometer model Arcos® MV130 (SPECTRO Analytical Instruments GmbH, Germany)

Fig. 2 Microwave oven model SpeedWave® MWS-3 used as the microwave pressure digestion unit (Berghof Products + Instruments GmbH, Germany)

References

[1] K. Nakayama and K. Wagatsuma, ISIJ Int. **60**, 193 (2020).

Keywords: atomic emission spectrometry, steel

Kenichi Nakayama (Corresponding Author, Analytical Research Core for Advanced Materials)
E-mail: ken1naka@imr.tohoku.ac.jp
Kazuaki Wagatsuma (Analytical Science Research Laboratory)
E-mail: wagatuma@imr.tohoku.ac.jp
Toyohiko J. Konno (Head of Analytical Research Core for Advanced Materials)
E-mail: tjkonno@imr.tohoku.ac.jp
URL: http://bunseki-core.imr.tohoku.ac.jp/top_eca_eng.html

International Collaborative Research

Electronic Materials

In Situ Observation of Crystal Growth and Re-Melting Process of $Si_{1-x}Ge_x$ Alloy Semiconductor

Rapid cooling of a liquid phase is a well-known method for obtaining materials with fine-grain structure. However, it was found that the grain sizes of the rapidly cooled and slowly cooled $Si_{1-x}Ge_x$ did not differ. We directly observed the solidification process of this material and found that the initially grown fine dendrites re-melted during the rapid cooling process, and finally formed a coarse-grain structure.

Rapid cooling of an alloy typically results in a polycrystalline material with a fine-grain structure because a large number of nucleation sites are formed instantaneously. Therefore, it is expected that a sample of rapidly cooled $Si_{1-x}Ge_x$ would have a fine-grain structure with relatively low variations of Ge composition and improved thermoelectric performance. However, such rapid crystallization experiments of the $Si_{1-x}Ge_x$ alloy have not been reported as yet.

Therefore, in the present study, we investigated the growth process of Si-rich $Si_{1-x}Ge_x$ ($x = 0.1$, 0.2, and 0.3) under rapid cooling to achieve the fine-grain structures for high thermoelectric performance [1]. The crystallized samples were analyzed by EDX and EBSD to study the compositional variation and grain structures.

$Si_{1-x}Ge_x$ samples were solidified under rapid (~330 K/min) and slow (1 K/min) cooling processes. Unexpectedly, the grain size and structures for both crystals were almost the same, even though the cooling rate in the rapid cooling experiment was more than 300 times faster than that in the slow cooling experiment.

To understand the formation of similar grain structures, the crystal growth process under rapid cooling was observed *in situ* using a high-speed microscopic camera with a recorder [1]. Figure 1 shows the snapshots recorded during the *in situ* observation of the crystal growth process of (a) $Si_{0.7}Ge_{0.3}$ and (b) pure Si at different temperatures during rapid cooling. Fine dendrites started to grow in $Si_{0.7}Ge_{0.3}$ after the heater was switched off. The dendrites grew rapidly for a short period but started to re-melt even as the temperature decreased. The re-melting was continued and ultimately completely. Finally, the recrystallization was observed as shown in the final picture of Fig. 1(a). In the case of pure Si (Fig. 1(b)), two dendrites grew under the observed area and the size of the dendrites increased with time without re-melting. From the *in situ* observations, it was obvious that the coarse-grain structure was formed in $Si_{1-x}Ge_x$ even during the rapid cooling process. The deviation from the equilibrium liquidus and solidus composition was relatively larger when the initial Ge composition was higher in $Si_{1-x}Ge_x$ and thereby the re-melting occurred immediately.

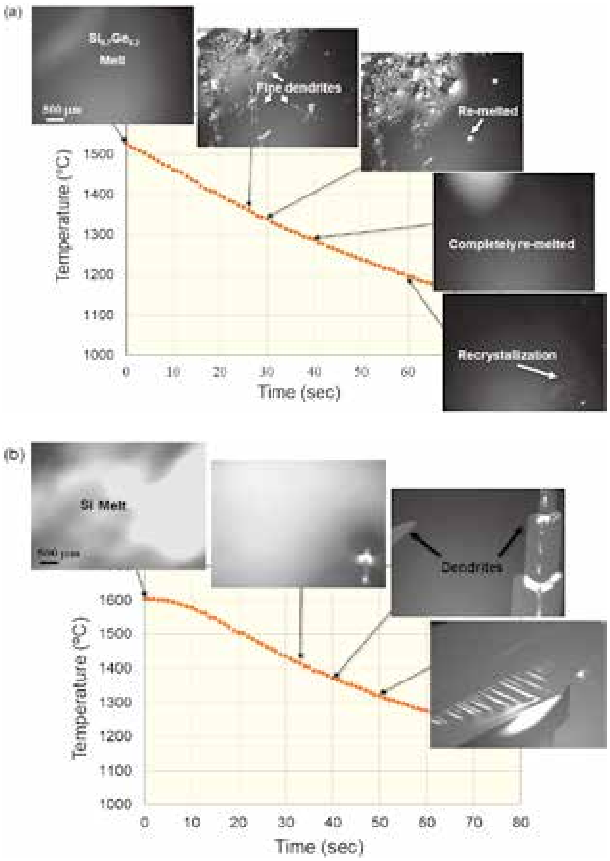

Fig. 1 Crystallization processes of (a) $Si_{0.7}Ge_{0.3}$ and (b) pure Si as a function of time during rapid cooling [1].

References

[1] M. Arrivanandhan, G. Takakura, D. Sidharth, K. Maeda, K. Shiga, H. Morito, and K. Fujiwara, J. Alloys Compd. **798**, 493 (2019).

Keywords: crystal growth, interface, crystal structure

Kozo Fujiwara (Crystal Physics Research Laboratory)
E-mail: kozo@imr.tohoku.ac.jp
URL: http://www.imr.tohoku.ac.jp/en/about/divisions-and-centers/research-division/02.html

Electronic Materials

Random Hopping of Majorana Fermion Found in Diluted α-$Ru_{0.8}Ir_{0.2}Cl_3$

In this study, we have investigated the thermodynamics of the well-known dilute dα-$Ru_{0.8}Ir_{0.2}Cl_3$-a model substance of Kitaev honeycomb lattice in which quantum spin liquids and fractional Majorana fermions are expected to appear. The observation of low-power behavior of heat capacity has been explained as a consequence of random hopping of Majorana fermions.

The investigation of spin liquids has been a long standing research topic in condensed matter physics. Exotic properties are expected in spin liquids in which no-magnetic orders appear despite substantial correlation. One of the most important predictions in this context is the fractionalization of the quantum number and the appearance of Majorana Fermion state in Kitaev honeycomb lattice systems [1], which is a unique system with an exactly solvable ground state.

α-$RuCl_3$ has been extensively investigated as the model substance of the Kitaev model, in which $4d^5$-Ru^{3+} ions form strongly anisotropic spin-arrays on the honeycomb lattice. Several physical properties demonstrate evidence of spin liquid-like excitations at high temperatures above the magnetic order at around 7 K. Its phase transition to zig-zag antiferromagnetic state prevents the investigation of its spin liquid ground state with lesser thermal disturbances. One strategy to accomplish this is a dilution with non-magnetic Ir^{3+} ions to suppress the magnetic order. In fact, the original zig-zag magnetic order disappears by about 10% Ir substitution and another magnetic order appears and persists at up to 20% substitution. In the present study, we have examined certain thermodynamic properties, such as magnetization, susceptibility, and specific heat, to examine the thermodynamic properties of the material at the quantum critical regime between the ordered and the disordered states.

The experiments have been conducted using a micro-calorimeter installed in a superconducting magnet generating magnetic fields of up to 16 T [2]. The specific type of the calorimeter is crucial to minimize the stress on the sample, which is very sensitive to pressure. The temperature dependence of heat capacity of the sample demonstrates the vast difference between its behavior and that of the non-substituted sample. Specifically, the clear peak of the zig-zag magnetic order was observed to disappear and a sizable residual entropy was detected at the ultra-low temperature regime. At above 2.5 K, the *C/T* was observed to be nearly constant, exhibiting slight decrement towards higher temperatures. A rapid decrease in the value of *C/T* was observed corresponding to lower temperatures with a clear power-law dependence.

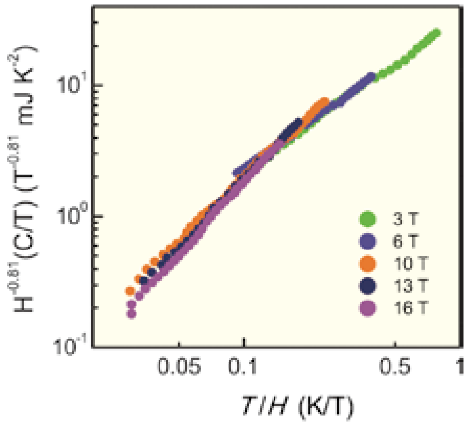

Fig. 1 Scaling relation of heat capacity in α-$Ru_{0.8}Ir_{0.2}Cl_3$ at various magnetic fields. The relation, $H^{0.81}C/T$-T/H, is found.

To elucidate the origin of the power-law dependence, we have tried to use different types of scaling functions. One of the most successful ones has been depicted in Fig. 1, for which the relation $H^{0.81}C/T$-T/H could be applied. The reduction in the value of *C/T* from *T*-linear behavior found during the Raman scattering demonstrates the hierarchy of the spin excitations. Specifically, the natures of the excitations vary over higher energy and lower energy regimes.

Such reduction is expected in the bond-disorder Kitaev model. Therefore, we inferred that the observed thermodynamic properties were induced by the quantum spin liquid with bond disorder. In terms of Fermions, this can be related to the random hopping of the Majorana Fermion in the pinned random flux background, which appears at the quantum critical regime due to the suppression of magnetic orderings.

References

[1] A. KItaev, Ann. Phys. (Berl.) **321**, 2 (2006).

[2] S. H. Do, C.H. Lee, T. Kihara, Y.S. Choi, S. Yoon, K. Kim, H. Cheong, W. T. Chen, F. Chou, H. Nojiri, and K. Y. Choi, Phys. Rev. Lett. **124**, 047204 (2020).

Keywords: high magnetic field, spin liquid, heat capacity

Hiroyuki Nojiri (Magnetism Research Laboratory)
E-mail: nojiri@imr.tohoku.ac.jp
URL: http://www.hfpm.imr.tohoku.ac.jp/index.html

Energy-related Materials

Prediction of Macroscopic Mechanical Properties of Diamond-Like Carbon from Atomic-Scale Simulation

Understanding the relation between the atomic-scale structure and mechanical properties of diamond-like carbon (DLC) is necessary and helpful for its improvement. Herein, we proposed a parameter to predict the mechanical properties of DLC by molecular dynamics simulation.

The amorphous carbon material called diamond-like carbon (DLC), mainly containing sp^3- and sp^2-hybridized carbon and hydrogen atoms, shows tremendous potential in various fields and applications because of its excellent mechanical properties. Generally, the mechanical properties of materials are determined by the atomic-scale structure. However, the detailed relation between the atomic-scale structure and the mechanical properties of DLC is still unclear. In this study, molecular dynamics (MD) approach was used to clarify the correlation between the atomic-scale structure and the macroscale Young's modulus of DLC.

To investigate the relation between the atomic-scale structure and the Young's modulus of DLC, tensile MD simulations were conducted on DLC with various atomic-scale structures.

First, we examined the coordination number (CN), which is known to be related to mechanical properties, as a parameter to predict the Young's modulus of DLC. The CN is given as follows:

$$\mathrm{CN} = \frac{2N(\mathrm{sp}) + 3N(\mathrm{sp}^2) + 4N(\mathrm{sp}^3)}{N(\mathrm{sp}) + N(\mathrm{sp}^2) + N(\mathrm{sp}^3)}, \quad (1)$$

where $N(\mathrm{sp})$, $N(\mathrm{sp}^2)$, and $N(\mathrm{sp}^3)$ are the numbers of sp-, sp^2- and sp^3-hybridized carbon atoms, respectively. However, we found that the Young's modulus (E) and density (ρ) of DLC do not show a monotonic correlation with CN (Fig. 1(a) and (b)), and thus CN fails as a parameter to predict the Young's modulus of DLC.

We considered that the failure of CN might be attributed to the treatment of the hydrogen atoms. In the case of hydrogenated DLC, hydrogen atoms do not participate in constructing the carbon network. Therefore, we examined effective coordination number ($\mathrm{CN_{eff}}$) as a parameter, that indicated the average coordination number of carbon atoms without the contributions from hydrogen atoms (N(H)).

$$\mathrm{CN_{eff}} = \frac{2N(\mathrm{sp}) + 3N(\mathrm{sp}^2) + 4N(\mathrm{sp}^3) - N(H)}{N(\mathrm{sp}) + N(\mathrm{sp}^2) + N(\mathrm{sp}^3)}, \quad (2)$$

The relation between $\mathrm{CN_{eff}}$, ρ, and E is shown in Figure 1(c) and (d). It was observed that $\mathrm{CN_{eff}}$ was linearly proportional to ρ, $\mathrm{CN_{eff}} = 0.87\rho + 1$. The monotonic positive correlation between $\mathrm{CN_{eff}}$ and E was also observed, $E = 180(\mathrm{CN_{eff}} - 2.0)^{1.5}$. Thus, $\mathrm{CN_{eff}}$ should be used rather than CN to predict the Young's modulus of DLC.

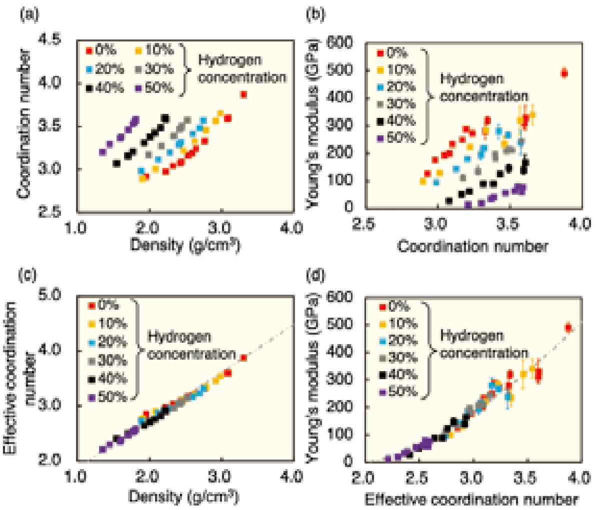

Fig. 1 (a) Relation between CN and density, (b) Young's modulus and CN, (c) $\mathrm{CN_{eff}}$ and density, and (d) Young's modulus and $\mathrm{CN_{eff}}$.

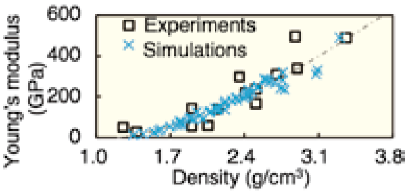

Fig. 2 Relation between the density and Young's modulus.

Finally, the applicability of the above obtained correlation between ρ and $\mathrm{CN_{eff}}$ was verified by comparison with the existing experimental results (Fig. 2). The simulation and experimental results showed the same monotonically increasing correlation between the Young's modulus, verifying that our obtained correlations among density, $\mathrm{CN_{eff}}$, and Young's modulus were correct [1].

References

[1] J. Xu, Y. Wang, Y. Cen, B. Xing, X. Zheng, Y. Ootani, and M. Kubo, J. Phys. Chem. C **123**, 24609 (2019).

Keywords: amorphous, mechanical properties, computational materials science

Momoji Kubo (Materials Design by Computer Simulation Research Laboratory)
E-mail: momoji@imr.tohoku.ac.jp
URL: http://www.simulation.imr.tohoku.ac.jp/eng/index.html

Infrastructural Materials

Two Types of Precipitates in High-Entropy Alloy FeCoNiCrTi$_{0.2}$ Analyzed by Atom Probe Tomography

A precipitation-strengthened high-entropy alloy, FeCoNiCrTi$_{0.2}$, was analyzed by atom probe tomography. Two types of precipitates, nano-sized spherical precipitates within grains and lamellar precipitates near grain boundaries, were observed. Atom probe analysis revealed that although the morphology of the precipitates in the inner grains was different from the one near the grain boundaries, the chemical partitioning in these two regions was almost the same.

High-entropy alloys (HEAs), a new class of structural materials, have attracted considerable attention in recent years because of their excellent properties and potential industrial applications. The face-centered cubic (FCC) HEAs are one of the most extensively investigated type of HEAs because they exhibit outstanding ductility, exceptional toughness, as well as excellent corrosion resistance. However, the FCC HEAs are not very strong, which limits their applications. The most promising method to strengthen FCC HEAs involves introducing hard precipitates into the FCC matrix.

Atom probe tomography (APT) is used to obtain three-dimensional atom maps of materials with nearly atomic-scale resolution [1-3]. This technique has high mass resolving power to identify isotopes, and therefore may be used to characterize the composition of different kinds of precipitates in HEAs, which include various elements [4].

Figure 1 shows the atom maps in the inner region of a grain in the precipitate-strengthened FeCoNiCrTi$_{0.2}$. The nano-sized spherical precipitates in the grain were clearly observed using APT. The average radius of these precipitates was 4.1 ± 1.6 nm. Figure 2 shows the atom maps near the grain boundaries, which clearly showed lamellar precipitates. It was found that Fe and Cr were almost depleted from the lamellar precipitates. APT analysis revealed that although the morphology of the precipitates near the grain boundaries was different from the one in the inner grains, the chemical partitioning in these two regions was almost the same. Besides, nano-sized spherical precipitates formed from the homogeneous nucleation within the grains, the lamellar precipitates were also formed because of the heterogeneous nucleation near grain boundaries. These precipitates contributed to the strength enhancing of FCC HEAs.

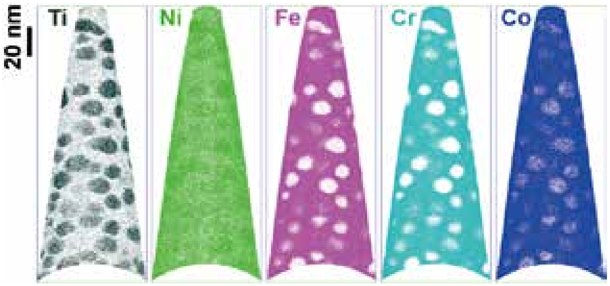

Fig. 1 Atom maps inside the grain with spherical precipitates.

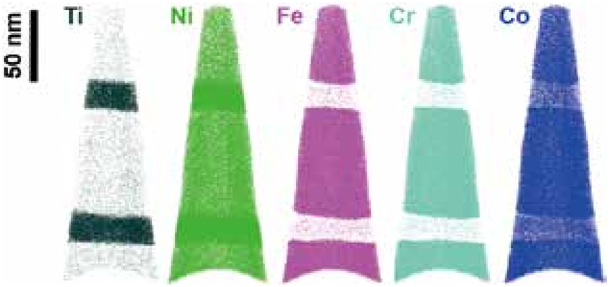

Fig. 2 Atom maps near the grain boundary with lamellar-shape precipitates.

References

[1] M. Tane, H. Nishiyama, A. Umeda, N. L. Okamoto, K. Inoue, M. Luckabauer, Y. Nagai, T. Sekino, T. Nakano, and T. Ichitsubo, Phys. Rev. Mater. **3**, 043604 (2019).

[2] Y. Ono, Y. Funakawa, K. Okuda, K. Seto, N. Ebisawa, K. Inoue, and Y. Nagai, Tetsu To Hagane **105**, 452 (2019).

[3] E. Tsuchiya, Y. Matsumura, Y. Hosoya, Y. Miyamoto, T. Kobayashi, K. Seto, K. Tomura, K. Inoue, and Y. Nagai, Tetsu To Hagane **105**, 76 (2019).

[4] Y. Tong, D. Chen, B. Han, J. Wang, R. Feng, T. Yang, C. Zhao, Y. L. Zhao, W. Guo, Y. Shimizu, C. T. Liu, P. K. Liaw, K. Inoue, Y. Nagai, A. Hu, and J. J. Kai, Acta Mater. **165**, 228 (2019).

Keywords: atom probe tomography, high entropy alloy, microstructure

Yasuo Shimizu, Koji Inoue, and Yasuyoshi Nagai (Irradiation Effects in Nuclear and Their Related Materials Research Laboratory)
E-mail: nagai@imr.tohoku.ac.jp
URL: http://www.imr.tohoku.ac.jp/en/about/divisions-and-centers/research-division/11.html

Electronic Materials

Water Vapor Sensitive Spin-State Switching in an Iron (III) Complex with Nucleobase Pendants Making Flexible Hydrogen-Bonded Networks

Sensitive chemo-switchable magnetic materials that can operate at room temperature are potential candidates for use in novel chemical devices. Here, we report a discrete iron (III) complex that exhibits high-spin/low-spin switching and is sensitive to water vapor above room temperature. The transformation of the hydrogen-bonded network triggered by water is closely associated with spin-state changing.

Porous magnetic materials with properties controllable by chemical stimuli (such as guest molecules) have potential applications in chemical switches. We focused on a structure-flexible hydrogen-bonded framework with multiple hydrogen bonding sites from nucleobase moieties attached to a discrete iron (III) spin-crossover (SCO) core, $[\mathrm{Fe^{III}(Tsal_2trien)}]\mathrm{ClO_4{\cdot}H_2O}$ (**1-$\mathrm{H_2O}$**) [1]. Here, we report low-spin/high-spin (LS/HS) state switching using water adsorption/desorption above room temperature (RT) between the solvated compound **1-$\mathrm{H_2O}$** and its solvent-free compound **1**.

When lattice water was removed from **1-$\mathrm{H_2O}$** to obtain **1**, the color of the solid changed from dark blue to dark red, corresponding to the LS and HS states of the $\mathrm{Fe^{III}}$ ion, respectively (Fig. 1a). When **1** was exposed to the atmosphere, the color quickly changed to dark blue, indicating the recovery of the **1-$\mathrm{H_2O}$** phase, as shown in the powder X-ray diffraction (PXRD) pattern (Fig. 1a). The spin-state assignment and its reversibility were also confirmed by the Mössbauer spectra (Fig. 1b).

In the χT-T plots of **1-$\mathrm{H_2O}$** under heating and a reduced pressure (10 Torr), χT abruptly increased at 323 K (Fig. 2a), indicating that the spin state changed from LS (**1-$\mathrm{H_2O}$**) to HS (**1**) by removing the water. In the cooling process, the value of χT remained constant (Fig. 2a), indicating that **1** remained in the HS state. Meanwhile, in the χT-T plots under atmospheric pressure (760 Torr), the transition temperature (T_c) increased to 343 K (Fig. 2b). Thus, it is clear that T_c is pressure dependent. The plot of γ_{HS} vs. time at 330 K shows that as soon as water was introduced, γ_{HS} abruptly decreased, and the electronic state completely switched from HS to LS within 30 s (Fig. 2c). The reversible switching of the spin state could be tuned by reducing the pressure and adding saturated water vapor at 340 K (Fig. 2d). This means that the bidirectional spin-state switching above RT can be controlled with only water vapor.

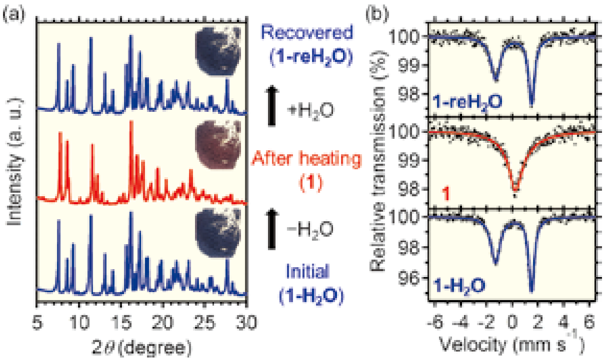

Fig. 1 Structure and spin-state changes during water elimination/adsorption. (a) PXRD patterns at RT and images of micro-crystals. (b) Mössbauer spectra at RT.

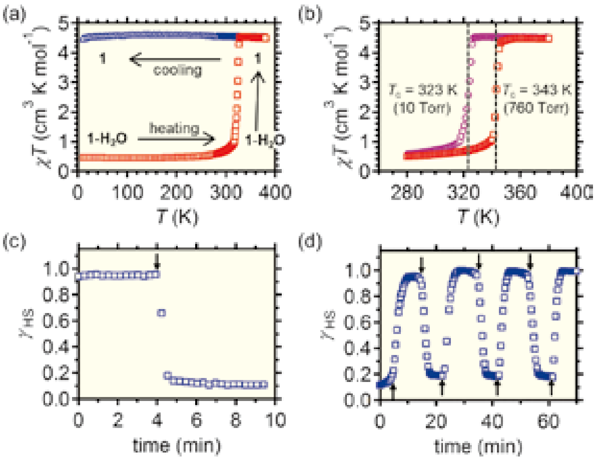

Fig. 2 (a) χT − T plots under 10 Torr of pressure of humidity. (b) Humidity dependence of χT − T plots. (c) Time dependence of HS fraction (γ_{HS}) at 330 K, where water vapor (760 Torr) was introduced to **1** after 4 min. (d) Variation of γ_{HS} at 340 K by repeating introducing water vapor (760 Torr) and reducing pressure (10 Torr). H = 2 kOe.

References

[1] K. Kagesawa, Y. Ichikawa, H. Iguchi, B. K. Breedlove, Z. Li, M. Yamashita, A. Okazawa, W. Kosaka, and H. Miyasaka, Chem. Lett. **49**, 1221 (2019).

Keywords: crystal structure, magnetic properties, porosity

Wataru Kosaka and Hitoshi Miyasaka (Solid-State Metal-Complex Chemistry Research Laboratory)
E-mail: w-kosaka@imr.tohoku.ac.jp; miyasaka@imr.tohoku.ac.jp
URL: http://www.miyasaka-lab.imr.tohoku.ac.jp/cn5/HOME-Eng.html

Electronic Materials

Non-Destructive Imaging for the Improvement of Fabrication Yields of Magnetic Tunnel Junctions

We have developed a new non-destructive imaging technique for a buried interface. In this technique, the penetration depth of the incident electrons and the corresponding depth of the generated backscattered electrons were controlled precisely. Therefore, this technique is highly useful as a quality assurance tool for nanoelectronic devices.

Current nanoelectronic devices typically use over thirty layers, where each interface needs to be optimized to maintain their smoothness without any contaminations and defects. To date, such interfacial structures have been evaluated by cross-sectional transmission electron microscopy (TEM) imaging with atomic resolution. However, TEM imaging requires a device to be sliced into approximately 100 nm thick pieces with electron transparency, which does not allow observing correlations between the interfacial structures and their transport properties. In this study, we have developed a new imaging method with a controlled electron-beam in scanning electron microscopy (SEM) that enabled us to observe buried interfaces in a non-destructive manner [1].

A magnetic tunnel junction (MTJ), consisting of Cr (80)/Pd (5)/$Co_2Fe_{0.4}Mn_{0.6}Si$ (5)/MgO (2)/$Co_{0.5}Fe_{0.5}$ (5)/IrMn3 (10)/Ru (7) (thickness in nm), was deposited onto an MgO(001) substrate using ultrahigh vacuum sputtering][2]. This structure was then etched into a series of MTJ pillars with dimensions between 10×10 and 50×50 μm^2 by photolithography and Ar-ion milling. The milled regions were filled with Al–O and finally a top electrode of Au (80 nm) was sputtered. The fabricated MTJs were measured using a four-terminal method, categorizing into large (>80%) and small (<20%) tunneling magneto-resistance (TMR) ratios.

Electron flight simulations [3] was used to estimate the representative electron acceleration for SEM imaging. By taking over 5% changes in the number of backscattered electrons, two voltages were selected to highlight any defects at the MgO interfaces. SEM images taken at 10.5 keV exhibited some redeposited materials at the edges of the low TMR device only, as shown in Figs. 1(a) and (d). Further energy dispersive X-ray spectroscopy (EDX) mapping confirmed the redeposition of aluminum carbides, which were likely formed by the reaction between the residual resist from photolithography and Al during Al-O sputtering [see Figs. 1(b), (c), (e), and (f)].

Accordingly, the Al-O sputtering power was reduced, which increased the yield to 15%. This demonstrated that our non-destructive imaging technique is useful to identify production faults and improve the yield [4].

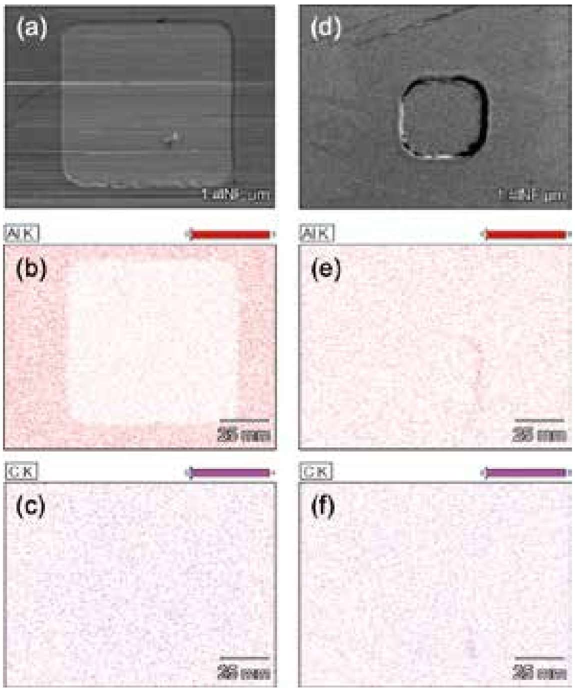

Fig. 1 (a) and (d) Scanning electron images of large and small TMR devices, respectively. EDX mapping is shown for (b) Al and (c) C for the large TMR device and for (e) Al and (f) C for the small TMR device. After Ref. [4].

This work was done in collaboration with Prof. Atsufumi Hirohata from University of York, UK.

References

[1] A. Hirohata, Y. Yamamoto, B. A. Murphy, and A. J. Vick, Nat. Commun. **7**, 12701 (2016).

[2] E. Jackson, M. Sun, T. Kubota, K. Takanashi, and A. Hirohata, Sci. Rep. **8**, 7585 (2018).

[3] P. Hovington, D. Drouin, R. Gauvin, D. C. Joy, and N. Evans, Scanning **19**, 29 (1997).

[4] E. Jackson, Y. Wu, W. Frost, J.-Y. Kim, M. Samiepour, K. Elphick, M. Sun, T. Kubota, K. Takanashi, T. Ichinose, S. Mizukami, and A. Hirohata, J. Phys. D: Appl. Phys. **53**, 014004 (2019).

Keywords: spintronics, interface, magnetic properties

Koki Takanashi (Magnetic Materials Research Laboratory)
E-mail: koki@imr.tohoku.ac.jp
URL: http://magmatelab.imr.tohoku.ac.jp/

Electronic Materials

Nonclassical Crystal Growth Dynamics Visualized Through Interfacial Potential Modification by Electrical Field of Optical Trapping Laser

Although the laser trapping of crystalline clusters in an aqueous solution can induce forced crystallization (even from an unsaturated solution), its crystal growth mechanism remains unclear. Herein, we revealed by direct *in-situ* observation on the crystal surface that crystal growth dynamics was triggered by the interfacial potential modification, which was caused by the electrical field of the incident laser.

The optical trapping of crystalline clusters with a laser tightly focused on the air/solution interface can induce forced crystallization, even on an unsaturated solution [1]. The laser trapping induced crystallization (LTIC) technique enables high controllability of crystallization, involving spatiotemporal control of nucleation, polymorph control depending on laser polarization, and switchable crystal growth, among others. However, the detailed crystal growth mechanism of LTIC remains unclear because the direct investigation on the crystal surface, where crystal growth actually progresses through molecular adsorption and desorption from an ambient phase, has not been carried out. Here, we performed an *in-situ* optical microscopic observation on the surface of an ionic crystal grown via LTIC to investigate the actual crystal growth mechanism.

A sodium chlorate metastable single crystal floating on the air/saturated solution interface was optically trapped with a laser tweezers system constructed by tightly focusing a continuous-wave laser (λ = 532 nm, 1 W) with an objective lens (60X, NA = 0.9) equipped on an inverted polarized-light microscope (Fig. 1A). The dynamics on the crystal surface was visualized using an optical microscope.

The irradiation of the trapping laser on the crystal triggered the wetting transition of the solution thin layer covering over the crystal surface. The solution thin layer changed from complete wetting state to partial wetting state by the laser irradiation. (Fig. 1B). The wetting transition suggests that the electrical field from the laser propagating though the crystal modified the interfacial potential by imposing an additional electrostatic potential. We found that the liquid droplets formed through the wetting transition, the size of which was hundreds of nm, fused into a crystal while keeping their volume until they reached the crystal step ledge through diffusion on the crystal terrace [2] (Fig. 1C and 1D). This growth process, through the collective incorporation of building molecules to form the crystal, deviates from the assumption of the classical crystal growth theory, in which crystal growth progresses through the sequential incorporation of each building unit. Our result not only provides a novel viewpoint that elucidates the mechanism of LTIC, but also is the first direct *in-situ* optical visualization of the nonclassical cluster assimilation crystal growth dynamics from diffusion to fusion of clusters [3].

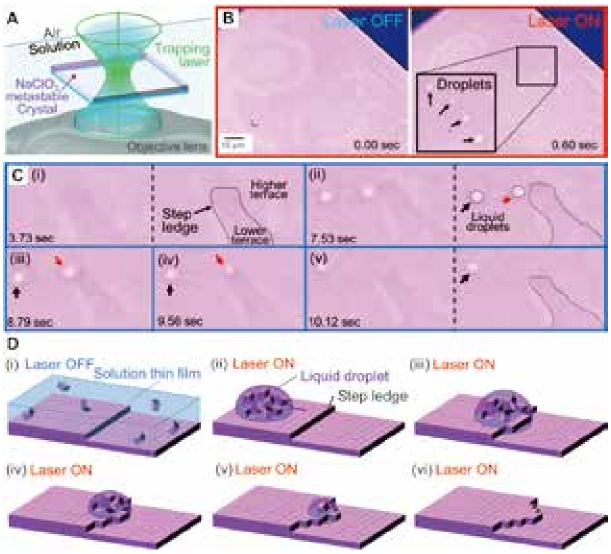

Fig. 1 (A) Experimental schematic. (B) Wetting transition of solution thin film. (C) Cluster assimilation like nonclassical crystal growth dynamics. (D) Fusion process of the liquid droplet illustrated by the Kossel crystal model.

References

[1] T. Sugiyama, K. Yuyama, and H. Masuhara, Acc. Chem. Res. **45**, 1946 (2012).

[2] T. Niinomi, T. Sugiyama, T. Ujihara, S. Guo, J. Nozawa, J. Okada, T. Omatsu, and S. Uda, Cryst. Growth Des. **19**, 4138 (2019).

[3] M. Sleutel and A. E. S. Van Driessche, Proc. Natl. Acad. Sci. U. S. A. **111**, E546 (2014).

Keywords: crystal growth, interface, thin films

Hiromasa Niinomi (Crystal Chemistry Research Laboratory)
E-mail: h.niinomi@imr.tohoku.ac.jp
URL: http://www.uda-lab.imr.tohoku.ac.jp/index-e.html

Catch Atoms in Action Using *In-Situ* Annealing TEM

International Research Center for Nuclear Materials Science

In-situ high-resolution TEM imaging is useful for understanding how thermal energy and partial pressure affect the crystal growth and surface atomic structures of metals, alloys, and compounds. Our *in-situ* annealing spherical aberration-corrected TEM/STEM is now ready for atomic-scale relaxations of platinum nanoparticles for a fuel-cell reactor or post-irradiation-annealing of nuclear reactor pressure vessel steels.

The international Japan-UK collaboration achieved direct atomic-scale visualization of surface structures during a chemical reaction in the fuel-cell reactor. The partial-pressure dependence of the surface atomic structure of platinum nanoparticles (NPs) on amorphous carbon films was studied in reactive gas atmospheres under both the e-beam and controlled heating conditions.

Spherical aberration-corrected TEM images indicated that the Pt atoms on the topmost surface layer formed a hexagonal lattice without the adsorbed atoms. Few individual Pt atoms were observed on the carbon film in 10^{-2} Pa H_2 and N_2 atmospheres (Fig. 1(a)). Such faceted Pt NPs with distinct edges are a key feature for clarifying the stabilizing effect of reducing or non-reactive gas molecules. As expected, the Pt NPs in CO and O_2 atmospheres had an markedly round (less faceted) shape, as shown in Fig. 1(b). This is critical evidence that the gas molecules directly contributed to the stabilization of the surface structure.

The transformation of NPs into disordered clusters was systematically quantified under controlled *in-situ* annealing experiments at 423, 573, and 723 K using our specially designed *in-situ* annealing TEM [1]. The *in-situ* annealing TEM was then applied to various nuclear materials such as reactor pressure vessel (RPV) and oxide dispersion strengthened (ODS) steels for understanding their embrittlement mechanisms. Fig. 2 shows the WB-STEM images obtained from RPV steels before and after post-irradiation-annealing at 673 K. During annealing, two ½ <111> dislocation loops coalesced each other and formed a <100> dislocation loop. Such growth and lattice relaxation processes of the ½ <111> loops were consistent with the molecular dynamics at the atomic scale. This is the first direct visualization of relaxation processes of neutron-induced dislocation loops during post-irradiation annealing.

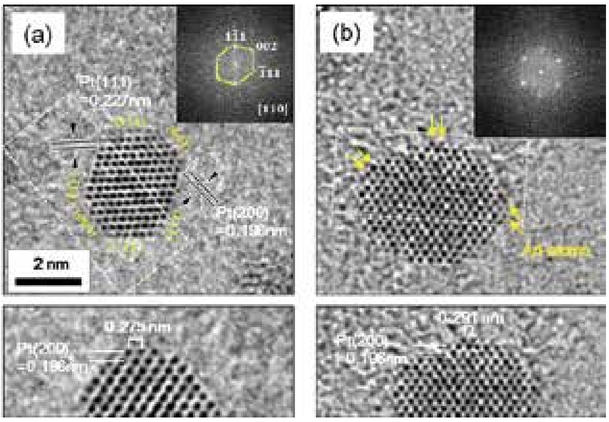

Fig. 1 SAC images of the Pt/C catalysts under H_2 atmosphere of 1×10^{-2} Pa (a), CO atmosphere of 1×10^{-2} Pa (b); the fast Fourier transform patterns are shown as insets. The reconstructed surfaces of Pt NPs are enlarged.

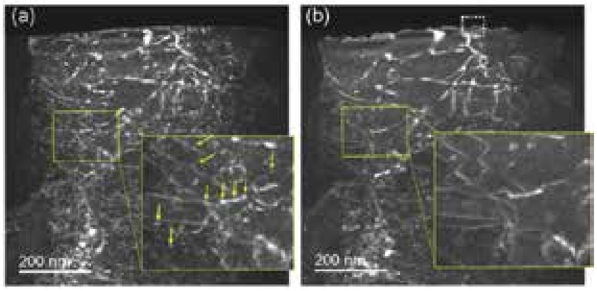

Fig. 2 Weak-beam STEM images of the neutron-irradiated reactor pressure vessel steel acquired at R.T. (a) and 400 °C under isothermal annealing (b). The arrows in (a) show the dislocations and dislocation-loops.

References

[1] K. Yoshida, X. Zhang, Y. Shimada, Y. Nagai, T. Hiroyama, N. Tanaka, L. Lari, M. R. Ward, E. D. Boyes, and P. L. Gai, Nanotech. **30**, 175701 (2019).

Keywords: electron microscopy, nanocluster, nuclear materials

Kenta Yoshida (Corresponding Author, International Research Center for Nuclear Materials Science)
E-mail: k_yoshida@imr.tohoku.ac.jp
Yasuyoshi Nagai (Head of International Research Center for Nuclear Materials Science)
E-mail: nagai@imr.tohoku.ac.jp
URL: http://www.imr-oarai.jp/en/

Structure and Magnetic Properties of Nanoporous FePt Fabricated by Dealloying Melt-Spun Fe-Pt-B Alloy

Cooperative Research and Development Center for Advanced Materials

Soft magnetic nanoporous fcc-FePt with an average pore size of 12 nm was fabricated by dealloying a melt-spun $Fe_{60}Pt_{20}B_{20}$ alloy in H_2SO_4 aqueous solution. The fcc-FePt transformed to $L1_0$-FePt by annealing the nanoporous alloy, which significantly increased the coercivity up to 8.42 kOe.

Ordered face-centered-tetragonal FePt ($L1_0$-FePt) has attracted considerable attention for the fabrication of high-performance permanent magnets and ultrahigh density magnetic data storage media owing to their extremely high magnetocrystalline anisotropy [1]. Although nanostructured $L1_0$-FePt alloys, including thin films, nanoparticles, and nanocomposites have been synthesized by various techniques and studied extensively, there have been only a few reports on the development of nanoporous structures [2]. Here, we report the magnetic properties of a nanoporous $L1_0$-FePt magnet, which was fabricated by dealloying [2] of a melt-spun $Fe_{60}Pt_{20}B_{20}$ alloy and subsequent annealing.

Pure Fe, Pt, and B were arc-melted to obtain an alloy ingot. Ribbon samples were prepared by melt-spinning. The alloy ribbons were dealloyed in 0.1 mol/L H_2SO_4 solution for 1800 s. Subsequently, annealing was carried out in vacuum at 803–943 K for 600 s. The structure of the samples was examined by XRD and TEM. SEM was used to observe the morphology and to measure the chemical composition. The magnetic properties of the samples were measured with a VSM at the CRDAM in IMR, Tohoku University.

A nanoporous alloy with an Fe/Pt atomic ratio of ~55.3/44.7 was fabricated by dealloying the $Fe_{60}Pt_{20}B_{20}$ alloy composed of nanoscale amorphous and fcc-FePt phase. The average ligament and pore sizes were ~27 nm and 12 nm, respectively (Fig. 1(a)). The TEM image (Fig. 1(b)) confirms the formation of a nanoporous architecture. The corresponding SAED pattern reveals the polycrystalline fcc-FePt diffraction rings without the amorphous phase. The nanoporous fcc-FePt alloy showed soft magnetic characteristics. A phase transformation from fcc-FePt to $L1_0$-FePt was realized in the nanoporous alloy after annealing (Fig. 2(a)). The VSM results showed that the coercivity of the nanoporous alloy increased from 0.14 kOe to 8.42 kOe with the increase in annealing temperature from 823 K to 943 K (Fig. 2(b)), which could be attributed to the increased volume fraction of the $L1_0$-FePt phase. The SEM observation revealed that the ligament size increased from 31 nm to 60 nm, whereas the average pore size remained nearly constant at ~16 nm with the increasing annealing temperature.

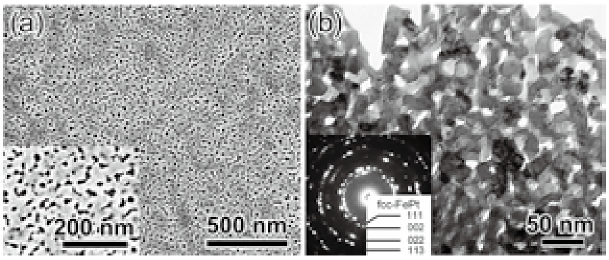

Fig. 1 SEM image (a) and bright-field TEM image of melt-spun $Fe_{60}Pt_{20}B_{20}$ alloy dealloyed in 0.1 mol/L H_2SO_4 solution. Inset in (b) is the corresponding SAED pattern [3].

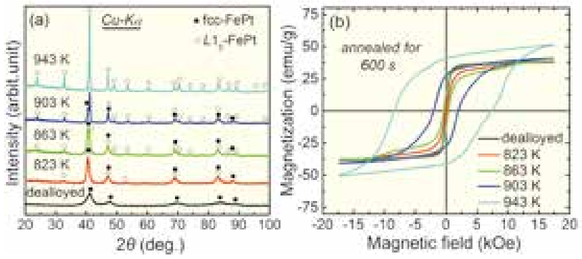

Fig. 2 XRD patterns (a) and hysteresis loops (b) of the nanoporous fcc-FePt alloys annealed at 823–943 K for 600 s [3].

References

[1] K. Watanabe and H. Masumoto, Trans. Jpn. Inst. Met. **24**, 627 (1983).

[2] J. Erlebacher and R. Seshadri, MRS Bull. **34**, 561 (2009).

[3] D. Ma, Y. Wang, Y. Li, R.Y. Umetsu, S. Ou, K. Yubuta, and W. Zhang, J. Mater. Sci. Tech. **36**, 128 (2020).

Keywords: nanoporous alloy, dealloying, magnetic properties

Wei Zhang (Dalian University of Technology)
E-mail: wzhang@dlut.edu.cn
Naoya Masahashi (Head of Cooperative Research and Development Center for Advanced Materials)
E-mail: masahasi@imr.tohoku.ac.jp
URL: http://www.crdam.imr.tohoku.ac.jp/en/index-en.html

Enhancement of the Critical Current Density in Cu/Ag Composite Sheathed (Ba, K)Fe_2As_2 Tapes by Pre-Annealing Process

High Field Laboratory for Superconducting Materials

Iron-based superconductors are promising candidates for high-field applications. Here, a pre-annealing method was used to promote the transport critical current density (J_c) in Cu/Ag composite sheathed (Ba,K)Fe_2As_2 tapes. It was found that such tapes showed a transport J_c up to 4.9×10^4A/cm^2 and 6.5×10^4A/cm^2 (4.2 K, 10 T) under ambient pressure and using a hot-press technique, respectively.

For 122-type iron-based superconductor (IBS) tapes produced by pure silver sheath, the transport critical current density (J_c) is 1.5×10^5 A/cm^2 (4.2 K, 10 T). To reduce the usage of pure silver in IBS tapes, a Cu/Ag composite sheath was tested. However, owing to the voids and residual cracks formed during cold deformation, the Cu/Ag composite sheathed IBS tapes had low J_c from being sintered at low temperatures. This suggests that high-temperature pre-annealing may be an effective method to enhance the transport current of the Cu/Ag composite (Ba,K)Fe_2As_2 (Ba-122) tapes [1].

For the tape prepared without any pre-annealing process (Tape 1), a transport J_c of ~2.0×10^4 A/ cm^2 (4.2 K, 10 T) was obtained, as shown in Fig. 1. However, by a high-temperature pre-annealing process and final ambient pressure sintering process, the J_c increased to 4.9×10^4 A/ cm^2 (4.2 K, 10 T, Tape 2). This result indicates that the transport J_c of the Cu/Ag composite sheathed Ba-122 tapes fabricated by the ambient pressure sintering process could be significantly improved by the high-temperature pre-annealing process. Moreover, the J_c of the pre-annealed tape could be further improved by a hot-press process.

When the tapes were sintered at a low sintering temperature, the grains were not well connected in the Cu/Ag composite sheathed IBS tapes. High-temperature pre-annealing process combined with cold rolling improved the grain alignment and enhanced the grain connections. As shown in Fig. 2, the Vickers hardness of the superconducting core in the pre-annealed tapes (Tape 2) reached an average value of 112.7, but the Vickers hardness of the non-pre-annealed sample (Tape 1) only had an average value of 77.6. The reason for the high hardness of Tape 2 is that there were more large grains and fewer cracks in the samples pre-annealed at a relatively high temperature (880 °C). The well-constructed crystallization and grain connectivity obtained in the pre-annealed tapes were considered as the major causes of the high J_c.

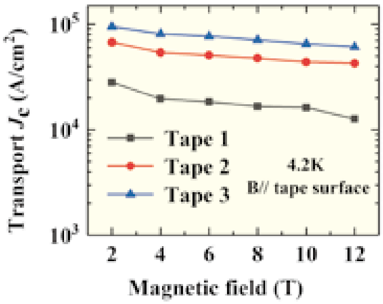

Fig. 1 Magnetic field dependence of transport J_c in different kinds of tapes [1].

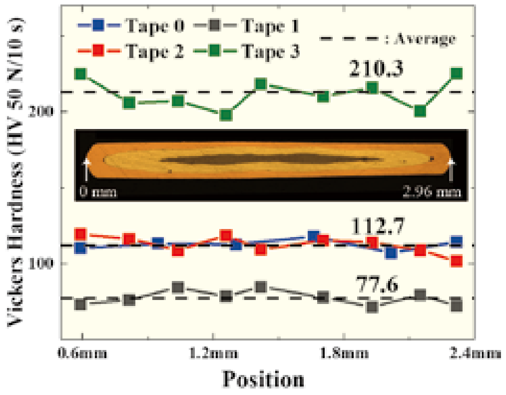

Fig. 2 Vickers hardness of superconducting core of four types of tapes [1].

References

[1] L. Li, X. Zhang, C. Yao, S. Liu, H. Huang, C. Dong, Z. Cheng, S. Awaji, and Y. Ma, Mater. Res. Express **6**, 096003 (2019).

Keywords: iron-based superconductor, high magnetic field, critical current density

Yanwei Ma (Corresponding Author, Institute of Electrical Engineering, Chinese Academy of Sciences)
E-mail: ywma@mail.iee.ac.cn
Hiroyuki Nojiri (Head of High Field Laboratory for Superconducting Materials)
E-mail: nojiri@imr.tohoku.ac.jp
URL: http://www.hflsm.imr.tohoku.ac.jp/cgi-bin/index-e.cgi

Negative Thermal Expansion and Negative Linear Compressibility of Black Phosphorene: A First-Principles Prediction

Center for Computational Materials Science

The Center for Computational Materials Science supports various advanced studies on computational materials science by providing users with an efficiently tuned high-performance computer as an international collaborative research institute. Here, we introduce an activity selected from ~200 users. Dr. Chen investigated the properties of black phosphorene.

While most materials expand on heating and contract on pressure, some abnormal negative response, such as the negative thermal expansion (NTE) and negative linear compressibility (NLC), exists in very few materials. For the first time, we have found using first-principles calculations that NTE and NLC can coexist in low-dimensional black phosphorene [1]. Black phosphorene is a graphene analog with a strongly puckered structure (Fig. 1). In the temperature-field, the volume-NTE in black phosphorene was observed below 170 K, and three axial-NTEs were observed in the whole studied temperature range, illustrating its anisotropic feature (Fig. 2(a)). In the hydrostatic pressure-field, the NLC behavior occurred along the zigzag or armchair direction in different pressure ranges (Fig. 2(b)) while the volume maintained positive compression. The lattice dynamics analysis revealed that the reentrant honeycomb network was formed from a very flexible hinge and a widely variable angle of the local structure unit in black phosphorene facilitated the NTE and NLC behaviors. The calculated phonon spectra and Gruneisen parameters in the Brillouin zone showed that the out-of-plane transverse acoustic phonon mode TA_Z corresponded to the negative modes of Gruneisen parameter. As the negative values of Gruneisen parameter implied an increase in the frequencies of the vibrational modes with increasing volume, this TA_Z phonon was likely conducive to the occurrence of abnormal physical properties in black phosphorene. This study recognized that black phosphorene is a promising 2D functional material with rich physics, and also provided some foundation and clues for exploring the abnormal properties in other 2D materials.

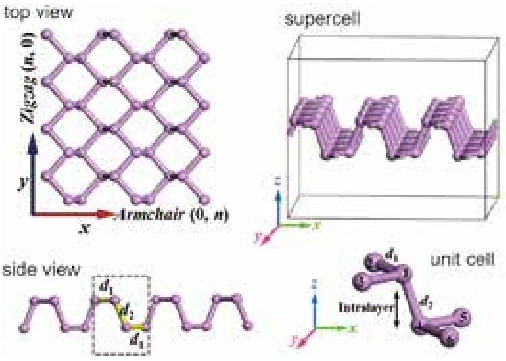

Fig. 1 Structure of black phosphorene with a strongly puckered feature and the supercell used in calculations. The resultant structural parameters agree well with the experimental values.

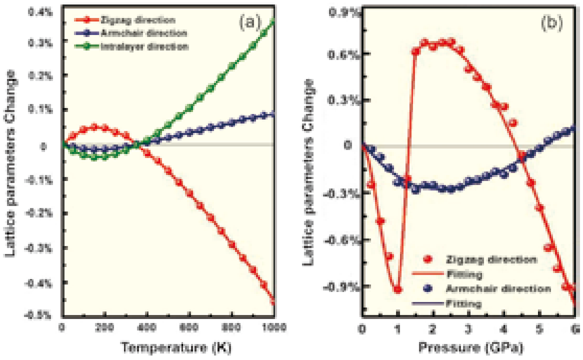

Fig. 2 Negative thermal expansion (NTE) and negative linear compressibility (NLC) in black phosphorene detected in the calculations.

(a) Temperature dependence of the structural parameters along three directions.

(b) Pressure dependence of the structural parameters along zigzag and armchair directions.

References

[1] L. Wang, C. Wang, and Y. Chen, J. Phys.: Condens. Matter **31**, 465003 (2019).

Keywords: 2D materials, unusual response properties, first-principles calculations

Ying Chen (Corresponding Author, School of Engineering, Tohoku University)
E-mail: ying@rift.mech.tohoku.ac.jp
Momoji Kubo (Head of Center for Computational Materials Science)
E-mail: momoji@imr.tohoku.ac.jp
URL: https://www.sc.imr.tohoku.ac.jp/eng/

Observation of Magnetic Excitation in a Quantum Spin System Using POLANO

Center of Neutron Science for Advanced Materials

The neutron spectrometer POLANO at J-PARC is a powerful instrument that can achieve polarization analysis in higher energy regions up to 100 meV to elucidate detailed spin and lattice dynamics. Using POLANO, we measured the spin excitations and phonons in the quantum spin system of CuGeO$_3$ and observed the thermal evolution of both dynamics.

The study of low-dimensional spin systems is important for understanding the fundamental natures of high-temperature superconductors [1]. CuGeO$_3$ is a typical one-dimensional material. The magnetism of the edge-sharing CuO$_2$ chains of CuGeO$_3$ can be described by the $S = 1/2$ Heisenberg model, and the two spinon continuum excitation, which are associated with the quantum nature of spins, were indeed observed by the neutron scattering measurement [2]. Below 14 K (T_{sp}), a spin gap opens due to the formation of a spin-singlet pair with the spontaneous lattice distortion. This behavior is recognized as the spin-Peierls transition, and CuGeO$_3$ was thought to be the first inorganic spin-Peierls compound. However, it remains unclear whether CuGeO$_3$ is an archetypal spin-Peierls system, because phonon softening accompanied by spin-Perierls transition has not yet been observed on CuGeO$_3$. To clarify the mechanism of the anomalous phase transition in CuGeO$_3$, the identification of the dynamical behaviors, meaning both spin fluctuations and phonons at and around the transition temperature (not in the ground state at a base temperature), is essential.

We performed inelastic neutron scattering experiments to elucidate the thermal evolution of the spin and lattice dynamics using the chopper spectrometer POLANO, which was recently supplied for a user program at MLF.

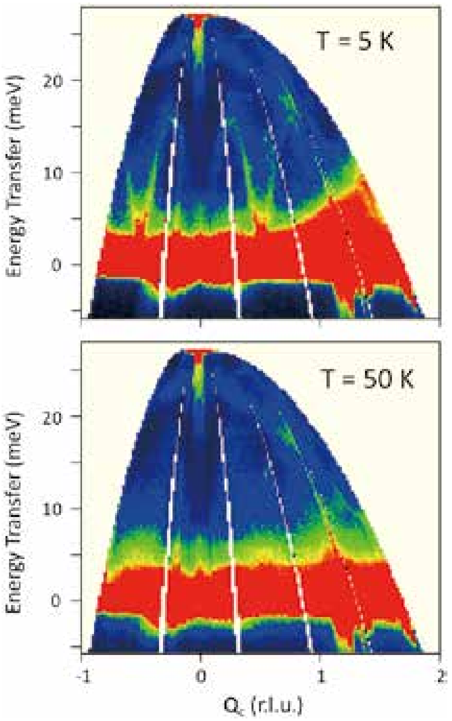

Fig. 1 Spin excitation spectra observed at 5 K and 50 K for CuGeO$_3$.

Figure 1 shows the spin excitation spectra observed in a wide energy and momentum spaces at 5 K (below T_{sp}) and 50 K (above T_{sp}) At 5 K, des Cloizeaux-Pearson-like modes emerge at $Q_c = \pm 0.5$, which corresponds to the magnetic zone center, and they vanish above T_{sp}. These observations are consistent with previously reported results [2], showing the potential of POLANO in observing the magnetic excitation of quantum spin systems. Furthermore, we found an anomalous temperature dependence in a high-energy optical phonon, which could be evidence of spin-phonon coupling. Since POLANO can carry out polarization analyses in high energy regions, details of the spin-phonon coupling in CuGeO$_3$ could be clarified in future polarized neutron scattering measurements taken with POLANO.

References

[1] S. Asano, K. M. Suzuki, K. Kudo, I. Watanabe, A. Koda, R. Kadono, T. Noji, Y. Koike, T. Taniguchi, S. Kitagawa, K. Ishida, and M. Fujita, Phys. Soc. Jpn. **88**, 084709 (2019).

[2] M. Arai, M. Fujita, M. Motokawa, J. Akimitsu, and S. M. Bennington, Phys. Rev. Lett. **77**, 3649 (1996).

Keywords: neutron scattering, quantum spin system, spin excitation

Masaki Fujita (Head of Center of Neutron Science for Advanced Materials)
E-mail: nc-imr@imr.tohoku.ac.jp
URL: http://nc-imr.imr.tohoku.ac.jp/index-e.html

Author Index

Keyword Index

Editors

Ryuta Kasada, Yoshinori Onose, Rie Umetsu,
Shigeyuki Takagi, Haruhiko Morito, and
Motomichi Koyama

Editorial Staff

Misa Y. Tomimatsu, Aki Oikawa, and Yuko Godart

Printing

HOKUTO Corporation

Organization

Institute for Materials Research
Tohoku University
2-1-1 Katahira, Aoba-ku, Sendai 980-8577, Japan
Tel. +81-(0)22-215-2144 Fax. +81-(0)22-215-2482

URL: http://www.imr.tohoku.ac.jp/
E-mail: pro-adm@imr.tohoku.ac.jp

Research

東北大学 金属材料研究所
Institute for Materials Research
Tohoku University

2-1-1 Katahira, Aoba-ku
Sendai 980-8577, Japan

http://www.imr.tohoku.ac.jp/